The Nanoscale Structure and Dynamic Properties of Ferroelectric Films

by

Christopher Tobias Nelson

A dissertation submitted in partial fulfillment
of the requirements for the degree of
Doctor of Philosophy
(Materials Science and Engineering)
in The University of Michigan
2011

Doctoral Committee:

Professor Xiaoqing Pan, Chair
Professor John W. Halloran
Associate Professor Jamie D. Phillips
Associate Research Scientist Kai Sun

Dedication

To my parents Mark and Lila
brothers Andrew and Daniel
& sister Katrina

Acknowledgements

I would foremost like to thank my advisor Dr. Xiaoqing Pan for his guidance and support during my graduate studies. He has generously and patiently provided me with the resources and opportunity to grow as a scientist. I would also like to acknowledge my undergraduate advisor Dr. James Fitz-Gerald who introduced me into academic research and helped to prepare me for the challenges of graduate school. This project was done in collaboration with several other groups whose contributions were essential to the success of this project. Dr. Darrell Schlom of Cornell University and Dr. Chang-Beom Eom of the University of Wisconsin provided the ferroelectric thin films studied in this work. Dr. Long-Qing Chen of Pennsylvania State University provided phase-field simulations of the ferroelectric domains structures. I owe all three of them a great debt of gratitude.

This work would have been impossible without the help of numerous friends and colleagues. I am grateful to Dr. Yanbin Chen and EMAL staff Dr. Haiping Sun and Dr. Kai Sun who trained me in TEM. I would also like to thank my fellow graduate students and post-docs in the Pan lab, in particular Peng Gao who has contributed significantly to this research by performing experiments and aiding the analysis and write-up of the in-situ switching, especially for PZT. From the Pan group I would also like to acknowledge Jake Jokisaari for his PFM measurements, Yi Zhang & Sung Joo Kim for additional help with sample preparation, Baihai Li for first-principles simulations of the $BiFeO_3$ interface (not included in this thesis), and Kui Zhang for Hall measurements. Lastly, I would also like to thank the present and former staff members of the National Center for Electron Microscopy (NCEM) at the Lawrence Berkeley National Lab for the training and use of the TEAM 0.5, currently one of the best microscopes in the world.

This work was made possible by funding from the Department of Energy under the grant DE-FG02-07ER46416 and partially by the National Science Foundation under grants

DMR-0907191, DMR-0820404 and DMR-0723032 (TEM instrument). Use of the NCEM facilities was available from support under the DOE grant DE-AC02-05CH11231 for user facilities.

Table of Contents

List of Figures

Chapter **1**

1 Introduction and Background

1.1 Introduction

Strongly correlated systems such as the transition-metal oxides exhibit many unique phenomenon including metal-insulator transitions[1], superconductivity[2], and magnetic and ferroelectric order[3]. The variety of technologically useful properties within a single materials system allows them to be easily integrated and holds the promise of all-oxide devices[4]. The close coupling of the correlation effects to lattice degrees of freedom can give rise to novel properties by imposing strain in a transition-metal oxide film through constraint to the lattice structure of a substrate. For example such strain can induce paraelectric materials to become ferroelectric[5], increase ferroelectric polarization[6], and increase the transition temperatures of magnetic[7,8] and superconducting[9,10] films. The interfaces between the correlated systems can themselves adopt novel properties such as the formation of conducting planes between insulators[11-13], or ferromagnetic planes between antiferromagnetic layers[14]. This broad design space and range of device applications has lead to the prominent study and use of transition metal oxides.

Of the aforementioned properties demonstrated by the transition metal oxides, ferroelectricity is of particular interest due to its hysteretic behavior under applied electric fields. Ferroelectricity is defined by the existence of multiple equivalent polar orientations that can be traversed by an applied electric field – a behavior similar to the reorientation of ferromagnetic moments under an applied magnetic field. However, electric fields are considerably easier to manipulate and the critical ferroelectric domain size is smaller than for ferromagnets making ferroelectric materials attractive for high-density non-volatile memories[15-20]. These materials are also high-k dielectrics and exhibit strong electromechanical coupling making them useful for gate oxides, sensors and actuators[19]. However, their most versatile attribute is that the switchable polarization

couples with electronic transport properties[20-23], surface chemistry[24], strain[25,26], and magnetic order[27,28], allowing for a variety of materials properties to be hysteretically controlled by an electric field. Even when the coupling of two specific order parameters is not intrinsic to a single material, the inclusion of ferroelectric films into heterostructures can allow them to be coupled indirectly. For example ferroelectricity and ferromagnetism can couple across an interface through electron exchange interactions[28-31] or by strain[27,32,33]. Through such planar process engineering, ferroelectric materials provide a unique ability to create electrically tunable and switchable functional devices.

Despite their utility, the adoption of ferroelectric films into certain device applications has been hampered by a few notable drawbacks. Ironically these tend to relate to the same order-coupling and sensitivity to environment that make them attractive in the first place. Specifically, over the long term ferroelectric films can suffer from a gradual loss of polarizability (fatigue), a gradual loss of the stored state (retention loss), and/or a gradual freezing in of the stored state (aging). These are discussed in more detail in section 1.2.1 but they are all commonly attributed to nanoscale defects and are just a few detrimental examples of the strong dominance of the nanoscale defect structure on ferroelectric switching. A specific understanding of the role of defects is necessary in order to engineer ferroelectric devices, including mitigating the aforementioned effects and to scale devices down to the size of the defect spacing where a statistical treatment is not applicable. Here, I report the nanoscale characterization of ferroelectric films which I combine with novel in situ ferroelectric switching using real-time and aberration-corrected transmission electron microscopy (TEM). In the chapters which follow I reveal the controlling role of defects such as dislocations and interfaces in the static structures and switching dynamics of two prominent ferroelectric materials: $BiFeO_3$ and $PbZr_xTi_{1-x}O_3$.

1.2 Ferroelectric and Multiferroic Materials

1.2.1 Ferroelectrics and Multiferroics

The first ferroelectric material, Rochelle Salt, was reported nearly 90 years ago by J. Valasek[34]. Since then many hundreds have been discovered, nearly all of them oxides although there has been some recent attention paid to the fluorides as well[35,36]. Of these, the most commercially and scientifically prevalent belong to the perovskite ABO_3 family (A and B are cations). These are prototypical displacive-type ferroelectrics which upon cooling through a Curie temperature adopt a lower-symmetry non-centrosymmetric structure which possesses a dipole moment. The dipole moment has multiple degenerate orientations as illustrated schematically by the double-well energy diagram of a tetragonal perovskite in Fig. 1.1.

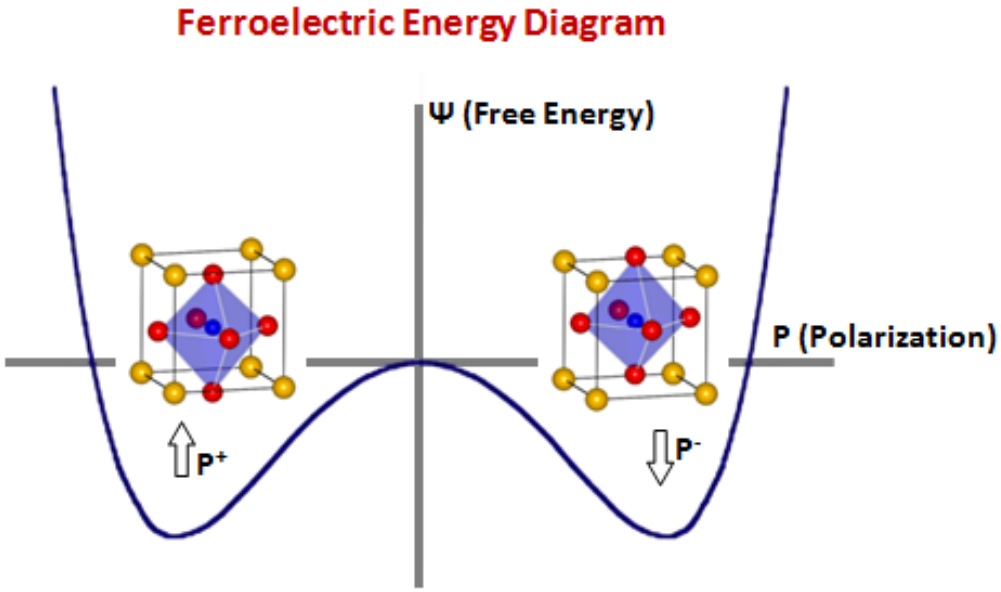

Fig. 1.1 Free Energy vs. Polarization in Ferroelectrics
Double energy-well potential of the ferroelectric polarization. Here, the ferroelectric can adopt one of two degenerate polarizations along the [001] axis to minimize it's free energy. Specifically shown are the c+ and c- polarizations of tetragonal $PbZr_{0.2}Ti_{0.8}O_3$ unit cell, although the actual shape of the double well energy curve is purely illustrative. The oxygen octahedral are displaced downward and upward, respectively, compared to the Pb cage resulting in the dipole moments (polarizations) shown.

In ferroelectrics, long-range coulombic forces promote the polar ferroelectric distortion, whereas short range repulsions favor an undistorted cubic structure. For the ABO_3 case, covalent bonding between the B-site cation and oxygen soften the repulsive force and stabilize the ferroelectric state. Thus, they must possess a B cation whose lowest unoccupied state is a d-orbital which hybridizes to oxygen 2p[37]. However, the A-site can also play a significant role such as in the two ferroelectrics which are the focus of this

work: $BiFeO_3$ and $PbZr_xTi_{1-x}O_3$. In both, a lone electron pair on the Bi and Pb atoms leads to a large A-site distortion and hybridization with the O 2p orbital[37-39]. Due to this lone-pair, the atomic displacements are especially large in these materials which will be important for the TEM polarization mapping developed in section 3.3.

Recently, there has been significant scientific effort put towards multiferroic materials[40], i.e. those which posses multiple types of ferroic order ((anti)ferroelectric, (anti)ferromagnetic, ferroelastic, or ferrotoroidal). Typically multiferroic is interpreted to refer only to materials which exhibit (anti)ferroelectric and (anti)ferromagnetic order or even more strictly to only the ferroelectric and ferromagnetic properties. The reason is that ferroelectricity and ferromagnetism are technologically useful properties such as for storing information in memory. A material which posses both uncoupled can be used as a four state memory bit ($P\uparrow M\uparrow$, $P\uparrow M\downarrow$,$P\downarrow M\uparrow$, $P\downarrow M\downarrow$)[41]. More commonly, and perhaps more convenient, is when the two are coupled[29,30]. This combines the advantages of both types of memory: the ease of writing the ferroelectric state with an electric field and ease of reading the ferromagnetic state through magnetoresistance. In addition to memory such multiferroics could be used for a broad range of potential magnetoelectric applications[42].

Unfortunately, there are currently no single phase materials with significant ferroelectric and ferromagnetic properties at room-temperature. Even if one includes antiferromagnetic ordering there are only a few rare cases of which $BiFeO_3$ is the forerunner. The rarity of finding these two properties simultaneously was addressed by first-principles calculations which found there is a mutually exclusive requirement for the B-site d-orbital occupancy[3]. Ferroelectricity requires the formal valence of the B-site to be d_0 (empty d orbital), however without any unpaired electrons no magnetic ordering, ferro or otherwise, is possible. $BiFeO_3$ represents an unusual case where ferroelectricity is primarily driven by the lone-pair on the A-site Bi atoms allowing the relaxation of the d_0 requirement of the B-site, i.e. Iron. Although the perovskites have excellent ferroelectric properties, this lack of magnetic order has been a large part of the driving force towards finding new classes of ferroelectrics such as the fluoride based multiferroics[36].

An alternate route to achieving magnetoelectric materials despite the lack of single phase materials is to combine multiple layers into magnetoelectric heterostructures[32]. For example a magnetoelectric bilayer can be created from a piezoelectric layer (changes strain with applied field) coupled to a magnetostrictive layer (changes magnetic order with applied strain) [33,42]. More commonly of late is the coupling of a multiferroic (ferroelectric/antiferromagnetic) to a ferromagnetic layer through the electron exchange interaction of the antiferromagnetic and ferromagnetic orders[28,30,31]. This latter type of magnetoelectric heterostructure, specifically multiferroic $BiFeO_3$ on ferromagnetic $La_{0.7}Sr_{0.3}MnO_3$, will be the focus of section 5.3.

Unless the polarization degeneracy is lifted by a significant external field or other defect, a bulk ferroelectric sample or ferroelectric film will typically form a polydomain structure composed of multiple different polarizations. Usually, such structures are energetically favorable as a means of reducing the electric field and strain energy. The surface energy of the domain walls which separate disparate polarized regions are typically less than a few hundred mJ/m^2 [43,44]. This is sufficiently small that ferroelectric films often adopt high densities of domain walls. However, this domain wall energy becomes prohibitive for sufficiently small domains since it scales with the surface area of the domain rather than its volume. Ferroelectric domains below a critical size threshold are intrinsically unstable. This imposes a significant barrier for ferroelectric switching which must form stable nuclei of new domains.

Early theoretical calculations by Rolf Landauer of the energy and critical domain size required to initiate switching were impossibly large, on the order of the entire thickness of a several micron film[45]. This was clearly at odds with observations of nucleation dominated switching behavior and the critical voltage required[46] and became known as the “Landauer’s paradox”. The solution to this discrepancy is the introduction of defects to the ferroelectric crystal which provide local regions with reduced nucleation barriers. The switching between ferroelectric orientations is entirely governed by such defects, most notably the interface (detailed in section 3.1). For practical reasons, ferroelectric switching usually occurs in a planar capacitor type geometry with a uniform electric field. Switching in this geometry is illustrated schematically in Fig. 1.2 and begins with the

nucleation of domains at the interfaces when the field exceeds the critical field (E_C). Switching then procedes by two stages of domain growth: fast growth parallel to the field, and slow lateral growth. The disparity in velocity is due to the high energy of the forward edge of the domain which makes it unstable. According to simulations it is a similar mechanism which drives the lateral growth whereby small kinks in the domain wall are rapidly pushed across to the interface[47]. However, the total domain motion of this stage is much slower since it is limited by the nucleation rate of such kinks.

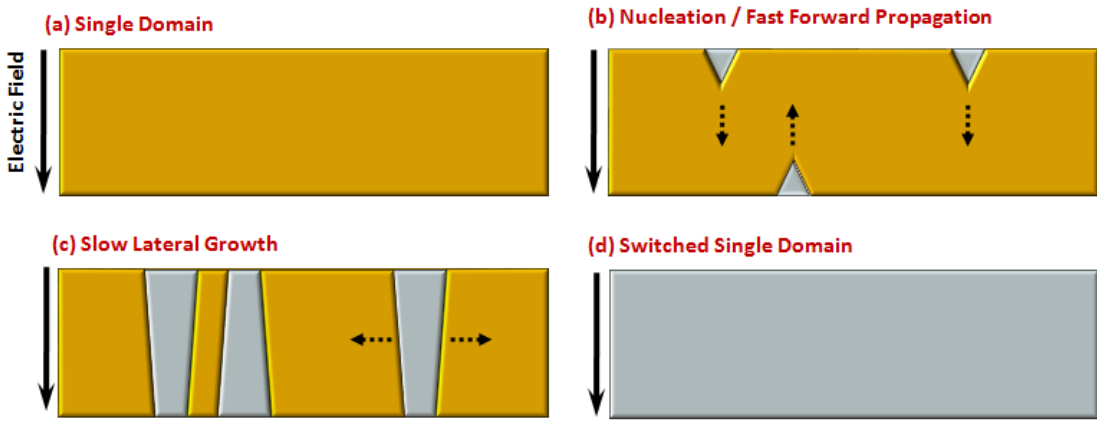

Fig. 1.2 Model Ferroelectric Switching
The chronological domain structure of a ferroelectric switching in a planar capacitor. **(a)** initial single domain structure is unchanged while E<critical field. **(b)** Nuclei form at the surfaces/interfaces and rapidly propagate parallel to the field as "needle domains". **(c)** After reaching the opposite surface, domain walls expand slowly laterally. **(d)** Fully switched film.

Ferroelectric switching is classically understood to be kinetically limited either by the nucleation rate or growth rate of new domains. The most popular model to fit this ferroelectric behavior is a domain wall limited Kolmogorov-Avrami-Ishibashi (KAI) model[48-50]

$$P(t) = 2 \cdot P_S \cdot \left(1 - e^{-(t/t_0)^n}\right) \qquad 1\text{-}1$$

where P(t) is the change in polarization with time, P_S is the spontaneous polarization, t_0 is the characteristic switching time which is inversely proportional to the domain wall velocity, and n is a constant ≥ 1 which depends on geometry and the assumptions of the nucleation rate: either constant rate or zero rate after t=0 (latent nuclei). This model provides a good empirical fit to many experimental reaction rates[47,51-53] but it should be

noted that it makes several inaccurate assumptions such as a constant domain wall velocity independent of the domain radius and that domain growth is unrestricted. Several studies have addressed regimes where the KAI model fails[54] such as at low fields or polycrystalline samples[55] or when considered over large timescales[56] and proposed models which incorporate a distribution of nucleation and relaxation times. However, all of these models are empirical fits aggregating the switching behavior over large volumes. These models are not well suited to describe the nanoscale where switching may be dominated by only a few nucleation sites and where the domain wall velocity is not a constant – which has been demonstrated by switching of a nanoscale capacitor[57]. The authors of ref 57 were never-the-less able to fit their switching behavior to the known field dependence of the nucleation rate and domain wall velocity:

$$Nr \propto e^{\left(-\frac{\alpha_N}{E}\right)} \quad \text{1-2}$$

$$DW_{vel} \propto e^{\left(-\frac{\alpha_V}{E}\right)} \quad \text{1-3}$$

where α_N and α_V are temperature dependent activation fields for nucleation and domain motion respectively. Despite a functional form similar to Arrhenious equations, the activations do not necessarily incorporate a kT^{-1} term. Recent variable temperature surface probe switching experiments suggests that the nucleation may not be, or at least isn't required to be, a thermally activated process[58] as originally envisioned by Landauer. A common feature of all of these models is that the sample/field is homogeneous and switching is kinetically limited. The nanoscale switching of real thin-film system shows that this assumption is inaccurate and results in some marked deviations from the model behavior (section 5.3).

Unfortunately there are several common deleterious phenomena in real ferroelectric films. Most notable is fatigue, whereby this switching process degrades after many cycles manifesting as a reduction in the polarization change. Scott and Pouligny showed that only a very small fraction of total film actually changes phase[59], indicating that the switching domain walls were being pinned by these relatively few altered regions. Given the known influence of oxygen on ferroelectric fatigue[54,60,61] one of the primary

contributions is almost certainly some form of oxygen vacancy gradient or complex with other point defects. In addition, domain walls can become pinned by one another as reported in 180° switching of $BiFeO_3$[62]. Defect pinning, oxygen vacancy pinning, and domain wall/domain wall pinning are all observed by nanoscale switching in section 5.3.3 as is dislocation pinning in section 5.4.2.

Ferroelectric films can also exhibit two opposing long-term tendencies: either failing to retain its stored polarization (retention failure)[63-71] or, ironically, forming a significant barrier to switching away from the stored polarization (imprint/aging). In both cases this process is tied to the thermodynamic stability of the domain state, specifically that the polar orientations are no longer degenerate as in the model case depicted in Fig. 1.1. In the case of retention failure, the saved state is higher energy than another polarization leading to a gradual transition to the lower energy state. This degeneracy can be the result of built-in electric fields[72-78] or strain[79,80], the latter sometimes produced by the switching itself. Aging, on the other hand, results from charged defects slowly aligning and migrating according to the polarization direction and domain structure. This creates a built-in field which makes the current polarization lowest in energy and has to be overcome in order to switch. Imprint is the same as aging except it is in response to an external field which will similarly influence polar defect alignments and, if an electrode is in contact, can inject charge carriers. From the nanoscale switching experiments in this work, an additional contribution to the retention failure of small domains is added: the domain wall itself can be metastable (section 5.4.3).

1.2.2 $PbZr_xTi_{1-x}O_3$

Lead Zirconate Titanate ($PbZr_xTi_{1-x}O_3$), also known as PZT, is either tetragonal or rhombohedral depending on the Ti^{4+}/Zr^{4+} ratio. The commercial prominence of this material largely stems from an abnormally large piezoelectric and dielectric coefficient at the boundary between these two phases (called the morphotropic phase boundary) near x=0.52 at room temperature[81]. Its prominent use as a ferroelectric stems from its large polarization vector (~70 μCm^{-2} at our composition)[82,83]. In this work we use a x=.2 composition, $PbZr_{0.2}Ti_{0.8}O_3$, which is a tetragonal phase with a corresponding Curie temperature (T_c) for its transition to the high temperature paraelectric phase at ~450°C[81].

There are six nominally degenerate <100> polarization directions in tetragonal PZT. A transition between any two vectors requires a rotation of either 90° or 180° which therefore corresponds to the two types of domain walls and switching which can occur. The crystal structure of the [001] polarization is shown in Fig. 1.3. An electric dipole moment is created by relative displacements between cations (Pb,Zr/Ti) and anions (O) from their centrosymmetric positions. Due to the lone electron pair on the Pb atoms, the largest displacement is of the Pb atoms relative to the oxygen octahedra, and is clearly visible in the crystal structure (oxygen octahedral is shifted downward from the cube center). Due to the smaller a-lattice parameter orthogonal to the polarization, PZT films grown under compression will preferentially adopt a c-axis orientation as in this figure (i.e. the a-sides are in the film plane). Thus, the six degenerate polarizations are reduced to just two: up $P_{[001]}$ or down $P_{[00\bar{1}]}$ (Fig. 1.1).

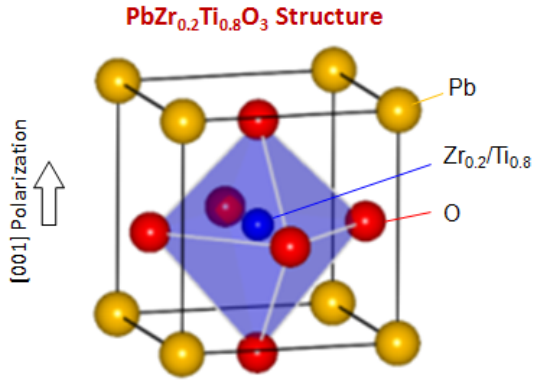

Fig. 1.3 $PbZr_{0.2}Ti_{0.8}O_3$ Structure
The perovskite unit cell of $P_{[001]}$ $PbZr_{0.2}Ti_{0.8}O_3$ shows the downward displacement of the oxygen octahedral and to a lesser extent the central B-site Zr/Ti cation. This results in an electric dipole moment upward.

1.2.3 $BiFeO_3$

$BiFeO_3$ is popular for a number of reasons, most importantly because it is an extremely rare case of a single phase room temperature multiferroic (T_C = 1103°K & T_N = 643°K)[84]. It also has a very large spontaneous polarization (~100 μC/cm^2)[85] making it attractive for its ferroelectric properties alone. Though it has a bulk rhombohedral R3c structure, the application of large compressive substrate strain creates a morphotropic phase boundary with a tetragonal phase making it a potential replacement for $PbZr_xTi_{1-}$

$_xO_3$ even as a piezoelectric[86]. Although the unit cell is rhombohedral, cubic indices corresponding to the perovskite cell will be used throughout this work. The structure of $BiFeO_3$ can be envisioned by two pseudocubic perovskite unit cells connected along the body diagonal (Fig. 1.4). The oxygen octahedra and the central Fe cation are displaced along one of the eight <111> directions ([111] in Fig. 1.4a) from their respective positions at the face and body centers giving it a dipole moment. Rotations between polarizations can be 71°, 109°, or 180° yielding these three types of domain walls. The oxygen octahedra are additionally counter rotated by ±13.8° around the <111> axes[26], thus the necessity for two perovskite cells to illustrate the structure. Like Pb in PZT, the lone pair on the A-site Bi is responsible for the large displacement and polarization. The pseudocubic unit cell is slightly elongated along the polarization axis. Therefore polarization rotations between the four different axes of polarization are accompanied by strain as the direction of the rhombohedral distortion changes, known as ferroelastic switching. Hereafter, I shall use the Streiffer shorthand notation to distinguish the four ferroelastic variants r_1-r_4, where [001] is the film normal and r_1 corresponds to $\pm P_{[111]}$, r_2 to $\pm P_{[\bar{1}11]}$, r_3 to $\pm P_{[\bar{1}\bar{1}1]}$ and r_4 to $\pm P_{[1\bar{1}1]}$.

The magnetic moment of the Fe cation is normal to the polarization and alternates between the corner adjacent perovskite cells (Fig. 1.4b). In bulk $BiFeO_3$ this moment can occur along any of six degenerate easy directions on the perpendicular easy plane (corners of the yellow polygon). However, substrate induced strains can break this degeneracy and create a single preferred axis[87]. Regardless, a change of the antiferromagnetic ordering requires a change of the polarization axis which only occurs for 71° and 109° switching. As mentioned previously, the change of polarization axis also changes the rhombohedral distortion of the perovskite cell, thus it is also a ferroelastic transition and accompanied by strain.

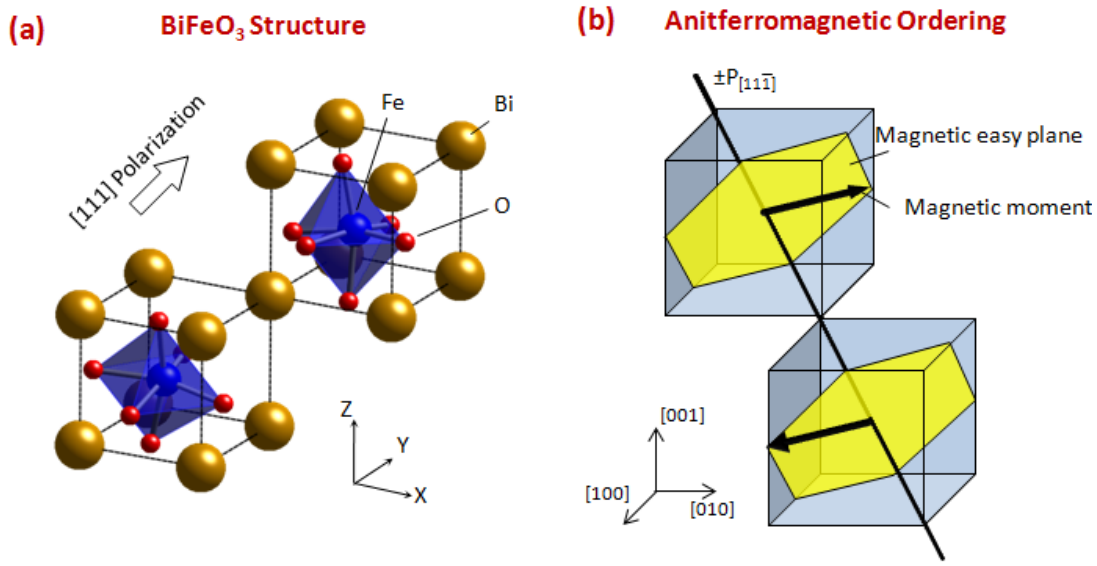

Fig. 1.4 $BiFeO_3$ Stucture
(a) Structure of $BiFeO_3$ shown by two corner adjacent perovskite cells. The oxygen octahedral and central Fe cation are displaced along the [111] axis, and the two octahedral are oppositely rotated by ±13.8°. **(b)** The magnetic moment of the Fe cation alternates between adjacent unit cells along the polarization axis. In bulk $BiFeO_3$ is can adopt one 6 easy axis on the magnetic easy plane show by the yellow polygon.

Chapter 2

2 Experimental Techniques

2.1 Transmission Electron Microscopy

In order to view ferroelectric switching in low dimensional systems such as the normal axis of a thin film, very high spatial and temporal resolution characterization is required. This is possible using transmission electron microscopy (TEM) whereby the domain structure is imaged by a high energy electron beam which passes through the sample. Generally spatial resolution is limited by the wavelength of the probe being used, and for electrons this wavelength is extremely small (0.00197 nm at 300kV). Very recently the resolution limit of TEMs have been pushed into the sub-Angstrom regime due to the development of correctors for spherical aberrations (Cs) in the electron optics[88]. At this measurement scale, TEM provides not only a means to characterize ferroelectric switching but can view the full ionic structure of perovskite materials and ultimately determine polarization distributions at the unit cell level (section 3.3).

This chapter will provide the experimental background for the data and analysis presented in this work. It will primarily consist of TEM operating principles and analysis, a very extensive topic and the interested reader is pointed to the texts of Williams & Carter[89] and Fultz & Howe[90] for a more thorough introduction. This chapter will also provide an experimental description of the film growth and TEM sample preparation methods and detail the phase-field simulation method used to model and analyze domain structures.

There are two main operating modes for TEM imaging distinguished by either illuminating the sample by a convergent electron beam (Fig. 2.1a) or a parallel electron beam (Fig. 2.1b) using the system of condenser electron lenses (CL1 and CL2 in the figure). In parallel beam illumination, the sample is magnified by the lens system as shown by the color coded beams which reproduce the specimen shape at the viewing

plane. This mode transfers a great deal of information about the crystal through its interaction with the planar electron wave. For example, small angle diffraction from the crystal planes near the Bragg condition, as illustrated in red and blue ray traces emitted from the sample in Fig. 2.1c, create a diffraction pattern at the back focal plane which can give detailed information about the crystal structure especially when the sample is aligned along a crystallographic zone axis. In contrast the convergent beam mode is rastered across the sample surface, termed scanning transmission electron microscopy (STEM), and relies little on wave-nature interactions with the sample since the scattering is incoherent. Instead, a variety of signals generated from the local scattering of electrons is gathered from specialized detectors and provides information about the local chemical structure.

The variety of signals produced by the incident electrons are due to the different types of scattering which occur in the sample. Electrons which pass near the nucleus or electron cloud can be elastically (i.e. without loss of energy) deflected by coulombic interactions. Scattering from the nucleus can result in very high angle deflections which includes backscattered electrons. Alternatively an electron can lose energy to the sample, known as inelastic scattering. When the energy is transferred to an atom it generally leads to the expulsion of an electron, known as a secondary electron. If the missing electron came from a tightly bound inner shell of the atom, a significant and characteristic amount of energy is released when another electron takes its place. This energy can be released as an X-ray, or by ejecting another outer shell electron (Auger electron).

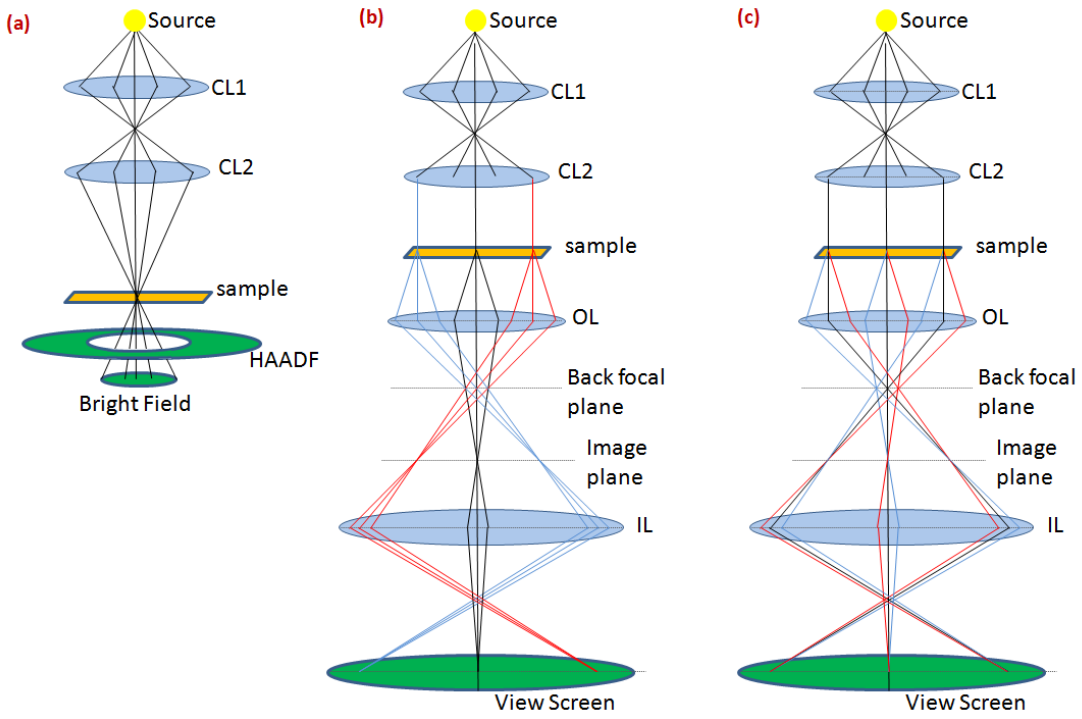

Fig. 2.1 TEM Optics
(a) Ray diagram of the electron path for convergent beam scanning techniques. The condenser lens system, here shown by CL1 and CL2, focuses the beam on the sample surface. This technique generally does not use post-sample electron lenses and incorporates various detectors specialized to measure specific electron interaction signals, here a high angle annular dark field (HAADF) and bright field detector. **(b,c)** Ray diagram of parallel illumination TEM which incorporates post sample objective (OL) and intermediate (IL) lenses to image the sample. In (b) colored ray traces follow the beam generated by different regions of the sample which reproduce the original structure at the view screen plane. In (c) colored ray traces follow specific diffraction angle from each region. This highlights the diffraction pattern formed on the back focal plane.

2.1.1 Diffraction Contrast TEM

The diffraction of the incident planar electron wavefront provides a great deal of information about the crystal orientation and symmetry. In normal TEM operation, signals from the diffracted and transmitted beams both contribute to the image (Fig. 2.1c). However, in dark field imaging an objective aperture is inserted into the back focal plane so the information is restricted to specific diffracted beams (Fig. 2.2). Wherever atomic planes in the sample are oriented to satisfy Bragg diffraction and this beam passes through the objective aperture in the back focal plane it will appear bright in the dark-field image. Alternatively, in bright field imaging the objective aperture selects only the transmitted beam and all strongly diffracted regions will appear relatively dark. In practice dark field imaging is not done as illustrated in the ray diagrams in Fig. 2.2.

Instead the incident beam is tilted when it enters the sample so that the selected diffracted beam travels along the optical axis of the TEM. This helps to avoid lens aberrations (which are less of a consequence with new Cs correcting optics).

Diffraction contrast imaging is very useful for imaging ferroelectric materials. Ferroelastic switching changes the crystal orientation and thus the diffraction pattern which results in sharp image contrast. More importantly, dynamic scattering effects lead to the breaking of Friedel's law[89,91] which states that diffraction from any plane (hkl) must equal its opposite ($\overline{hkl}$). Normally Friedel's law precludes the detection of noncentrosymmetric crystals, as is the case in x-ray diffraction. However, noncentrosymmetry manifests in electron diffraction and allows the detection of 180° switching. Thus, this method allows for all polarization changes to be directly imaged. A second benefit of this method compared to STEM is that the image is formed in parallel so the acquisition speed is limited only by the detector.

Diffraction contrast images in this work were aligned close to the zone axis but tilted away by ~1° so that only a single set of planes was close to the Bragg condition. In practice this is done by tilting along Kikuchi lines while operating in diffraction mode (the back focal plane is projected on the viewing screen). In this case a single line of diffraction spots normal to the plane are present and these can be selected by the objective aperture. Normally I have selected the 2nd diffraction spot away from the center transmitted spot to avoid the latter's accidental inclusion at the edge of the aperture. A selected area aperture (an aperture in the image plane restricting the sample area being imaged) is used during the alignment but removed during imaging.

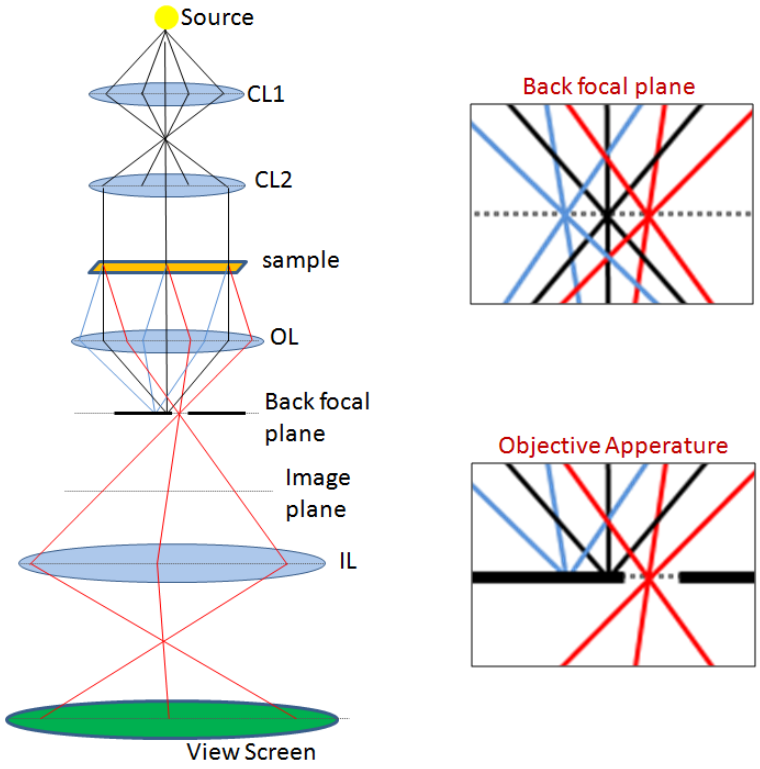

Fig. 2.2 Diffraction Contrast Imaging
Ray diagram of diffraction contrast TEM whereby an aperture is inserted into the back focal plane (magnified in inset images). Traces are colored based on diffraction angle, the aperture in this case selects only the red trace corresponding the diffraction angle to the right of the transmitted beam.

2.1.2 Phase Contrast High Resolution TEM (HRTEM)

By restricting the image-forming region at the back focal plane, diffraction contrast imaging limits the transmitted information thereby sacrificing resolution. High resolution information can instead be attained by cumulative effect of the periodic atomic potentials on the propagating planar electron wave – termed phase contrast imaging. The electron wave is diffracted at the atomic potentials forming an interference pattern with the undiffracted wave. This is manifest as spatial variation in the amplitude and phase of the propagating electron wave (see Fig. 2.3). The resultant wave pattern is further altered as it passes through several post-sample lenses prior to the image plane. Although this method provides optimal information transfer, the image is an interference pattern and not directly interpretable. In general the image will reproduce the periodicity of the structure but the atom positions do not necessarily correlate with regions of high or low intensity. Furthermore, aberrations in the objective and intermediate lenses will alter the

image and limit the resolution. This mode is also very sensitive to changes in sample thickness, high-order aberrations in any of the lenses, and sample orientation. For a combination of these reasons, no phase contrast images are used directly in this work. However, a derivative of this method, exit wave reconstructions (section 2.2.4), which mitigates many of these problems are used instead.

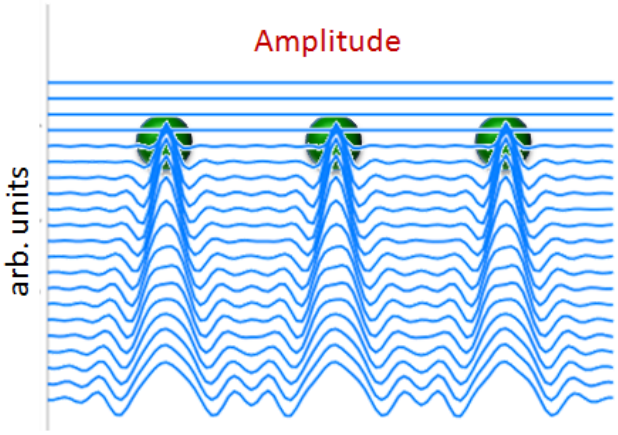

Fig. 2.3 Phase Contrast Imaging
Propagation of the amplitude of a planar electron wave through a periodic atomic potential represented by the three green atoms. The final wave at the bottom, barring distortion by post-sample lenses, would appear in the final image.

2.1.3 Scanning Transmission Electron Microscopy (STEM)

STEM imaging uses a rastered convergent beam and forms images based on deviations in electron scattering. In the two primary STEM modes these are elastic scattering events which are either detected directly (dark field) or by a change in the transmitted beam intensity (bright field). Alternately, images based on deviations in inelastic scattering provide details of the band structure of the sample under the probe, and these modes are generally referred to as analytical TEM and discussed in the next section. Analytical TEM can also be used for imaging but the lower frequency of these inelastic scattering events leads to very long acquisition times during which the sample may drift or become damaged by the beam. STEM has several advantages compared to HRTEM, most importantly the images are not interference patterns and therefore they can generally be interpreted directly. This is not strictly true for STEM imaging of low angle scattering which is partially coherent but even in this case the atomic positions are still usually

directly interpretable from the resultant image. An additional advantage is that the detected electrons do not pass through any post-sample optics which are a source of aberration. STEM is also more robust to variations in sample thickness than HRTEM which has a strong thickness dependence of the interference pattern and will undergo contrast reversal. STEM is also robust to small deviations in the alignment of the beam to the sample zone axis. Columns of atomic potentials act as waveguides to steer the beam to follow the sample zone axis.

The primary STEM imaging modes are differentiated based on the angle of the scattered electrons used to form the image. The most common mode uses an annular detector with an inner diameter set to collect electrons which have scattered more than ~75 milliradians[90] known as a high-angle annular dark field (HAADF) imaging. Scattering through such high angles is the result of Rutherford scattering from coulombic interactions between the incident electrons and the atomic nuclei in the sample. This scattering is strongly dependent on the nuclear charge (Z) of the atoms, so the resulting HAADF images are often referred to as Z-contrast images. The Z-dependence of Rutherford scattering is $\propto Z^2$ as given by the Rutherford differential cross section:

$$\frac{d\sigma_R}{d\Omega} = \frac{Z^2 e^4}{16E^2 \sin^4 \theta} \qquad 2\text{-}1$$

where E is the energy, e is the elementary charge, and θ is half the scattering angle. In practice the actual exponent of the power-law Z-dependence of HAADF images is slightly lower. These images are easily interpreted since the atomic nuclei are mapped directly with an intensity which corresponds to their atomic number.

Alternately, a “bright field” detector is designed to capture only the small angle scattered electrons, including those that are directly transmitted through the sample. Given the very strong angular dependence of equation 2-1, the magnitude of low angle scattering is much larger than at high angles. However, unlike HAADF the scattering is not restricted to Rutherford scattering nor is it completely incoherent and the image will include effects such as Bragg diffraction. It is this property which also make is useful for detecting low Z elements whose contribution to HAADF images can be negligible, the topic of section

2.2.4. Both HAADF and bright field imaging are used in this work. These two detectors are depicted schematically within the TEM optics system in Fig. 2.1a.

2.1.4 Analytical TEM

Detection of the inelastically scattered electrons and quantification of the energy transferred is used to provide information of the chemical structure of the region under the probe. This is primarily done either by measuring the energy loss of the transmitted electrons known as Electron Energy Loss Spectroscopy (EELS) or by detection of the x-rays generated from an electron falling into a vacancy in the inner shell known as Energy Dispersive X-ray Spectroscopy (EDX or EDS). In this work, a variation of the former approach is used for determining sample thickness (section 5.2.2) and the latter approach is used to characterize the composition across the $BiFeO_3$ interface (section 3.5).

EELS is an extremely powerful technique because it detects any loss of energy by the incident electrons, not just those due to ionization of an inner electron as in EDS. In practice, though, this is not as large of an advantage as it may sound because the scattering cross section for plasmons is very large. Thus a broad low energy Plasmon peak will dominate the low energy EELS structure and mask other low-energy signals such as from ionizing outer shell electrons. Additionally, tightly bound deep inner shell electrons have very small scattering cross sections so their signal is very weak. The practical result is that the useful orbital ionizations tend to overlap between EELS and EDS since the ionization events with the largest cross sections will yield the strongest signals. However, the additional information provided by EELS does have significant implications, including the plasmon scattering at low energies which increases with sample thickness and even the (potential) detection of band gaps[92,93], though this is controversial in practice due to uncertainty in deconvoluting the energy distribution of the electron source and accounting for Cherenkov radiation. EELS is also more sensitive to low Z elements making it preferential for analyzing elements such as oxygen which was previously mentioned for its major role in ferroelectric fatigue. Most importantly, the shape of an element's EELS structure at the edge of a core loss peak (the near-edge structure) provides information about its density of states and bonding environment,

including its valence, and can provide atomic level characterization of the electronic structure[12,94,95].

EELS data is collected by adding a spectrometer to the end of the STEM (or TEM) beam line. The electrons are separated by energy based on their radius of curvature in a magnetic field and imaged by a CCD. Thus the data is presented as a large bright peak corresponding to the non-scattered and elastically forward scattered electrons known as the zero loss peak (ZLP), and each elemental peak corresponding to higher energy loss as a small satellite peak at increasing distance from the ZLP. Alternatively, an aperture can be inserted into this spectrometer to filter a TEM image for a specified range of energy; a technique called energy filtered TEM (EFTEM). EFTEM imaging was used in this work to isolate the elastic and inelastic scattering of the sample to determine the sample thickness. The inelastic component is determined by subtracting the elastic scattering from an unfiltered image. The elastic component was determined by selectively filtering for only the ZLP energy range. The inelastic scattering is dominated by plasmon scattering which scales with the thickness of the film, thus the inelastic scattering is representative of specimen thickness. The EFTEM generated thickness map is discussed in section 5.2.2.

EDS is a very useful technique for measuring chemical composition of a sample. It is generally less efficient than EELS because it measures only a fraction of the inelastic scattering. Specifically it requires that a core electron be ejected, that the energy released in replacing it is in the form of an x-ray, and that the x-ray is emitted within the collection angle of the detector. The energy released by filling the electron hole can instead be emitted as an Auger electron, a process which is dependent on atomic number. For light elements, the x-ray yield is essentially zero while the Auger yield is 100%. The two don't reach parity until ~Z=33 for Arsenic after which X-ray emission is the dominant mechanism. The upshot is that EDS is most efficient for heavy elements, and completely ineffectual for very light ones. However, aside from the low Z elements EDS is very broadly reliable across a range of elements. This is not necessarily true for EELS since elemental core loss tends to have very large tails and the peak appearance will vary with

the near edge structure which for many elements may appear so broad as to be difficult to get a baseline.

2.2 Microscopy of Ferroelectric Films

This section will specifically focus on the microscopy of ferroelectric oxides. It is designed so that the reader should be able to reproduce the experiments and techniques employed in this work.

2.2.1 Sample Preparation

TEM requires an electron-transparent specimen, ideally thin enough that an incident electron will only scatter once. Multiple scattering events can lead to artifacts in the diffraction and inelastic scattering information. Generally this means reducing a specimen dimension to less than half of the mean free path between plasmon scattering events (λ) where λ is dependent on the electron energy and is ~100 nm for metals and semiconductors at 100 keV[90]. From our experiments of $BiFeO_3$ at 200 keV λ=70 nm (see section 5.2.2), which means the specimen should ideally be less than 35 nm thick along the electron beam direction. This is accomplished by mechanical polishing from a larger single-crystal specimen. This procedure is depicted for a cross sectional TEM sample of an epitaxial film in Fig. 2.4. A sacrificial silicon layer is glued to the surface of the film using MBond 610 and placed on a hot plate at 130°C for at least 4 hours (typically 12-24). The sandwich is then sectioned into ~ 1.5mm slices by a lubricated diamond cutting saw. The cross section surface is then mounted with crystal wax to a tripod polisher and polished using a series of progressively finer grit diamond polishing paper under water flow, usually ending with either 0.5 or 3 µm. For in-situ experiments a small ~10° angle is sometimes applied so that the film can be viewed on the zone axis when the specimen surface is tilted (by ~10°). The sample is then flipped, remounted, and polished until the sacrificial silicon layer is thin enough to appear bright red to orange under transmitted light. Often a small thickness gradient is deliberately applied so that the specimen is thinnest on the silicon side and thickest at the substrate in order to avoid substrate cracking. A molybdenum ring is then glued to the 2nd polished surface and allowed to dry for 24 hours at ambient temperature. The specimen is then soaked in acetone until the sample falls free. The mounted specimen is Argon ion milled in a Gatan precision

ion polishing system (PIPS) with a low energy gun attachment. The sample is ion milled from both the top and bottom surfaces with the ion beam oriented normal to the interface. The angle and energy of the ion guns is progressively reduced from an initial setting of ±4° and 4 keV ultimately to a ±3° and 200 eV surface cleaning step. The silicon is milled preferentially and the process is stopped when the silicon just barely covers the film. The finished sample usually appears as in Fig. 2.4g.

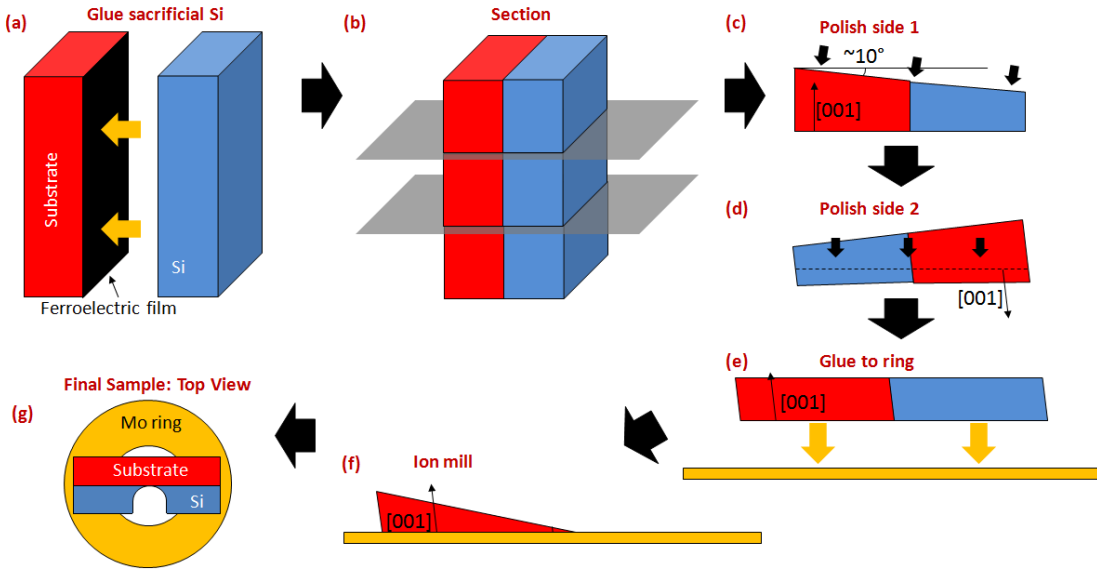

Fig. 2.4 TEM Sample Preparation
(a) Sacrificial Si is glued to the film. **(b)** Film is sectioned. **(c)** First side is mechanically polished, sometimes at an angle for in-situ experiments. **(d)** The second side is polished and **(e)** glued to a Mo ring. **(f)** The specimen is detached and ion milled. **(g)** The final specimen

This specimen preparation procedure is modified slightly for planar view samples. In such cases no sacrificial Si layer is glued to the film. However, the sample is polished next to silicon to provide a thickness indicator. Both mechanical polishing and ion milling are only done from the substrate side. During the ion milling step the film is mounted film-side down with wax on a post to avoid sputter deposition.

In-situ switching experiments require that the ferroelectric film surface is accessible to a side-access movable conducting needle. This is achieved by tilting the sample to provide clearance for the probe as shown in Fig. 2.5a. The angled polishing described and illustrated previously allows for zone axis imaging in this case. The silicon layer is mechanically broken free to provide access to the film. The buffer electrode is grounded

to the ring on both sides of the sample as shown in Fig. 2.5b. The contacts are made by silver paste or carbon paint.

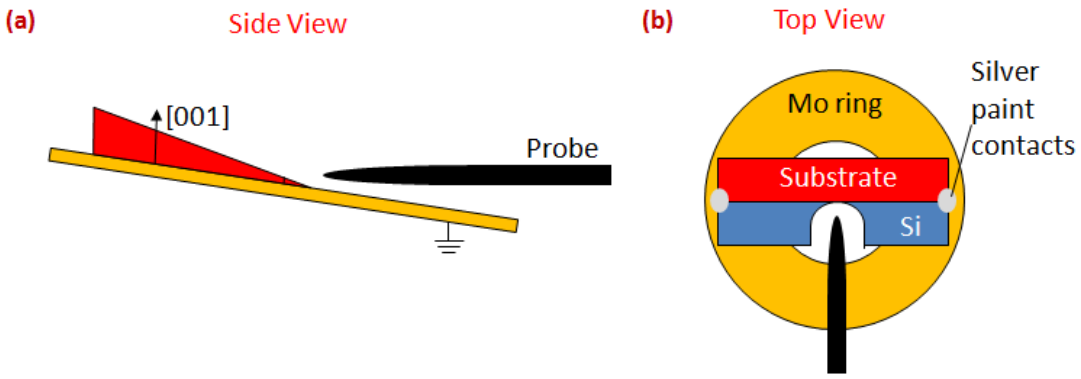

Fig. 2.5 TEM In-situ SPM for Ferroelectric Switching
(a) Side-view of in-situ switching experimental geometry. The sample is tilted to provide clearance for the probe.
(b) Top view shows the silver paint contacts used to ground the buffer electrode.

The tungsten probes used for the in-situ measurements were formed by electrochemical etching in a NaOH solution similar to ref 96. A short length of tungsten wire was dipped approximately 2 mm into the NaOH solution. A current was passed through the tip, electrolyte, and a small wire ring serving as a counter electrode. At the point when the necking tungsten wire suddenly breaks and drops into the beaker there is a sudden drop in current. An automatic cutoff circuit immediately stops the flow of electricity to avoid blunting of the tip.

2.2.2 Structural Characterization

As previously discussed, diffraction contrast imaging is a convenient way to image the real-time domain structure. It can also be used analytically through careful selection of the Bragg diffraction planes to determine the orientation relationships and planar distortions. For example, pure misfit dislocations with an in-plane burgess vector a<100> are invisible if the image is formed by diffraction of the normal (001) planes. This is important for imaging domains and domain walls since, in general, they will show very little contrast if the domain wall planes are the Bragg planes forming the diffracted image. As reported in detail by Streiffer et. al. the domain walls in $BiFeO_3$ (i.e. the boundaries between regions with different polarizations) have preferred minimum energy

planes, and the two domains will typically orient so that this plane is coherent[97]. Thus, diffraction of this plane will not yield any distinction between the two neighbor domains. If the domain wall is ferroelastic it will be also be a twinning plane and all the orthogonal planes are canted providing a very strong diffraction contrast. This is demonstrated in Fig. 2.6 by a 109° domain wall twinning structure of a 100 nm $BiFeO_3$ film on bare $(110)_O$ $TbScO_3$. Here, the coherent plane between the $BiFeO_3$ twins is the $(001)_O$ (using the orthorhombic indices of the substrate) as highlighted in the planar view (Fig. 2.6a) and cross sectional (Fig. 2.6b) images. Electron diffraction patterns of both orientations (Fig. 2.6c,d) show a clear split in the planes orthogonal to the coherent planes as shown in the magnified inset regions. A measure of the angle between these spots corresponds to a projected 0.5° distortion from cubic, in good agreement with the bulk $BiFeO_3$ structure. This means that the $BiFeO_3$ is essentially relaxed to its bulk structure, including canting of the $(110)_O$ planes despite being epitaxially constrained to the substrate. The respective TEM images were formed using diffraction of these canted planes, $(1\bar{1}0)_O$ in planar view (Fig. 2.6a) and $(110)_O$ in cross section (Fig. 2.6b), providing the strong bright/dark contrast. The exaggerated rhombohedral structure of the ferroelastic r_1 and r_4 twins and their twinning orientation is illustrated by the white rhombuses in the TEM images.

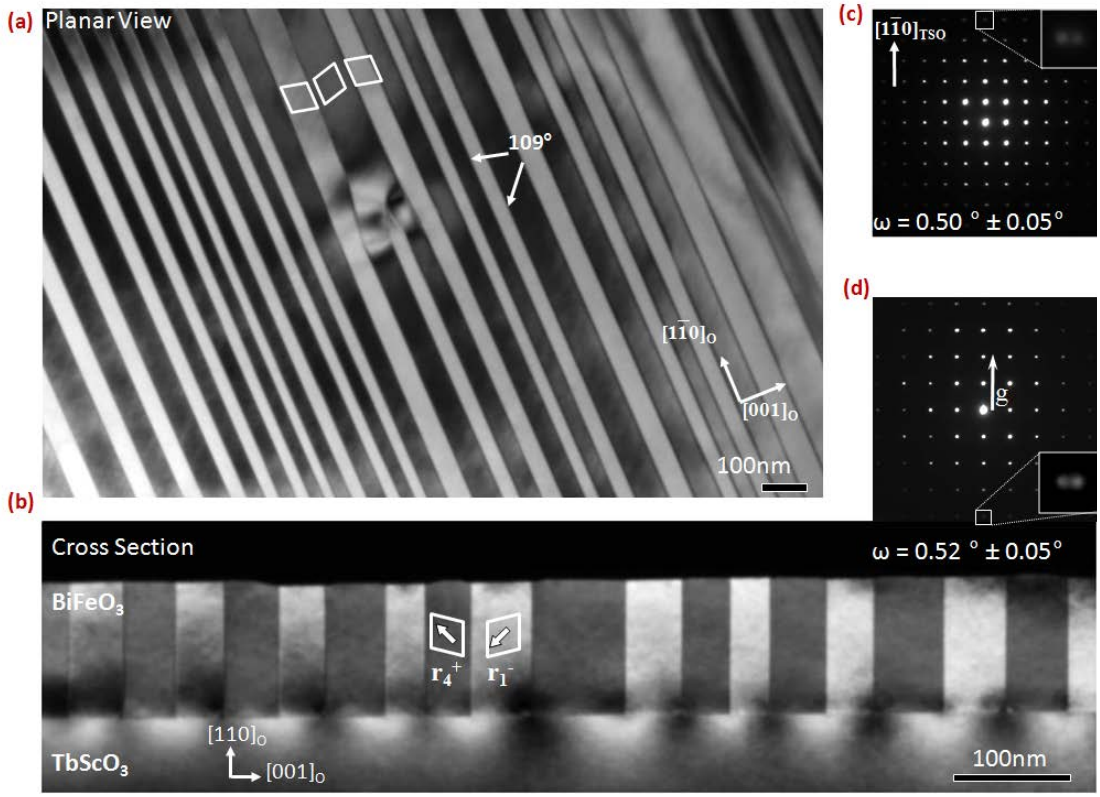

Fig. 2.6 Diffraction Contrast Imaging of $BiFeO_3$ Ferroelastic Twins
Dark field diffraction contrast images of a 100 nm $BiFeO_3$ film 109° twin structure shown in **(a)** planar view and **(b)** cross section. The corresponding electron diffraction patterns in **(c)** and **(d)** respectively show a canting of the planes orthogonal to the coherent $(001)_O$ twin boundary plane. Diffraction from these canted planes was used to form (a) and (b) and is responsible for the high contrast.

2.2.3 Piezoresponse Force Microscopy (PFM)

Piezoresponse force microscopy (PFM) is a surface probe measurement technique which is the predominant contemporary method of characterizing the long range domain structure of ferroelectric films. PFM is non-destructive, unlike the involved sample preparation procedure for TEM, but can provide high lateral spatial resolution of the domain structure. It is also capable of very high (equivalent) time resolution of cyclic ferroelectric switching behavior using stroboscopic imaging[98]. Since PFM is a surface probe measurement it is not a stand-alone technique; there are a host of other measurements such as conductivity mapping and atomic force microscopy which can be done in concert with PFM. Thus, it has been the source of most of the recent experimental advances in the theory and characterization of ferroelectric switching.

PFM works by measuring the (converse) piezoelectric response of the film to an applied bias via the deflection of a conductive tip in contact with the film surface. Piezoelectricity is defined as the buildup of charge in response to mechanical stress. The converse is also true, an applied field produces a mechanical response. Under constant stress the three principle deformations (strain S) for a tetragonally symmetric material are given by:

$$\begin{bmatrix} S_{11} \\ S_{22} \\ S_{33} \end{bmatrix} = \begin{bmatrix} 0 & 0 & d_{31} \\ 0 & 0 & d_{32} \\ 0 & 0 & d_{33} \end{bmatrix} \begin{bmatrix} E_1 \\ E_2 \\ E_3 \end{bmatrix} \quad \text{2-2}$$

where E is the applied field and d_{xx} are the piezoelectric coefficients (the shear strains were ignored but their contribution is small). For a field applied normal to the film (E_3), the dominant deflection measured by PFM is the normal strain S_{33} which raises or lowers the tip. This also corresponds to the largest response of the ferroelectric piezoelectric, d_{33}, which will cause the film to contract when the field is opposed to its polarization or expand if it is parallel. The driving voltage and corresponding strain are oscillated and connected to lock in amplifiers to provide high sensitivity. The phase offset between the driving voltage and the tip deflection is used to indicate if the polarization is parallel or antiparallel to the applied field.

If the polarization of the film does not lie purely along the film normal, such as in-plane polarizations of $PbZr_{0.2}Ti_{0.8}O_3$ or all the polarizations of $BiFeO_3$, then the out of plane S_{33} deflection will not fully characterize the polarization under the tip. In this case, the two cross terms, d_{31} and d_{32}, are necessary and correspond to the lateral expansion/contraction in response to the normal field E_3. It is helpful here to rotate the sample with respect to the tip so that one of these terms will cause the cantilever to twist about its length. This lateral signal can be measured separately from but simultaneously with the out-of-plane deflection. A measurement of the orthogonal in-plane term then requires the tip to be rotated 90°.

Normally the driving voltages are kept small to avoid altering the ferroelectric structure during measurement. However, one of the powerful features of PFM is its ability to

characterize ferroelectric switching under a large applied voltage by detecting the crossover between the in-phase and out-of-phase oscillations of the sample. These "butterfly loops" of the piezoresponse vs. voltage provide local information on the switching characteristics including the threshold biases for switching in each direction. This data can be compiled to form maps of the switching characteristics of a film, a technique called switching-spectroscopy PFM (SS-PFM)[99]. Alternatively, high-speed switching imaging can be done by strobing the measurements with a delay behind the switching pulse to form a fixed delay image. Although this does not measure a single switching event, switching behavior is usually very repetitive due to the dominance of stationary defects and the technique has been effective in imaging capacitor switching[98].

While PFM is extremely useful for characterizing the ferroelectric behavior of a film it has several major shortcomings. Foremost, it is an aggregate measurement of the surface deflection which must take into account several piezoelectric terms and tip/surface interactions. Achieving very high resolution requires extrapolating these contributions and additionally deconvoluting by the shape of the tip, and even still the achievable resolution falls short of the nanoscale dimension of the defects which control the switching process. Secondly, surface probe measurements do not have depth imaging into the nanoscale dimension of the material, i.e. the film normal axis. This is an important blind spot as it is the behavior along these confined dimensions which define the properties of low-dimension ferroelectric systems. Lastly, PFM has no direct means of characterizing any of the non-surface defects which influence the SS-PFM images. These require ex-situ analysis of the film structure such as by TEM. PFM and TEM are complimentary techniques. The former is large area with a high statistical sampling while the latter is high resolution with good structural characterization. Correlation between the two can bridge our understanding of ferroelectric behavior from the nano to the microscale.

2.2.4 Light element imaging

Detailed atomic-level characterization of the ABO_3 perovskite structure is a prerequisite for the polarization analysis later in this work (see section 3.3). Unfortunately, the position of oxygen is very difficult to determine using the two standard high resolution

techniques: HRTEM and HAADF STEM. The small scattering potential of the oxygen ions renders them invisible in HAADF images and their positions in HRTEM cannot be interpreted directly from the image. With the recent advances in aberration correcting optics and resolution no longer a bottleneck, several techniques have been developed to image the low Z elements, including a report this year of imaging columns of hydrogen[100]. These techniques are all types of phase contrast imaging. For very thin samples, the effect of an atomic potential on the propagating wave is a change in phase, known as the weak-phase object (WPO) approximation. Thus, techniques designed to measure the phase of the electron wave provide a clear image of the atom potentials, including low Z elements.

The first report of successfully imaging oxygen in perovskites was by Jia et. al. in 2003 utilizing the then new Cs-correcting optics to apply a phase shift to the electron wave[101]. The addition of the WPO phase shift ($\pi/2$) and the induced phase shift ($\pi/2$) resulted in the WPO phase appearing as the amplitude on the detector, and showing the atomic potentials as dark spots on a bright background.

A more complete version of this type of phase imaging, exit wave reconstruction, involves reconstructing the entire electron wave at the exit plane of the sample[102]. The amplitude is recorded at a series of different focus depths and numerical calculations are used to determine the phase information prior to objective lens. In our work, the commercial program MacTempas is used for exit wave reconstruction. A series of 41 TEM images taken at 2nm defocus steps centered around the Scherzer focus was used and the microscope aberrations measured from the self-reported values of the Cs image corrector (CEOS). MacTempas determined the true defocus depth from the thon rings and the spatial drift by cross correlation. The corrected values are then input into a Gerchberg-Saxton algorithm to recover the phase of the exit wave. Due to the sensitivity to the lens aberration values, a final tuning of the exit wave is necessary and done manually through iterative adjustment of the simulated lower order lens aberrations and focus. These parameters were adjusted until the atomic columns, primarily of the Bi and Sc sites, appeared round and symmetrically changed contrast with a change in focus.

Bright-field STEM has already been mentioned briefly for being able to image low-Z elements and operates on the same principle of phase interference from the atomic potentials. For thin areas where the WPO approximation holds, bright field STEM images of perovskites appear dark at the atomic potentials, as has been specifically shown in both $BiFeO_3$[103] and $PbZr_xTi_{1-x}O_3$[104]. As demonstrated by the imaging of hydrogen, BF-STEM can be further improved by removing the axial component of the beam and instead using an annular bright-field detector (ABF-STEM)[100]. The authors report that such an approach reduces chromatic aberrations (variations in the incident beam energy) – the most significant contribution to resolution limits after the Cs-aberration is compensated.

A final light-element imaging method which is not based on phase-contrast is STEM mapping of inelastic scattering as from EELS or EDS. However, this approach suffers from serious drawbacks due to very long acquisition times which require significant drift stability and/or correction. There is also a significant delocalization of the probe for inelastic scattering whereby an incident electron can ionize an atom at a (relatively) large distance. Therefore the resolution of inelastic scatter mapping is much worse than the phase-contrast techniques.

2.3 Thin Film Growth

$BiFeO_3$ and $PbZr_{0.2}Ti_{0.8}O_3$ thin films were provided by collaborations with Dr. Darrell Schlom of Cornell University and Dr. Chang-Beom Eom of the University of Wisconsin. $BiFeO_3$ films in this work were grown by both groups using two different growth methods: molecular beam epitaxy (MBE)[*] and 90° off-axis radio-frequency magnetron sputtering (rf sputtering)[†]. The former employs a neutrally charged molecular flux while the latter uses an ionized flux. A comparison of ~100 nm $BiFeO_3$ films on the same $(110)_O$ $TbScO_3$ surface is shown in Fig. 2.7. Both form the same 109° twin pattern which is indicative of similar electrostatic boundary conditions and an absence of appreciable free charge (see section 3.6). In general, the MBE films had the more regular domain structure and domain wall orientations which adhered more closely to the equilibrium

[*] Provided by collaboration with Dr. Darrell Schlom – *Cornell University*
[†] Provided by collaboration with Dr. Chang-Beom Eom – *University of Wisconsin - Madison*

planes so these films were used preferentially. The sputtered films had better electrical characteristics, a topic discussed in greater detail in section 5.2.4.

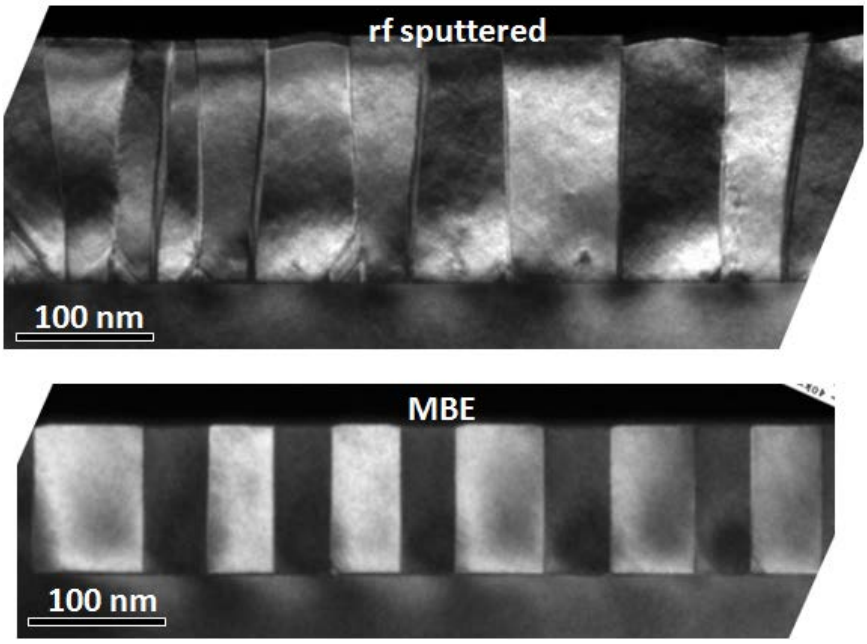

Fig. 2.7 Domain Structure vs. Growth Method
Dark field images of 109° twin structures of $BiFeO_3$ films grown by **(a)** rf-sputtering and **(b)** molecular beam epitaxy

MBE grown $BiFeO_3$ films of two different thicknesses were used in this work: 100 nm and 20 nm[*]. The $BiFeO_3$ films were grown on bare single crystal $(110)_O$ $TbScO_3$ surfaces and with 20 nm $La_{0.7}Sr_{0.3}MnO_3$ buffer electrodes in an EPI 930 MBE chamber equipped with reflection high-energy electron diffraction (RHEED). The 20 nm thick conducting $La_{0.7}Sr_{0.3}MnO_3$ buffer layer was deposited using a codeposition procedure utilizing effusion cells containing La, Mn, and Sr elements. The fluxes of the individual molecular beams were set to 3×10^{13} Mn atoms/(cm^2·s), 2.1×10^{13} La atoms/(cm^2·s) and 0.9×10^{13} Sr atoms/(cm^2·s). With the substrate at 700 °C these molecular beams together with an oxidant of O_2+10% O_3 (at a background partial pressure of 5×10^{-7} Torr) were simultaneously supplied to the substrate to form the $La_{0.7}Sr_{0.3}MnO_3$ film. Following growth, the sample was cooled in the same oxidant (O_2+10% O_3) background partial

[*] Provided by collaboration with Dr. Darrell Schlom – *Cornell University*

pressure in which it was grown until the temperature of the substrate dropped below 200 °C.

The $BiFeO_3$ films were grown in the same MBE utilizing an adsorption-controlled codeposition procedure as described in ref 105. The Fe flux was about 2.0×10^{13} atoms/(cm^2·s) and the Bi flux was 1.1×10^{14} atoms/(cm^2·s). During the deposition, distilled ozone (~80% ozone) was used to create a background oxidant pressure of 1×10^{-6} Torr. The substrate was maintained at a constant temperature of 610 °C for growth directly on the $(110)_O$ $TbScO_3$ substrate and 625 °C for growth on the $La_{0.7}Sr_{0.3}MnO_3$ prelayer.

A thickness series of $BiFeO_3$ films† on bare $(110)_O$ $TbScO_3$ was grown by off-axis radio-frequency magnetron sputtering according to ref 106. Four films were grown sequentially with thicknesses ranging from 45 nm to 385 nm. All deposition parameters were kept constant and the samples were grown in immediate succession to avoid deviations in processing conditions. The growth temperature was 690°C, still below the Curie temperature.

The $PbZr_{0.2}Ti_{0.8}O_3$ film used in this work† was grown by rf-sputtering and consist of a 100 nm PZT film on a 50 nm epitaxial $SrRuO_3$ (SRO) layer deposited as a bottom electrode on a single crystal (110)o $DyScO_3$ (DSO) substrate at 630 ^oC[107,108]. 200 mTorr was maintained during deposition with a 3:2 ratio of Ar and O_2 gas. Epitaxial 100nm $PbZr_{0.2}Ti_{0.8}O_3$ films were grown on top of the $SrRuO_3$ bottom electrode by 90^o off-axis sputtering at 530 ^oC. A mixture of Ar and O_2 gas with a 1:1 ratio was used with a total pressure of 200 mTorr[109].

2.4 Phase-Field Modeling of Ferroelectric Materials

In this work it is necessary quantify the energy contributions which determine the equilibrium domain structures in $BiFeO_3$ films. This was done by modeling and simulations using the Phase-Field approach provided by collaboration with Dr Long-Qing Chen of Pennsylvania State University. Phase-Field simulations have emerged as a very

† Provided by collaboration with Dr. Chang-Beom Eom – *University of Wisconsin - Madison*

successful approach for determining mesoscale domain structures in ferroelectric films[110]. In this method, the energetic contributions are defined according to a single variable, here the polarization. The domain structure is described by the spatial polarization distribution $\mathbf{P}=(P_1(\mathbf{x}), P_2(\mathbf{x}), P_3(\mathbf{x}))$, where $\mathbf{x}$ is the position vector, and its stability is determined by the total free energy which includes all the important energetic contributions,

$$F = \int_V (f_{bulk} + f_{grad} + f_{elas} + f_{elec})dV \qquad 2\text{-}3$$

With each of the individual energy contributions expressed in terms of the spatially inhomogeneous polarization distribution, the evolution of a less stable domain structure to a more stable one is described by the time-dependent Ginzburg-Landau (TDGL) equation,

$$\frac{\partial P_i(\mathbf{x},t)}{\partial t} = -L\frac{\delta F}{\delta P_i(\mathbf{x},t)}, i = 1,2,3, \qquad 2\text{-}4$$

where L is a kinetic relaxation coefficient related to the domain wall mobility. The energy contribution to equation (2-3) of primary interest in this work is the f_{elec} term, the electrostatic energy density of an inhomogeneous polarization distribution given by,

$$f_{elec} = -\frac{1}{2}E_i P_i \qquad 2\text{-}5$$

or

$$f_{elec} = -\frac{1}{2}\varepsilon_b \varepsilon_0 {E_{total,i}}^2 - E_{total,i}P_i \qquad 2\text{-}6$$

where the first expression 2-5 is valid without an external field, and the second expression 2-6 is applicable under an applied electric field with the total electric field given by the sum of depolarization and applied electric fields, ε_b is the background dielectric constant[111,112], ε_o is the vacuum permittivity, E_i is the i^{th} component of the electric field produced by the polarization distribution, i.e., the depolarization field with

no externally applied field, which can be obtained by solving the electrostatic equilibrium equation for the electric potential, ϕ,

$$-\varepsilon_b\varepsilon_0\nabla_i\nabla_j\phi(x) = \varepsilon_b\varepsilon_0\nabla_i E_j(x) = -\nabla_i P_i(x) = \rho_b(x) \qquad 2\text{-}7$$

in which ρ_b is the polarization or bound charge. The electrostatic equilibrium equation is solved using either short-circuit or open-circuit boundary conditions, i.e.,

$\phi(r)$ = constant for a short-circuit and perfectly screened boundary condition

$\nabla_3\phi(r)\big|_{surface} = \dfrac{P_3}{\varepsilon_b\varepsilon_o}$ for an open-circuit or unscreened boundary condition

The first term in the free energy equation (2-3), f_{bulk}, is the bulk free energy density described by the Landau free energy as a function of polarization under a stress-free state with the Landau coefficients given in ref 113 for $BiFeO_3$. The second term in the integrand of equation (2-3), f_{grad}, is the gradient energy density due to the polarization changes across the domain walls,

$$f_{grad} = \frac{1}{2} g_{ijkl} \frac{\partial P_i}{\partial x_j} \frac{\partial P_k}{\partial x_l} \qquad 2\text{-}8$$

where g_{ijkl} is the gradient energy coefficient and $\mathbf{P}=(P_1(\mathbf{x}), P_2(\mathbf{x}), P_3(\mathbf{x}))$,. In a ferroelectric domain structure, $f_{bulk} + f_{grad}$ essentially describes the domain wall energy density distribution.

The third term in equation (2-3), f_{elas}, is the elastic energy density,

$$f_{elas} = \frac{1}{2} c_{ijkl}(e_{ij}(x) - e_{ij}^0(x))(e_{ij}(x) - e_{ij}^0(x)) \qquad 2\text{-}9$$

where c_{ijkl} is the elastic stiffness tensor, e_{ij} is the total strain, and e_{ij}^o is the stress-free strain given by $e_{ij}^0(x) = Q_{ijkl}P_k(x)P_1(x)$ in which Q_{ijkl} is the electrostrictive tensor. Both e_{ij} and e_{ij}^o are defined using the pseudocubic phase as the reference. The total strain can be obtained by solving the mechanic equilibrium equation under the given film boundary

condition using a combination[114] of Khachaturyan's elasticity theory and Stroh's formalism.

Equation (2-4) is solved using a semi-implicit Fourier spectral method with periodic boundary conditions along x_1 and x_2 axes. Along the x_3 axis, we simply make the polarization outside the film 0.0, equivalent to a negative extrapolation length of approximately one grid size. A simulation cell of $128\Delta x \times 128\Delta x \times 32\Delta x$ is used. The film thickness is taken as $14\Delta x$ and the distance from the film–substrate interface into the substrate is taken as $14\Delta x$, beyond which the heterogeneous elastic deformation is ignored

The simulation grid spacing is chosen to be $\Delta x = l_0$ where $l_0 = \sqrt{G_{110}/\alpha_0}$ and $\alpha_0 = |\alpha_1|_{T=300K}$. In simulations, the values for Landau coefficients for $BiFeO_3$ are $\alpha_1=4.9\times10^5(T\text{-}1103)$, $\alpha_{11}=5.44\times10^8$, $\alpha_{12}=1.92\times10^8$ (SI units) where T is Kelvin temperature [113]. Homogeneous and isotropic elastic and dielectric constant was used and the nonzero constant are $c_{11}=3.0\times10^{11}$, $c_{12}=1.62\times10^{11}$, $c_{44}=0.691\times10^{11}$, $\kappa_{11}=\kappa_{22}=\kappa_{33}=50.0$, where c_{ij} is the Voigt's notation of the elastic stiffness. The electrostrictive coefficients of $Q_{11}=0.032$, $Q_{12}=-0.016$, $Q_{44}=0.06$ ($C^{-2}m^4$) were used where larger Q_{44} was taken for distinguishing the difference between the rhombohedral variants. We took the gradient energy coefficient to be $G_{11}/G_{110}=0.3$, $T=300K$, $\Delta t/t_0=0.08$, $t_0=\alpha_0 L$. In-plane anisotropic strains of $\varepsilon_{11} = -0.1\%$, $\varepsilon_{22} = -1.0\%$ and $\varepsilon_{12} = 0\%$ were applied to the bottom surface while the top surface is free.

Chapter 3

3 Ferroelectric Interfaces

3.1 Background

Interfaces of materials often posses unique properties compared to the bulk due to the broken symmetry and chemical reconstruction of the surface. This is especially true of strongly correlated systems such as the transition metal oxides where the electron interactions and lattice degrees of freedom are strongly tied. Useful properties can exist confined into this essentially 2-dimensional interface layer such as electronic conduction at the interface between the insulators $SrTiO_3$ and $LaTiO_3$[12] or $LaAlO_3$[11]. The twinning domain walls in ferroelectric materials have themselves been reported to exhibit a variety of unique behaviors including 2-d conduction[13], photocurrent generation[115] and ferromagnetic moments despite the host material being antiferromagnetic[14]. However, unlike material heterointerfaces, domain walls can be easily manipulated by electric fields allowing these properties to be actively modified. For example, the authors of ref 13 demonstrated a multi-state resistive memory device were the conduction current scaled with the number of domain walls deliberately formed between the electrodes. In section 3.4 of this chapter I undertake a study of the detailed atomic structure of the domain walls in $BiFeO_3$ which exhibit these unique properties.

The strong correlation in ferroelectric materials also lends itself to strain engineering whereby the symmetry of an overlying ferroelectric film is modified by epitaxial constraint to a substrate. Substrate induced in-plane strains can lead to dramatically enhanced ferroelectric properties[5,6,84]. Even if the results aren't always as dramatic, global strain can affect the properties of any ferroelectric film including the ferroelectric domain structure[97,110] and even the ferroelectric phase[86,110]. The two prominent ferroelectrics in this work, $BiFeO_3$ and $PbZr_{0.2}Ti_{0.8}O_3$, are no exceptions and $BiFeO_3$ is in fact one of the two aforementioned examples of highly enhanced properties. A shear

strain imposed by growing rhombohedral ferroelectrics like $BiFeO_3$ onto orthogonal substrates leads to the formation of twinning domains[97] (see section 3.6). Small in-plane strains in $BiFeO_3$ produce a monoclinic distortion which breaks the degeneracy of the 6 antiferromagnetic easy directions[87] and leads to a rotation of the polarization vector away from the body diagonal[116]. Compressive strains exceeding (~-3%) produce a transition to a c-oriented tetragonal phase[86]. In tetragonal ferroelectrics such as $PbZr_{0.2}Ti_{0.8}O_3$ strain dictates the domain structure according to a_1/a_2 (tensile), c/a (small strain), or c/c (compressive)[110]. So for example a PZT capacitor design which relies on polarization normal to the film (c-axis) requires a compressive strain to form a c oriented domain structure.

Even disregarding any functional interface properties or strain engineering, the substrate/film heterointerface plays a critical role in ferroelectric properties and behavior. The process of switching between ferroelectric orientation states is dominated by defects, the most prominent being the two film interfaces[46]. In the in-situ switching experiments presented in chapter 5 nucleation occurs unilaterally at the interface and such behavior in bulk has been known for over 60 years. The presence and direction of atomic surface steps on the substrate can break the degeneracy of the polarization directions and control the domain structure[80,117]. If the film exceeds a critical thickness (h_c), the global strain imposed by the substrate is relaxed by the formation of a dislocation network[118] at the interface according to[119]:

$$h_c = \frac{b}{8\pi/(1+\upsilon)} \cdot \ln\left(\frac{h_c}{b} + 1\right) \qquad 3\text{-}1$$

Where b is the Burgers vector of the dislocations and ν is Poisson's ratio. If this occurs not only are any benefits from strain engineering lost but the dislocations themselves can negatively impact ferroelectric properties[120]. The large strain gradients generated at the interface by film relaxation through misfit formation can produce large polarizations through the flexoelectric effect resulting in a severe switching asymmetry or even an unswitchable polar layer at the interface[111,121].

The inherent broken symmetry of the ferroelectric film also leads to large bound surface charges at the surface. This is due to the polarization gradient which must accompany any interface where the polarization goes to zero. According to Gausses law

$$\nabla D = \rho \qquad 3\text{-}2$$

where D is the electric flux density and ρ is the charge density. There are two contributions to the electric flux:

$$D = \varepsilon_0 E + P \qquad 3\text{-}3$$

where E is the electric field and P is the polarization. Thus electric fields can come from two sources: the divergence of the first term corresponds to the free charge and the divergence of the second term corresponds to the "bound" charge. Since the ferroelectric interface is necessarily a source or sink of polarization (i.e. the divergence is non-zero) there is by definition a bound charge at this surface which will induce an electric field in the ferroelectric. This is called the "depolarizing" field because it is oriented to oppose the polarization. The bound charge is a critical feature of ferroelectric interfaces because it cannot be perfectly screened[73,76,78], even by the addition of electrodes, so that depolarizing fields are inevitably produced by the interface. Section 3.6 develops this topic further using experiments of the electrostatic boundary conditions in $BiFeO_3$ films.

We are predominantly concerned with electrical phenomenon in $BiFeO_3$ ferroelectric films and thus we have selected well matched $TbScO_3$ substrates and grown the films below the Curie temperature to try and isolate them from strain effects or misfit dislocations. Even still, given the non-orthogonal rhombohedral symmetry of $BiFeO_3$ there is an unavoidable symmetry mismatch between the substrate (in this case orthorhombic) and the $BiFeO_3$ film (rhombohedral) and the transition between these structures at the interface is not spatially instantaneous. The crystal structure of the substrate will penetrate into the ferroelectric film and vice versa. For example the octahedral rotation of $BiFeO_3$ is damped in the vicinity of a cubic substrate[122]. This is one proposed contribution for experimentally observed "passive layers" near the interface

in ferroelectric films[111]. This effect from the $TbScO_3$ substrate is bigger pertinent question since it has lower symmetry than $BiFeO_3$ and much larger distortions of the cubic perovskite structure. The $TbScO_3$ surface has been shown to break the degeneracy of the four ferroelastic domains in $BiFeO_3$[106] although the mechanism has heretofore been unclear. In addition to symmetry mismatch there is often interdiffusion of atomic species and in fact some interfaces are incapable of being atomically sharp[94]. In section 3.5 I will study the detailed atomic scale structure of the $BiFeO_3$ / $TbScO_3$ interface.

3.2 Experimental

To limit in-plane strain we choose a model system consisting of $(001)_P$ oriented $BiFeO_3$ thin films on insulating $(110)_O$ $TbScO_3$ single crystal substrates (where the P and O subscripts represent pseudo-cubic and orthorhombic indices). The orientation relationship between the two materials is defined as $[001]_p \parallel [110]_{O\text{-}TSO}$, $[100]_p \parallel [-110]_{O\text{-}TSO}$, and $[010]_p \parallel [001]_{O\text{-}TSO}$. The $BiFeO_3$/$TbScO_3$ interface has a compressive lattice mismatch of (<0.13%)[123]. The $BiFeO_3$ films used in this section were grown to 20 nm thickness*, half the dislocation formation critical thickness (h_c) determined by the thermodynamic theory (eq 3-1)[119]. However, the $BiFeO_3$ films used in section 3.6†, a study of film thickness dependence, are an exception and grown up to 400 nm thick. However, no dislocations were observed even at these $>h_c$ thicknesses suggesting that dislocation formation is kinetically frozen out[124]. The film growth procedures of the 20 nm MBE films and sputter-grown thickness series used in this section are detailed in section 2.3.

Diffraction contrast imaging of the domain $BiFeO_3$ domain structures was performed on a 300 kV JEOL 3011 at the Electron Microbeam Analysis Laboratory (EMAL) at the University of Michigan according to the procedure described in section 2.1.1. All HAADF STEM images were taken on the FEI titan TEAM 0.5 at the National Center for Electron Microscopy (NCEM) at the Lawrence Berkeley National Lab operating at 300 kV. EDS mapping of the $BiFeO_3$ / $TbScO_3$ interface was performed on an FEI titan g2

* Provided by collaboration with Dr. Darrell Schlom – *Cornell University*
† Provided by collaboration with Dr. Chang-Beom Eom – *University of Wisconsin - Madison*

80-200 with Chemi-STEM operated at 200kV. Geometric phase analysis (GPA) was performed using the GPA Digital Micrograph plugin from HREM research.

3.3 Polarization Mapping

In addition to structural information, we would like to extract polarization information from our TEM data. At large length scales the determination of ferroelectric domain structures in thin films is straightforward. The structural distortions of ferroelastic domains in particular are easily detected by x-ray and electron diffraction. Even non-ferroelastic domains can be detected in TEM due to the failure of Friedel's law (section 2.2.2) or by PFM (section 2.2.3). However, these approaches are limited in resolution since the former requires a volume of diffracting planes and the latter a volume of piezoelectrically distorted material under the probe. Using atomic-resolution TEM to determine the positions of all the constituent ions allows the polarization to be determined on the scale of a single unit cell. In highly ionic crystals, where electronic contributions to the polarization are minimal, the polarization can be determined directly from the dipole moment formed by the ion positions observed by TEM. If the electronic contributions are significant a first principles calculation is also necessary to quantify the total polarization. However, in this section I show that the remnant polarization of the displacive perovskite ferroelectrics, specifically $BiFeO_3$, is accurately measured by ionic displacements alone. This approach has been viable only recently with the advent of Cs aberration correcting optics and techniques to detect light element anions such as oxygen (section 2.2.4). It was Chun-Lin Jia and colleagues who pioneered some of the first oxygen imaging[101] and promptly applied it to determine polarization gradients in ferroelectric films[125-128]. Using a similar method I examine the dipole moment of a $BiFeO_3$ film and formulate an approximation of the polarization based on the Bi and Fe cation displacements. This provides a highly simplified approach to mapping the polarization distribution since oxygen positions are no longer necessary.

The structure of $BiFeO_3$ consists of two pseudocubic perovskite unit cells connected along the body diagonal (Fig. 3.1a). The oxygen octahedra and the central Fe cation are displaced along one of the $\langle 111 \rangle_P$ directions ($[111]_P$ in Fig. 3.1) from their respective positions at the face and body centers, followed by additional counter rotation of the

oxygen octahedra by ±13.8° around the <111>$_P$ axes[26]. The polarization can be visualized by assuming valence charges centered on each of the ion sites. For a single pseudocubic unit cell this results in the charge distribution shown in Fig. 3.1b, where the centers of charge for each ion type are shown roughly at the body center of the unit cell. The electric dipole moment along the [111]$_P$ axis is clear from the offset between the negative (O) and positive (Fe and Bi) charges. Applying the Born effective charges[38] to this model yields a polarization of 98 μC/cm^2 along <111>$_P$, in excellent agreement with the measured polarization of $BiFeO_3$[85,129].

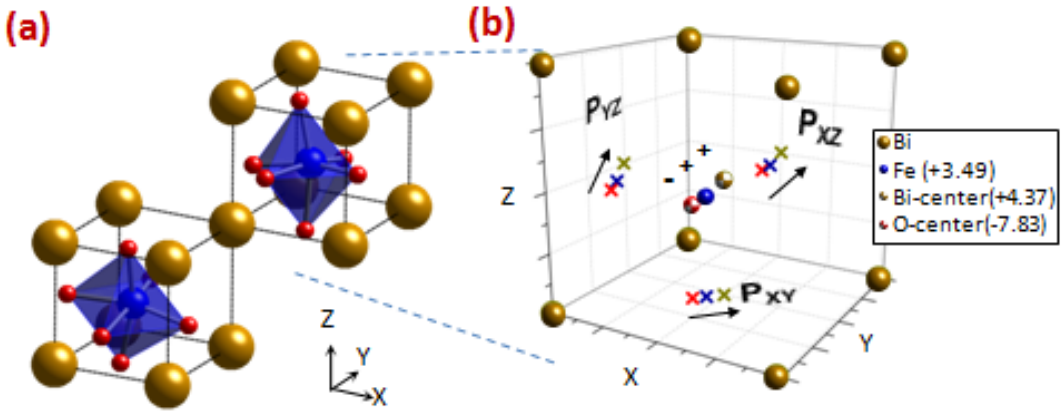

Fig. 3.1 Electric Dipole Moment of Bulk $BiFeO_3$
(a) The rhombedral unit cell of bulk $BiFeO_3$ represented as two adjacent pseudocubic perovskite cells. The oxygen octahedra and central Fe cation are clearly displaced from their respective positions at the face and body centers. **(b)** A polarization along the [111] axis results from the offset of the centers of the positive (Bi and Fe) and negative (O) charges.

Using high resolution TEM images, we are able to extract quantitative information about the local polarization vector. Fig. 3.2a shows the phase of the reconstructed electron wave upon exiting a $BiFeO_3$ thin specimen determined from a focus-series of HRTEM images (method detailed in section 2.2.4). There is an obvious displacement of the oxygen and iron relative to the center of the bismuth sublattice and the atomic positions visibly match the bulk structure polarized along the [111]$_P$ direction (hollow spheres overlaid on the inset image). If the Born effective charges[38] are assigned to the atom positions in Fig. 3.2a (indicated by crosses) determined using a two-dimensional Gaussian fit, the polarization in the image plane is $|\mathbf{P_{YZ}}|$=82 μC/cm^2 at an angle of Θ=50°. This is nearly identical to the value for the bulk structure from Fig. 3.1b

projected on the same plane, $|\mathbf{P_{YZ}}|$=80 μC/cm^2 at Θ=45°. The increase of the angle from 45° to 50° is consistent with the induced polarization rotation expected in (+0.13%) compressively strained $BiFeO_3$[116]. Assuming an equivalent in-plane polarization normal to the image yields a total polarization of $|\mathbf{P}|$=98 μC/cm^2, in agreement with the previous model and for the experimental polarization values for $BiFeO_3$ thin films[85,129].

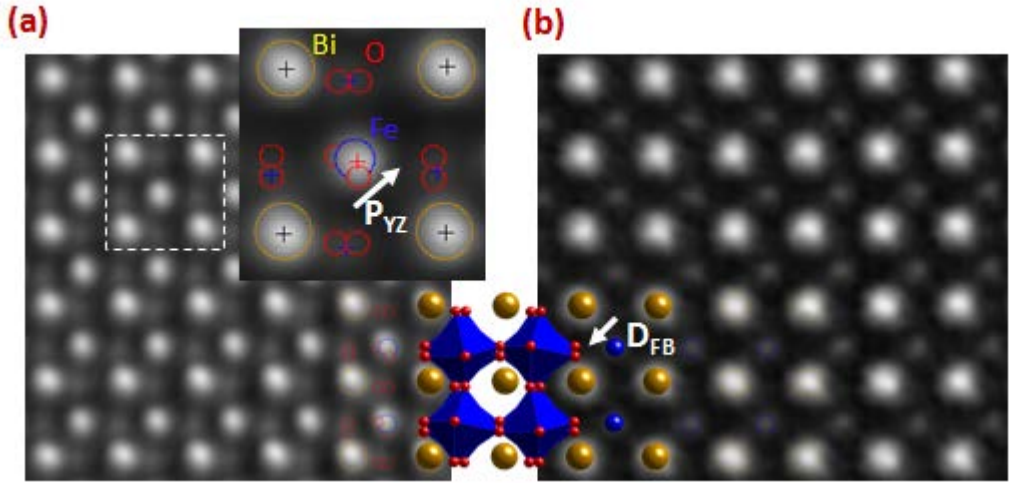

Fig. 3.2 $BiFeO_3$ Projected Dipole Moment in TEM
The electric dipole offset can be directly observed in the TEM micrographs of a $BiFeO_3$ thin film such as in **(a)**, the phase component of the exit wave determined from a TEM focal series. The atom centers, determined by fit as two-dimensional Gaussians, are shown as crosses in the inset and correspond to a projected polarization of P_{YZ} = 82 μC/cm^2. Since the ion charge centers are all collinear, a much more convenient determination of the polarization direction can be obtained from HAADF-STEM images such as **(b)** using the relative offsets of the Bi and Fe cations alone ($|\mathbf{D_{FB}}|$ = 33 pm).

While the exit wave retrieval approach is useful for determining the anion positions in the $BiFeO_3$ films, because the centers of charge of all three elements are collinear one of the elements is redundant for determining the polarization angle. The ferroelectric distortion is primarily A-site driven, thus the Bi atoms undergo the largest displacement and the largest separation is between the Bi and O charges. However, oxygen imaging is technically challenging and the fit is less precise compared to the cations; the fit of the cation peak positions in Fig. 3.2a have a 95% confidence interval of ±0.5 pm compared to ±2.5 pm for the oxygen peaks. Instead, the Bi displacement can be easily and more robustly determined from high-angle annular dark field (HAADF) imaging by scanning transmission electron microscopy (STEM) such as in Fig. 3.2b. Only the heavier cations are visible in these "Z-contrast" images, but they have the advantage that they require no

post processing and are less sensitive to specimen thickness. Here I define a vector $\mathbf{D_{FB}}$, which is the atomic displacement in the image plane of the Fe cation from the calculated center of the unit cell formed by its four Bi neighbors. $\mathbf{D_{FB}}$ is determined to be 33 pm along the $[01\bar{1}]$ diagonal, which is labeled in Fig. 3.2b. The simple relationship between $\mathbf{D_{FB}}$ and the polarization in the image plane is

$$P_{yz} = -2.5\frac{\mu C}{cm^2 \cdot pm} \cdot D_{FB} \qquad 3\text{-}4$$

where $\mathbf{D_{FB}}$ is the displacement in picometers. The linear relationship is straightforward; since $\mathbf{D_{FB}}$ points towards the center of the negative oxygen charges, it is opposite to the polarization direction. By mapping the spatial variation of $\mathbf{D_{FB}}$ in TEM images and using eq. 3-4 we can directly "image" the polarization in $BiFeO_3$.

To reduce noise, STEM images in this work are filtered in Fourier space using a grid mask to select for the structure frequencies and by low and high pass annular filters to remove the zero frequency and high frequency noise above the information transfer limit. In order to determine the coordinates of the atoms centers for mapping, a custom Matlab routine performs a simultaneous fit of all the atoms in the perovskite unit cell as either Gaussian or Lorentzian peaks. To perform this function on the scale of typical HAADF images which contain hundreds to thousands of unit cells, this routine is automated. A simulated image is created based upon an a-priori crystal structure. The simulated image is then automatically scaled and rotated according to the periodicity of the low-index planes in the fft pattern. The coordinates that this structure appears in the actual HAADF image is determined by cross-correlation. Overlapping atoms from neighboring unit cells are removed using a minimum distance threshold. The positions of the remaining atoms are then determined by an iterative fit using the trust-region algorithm in Matlab.

The formation of polarization maps using the real dipole moment and using only the cation positions based on equation 3-4 is carried out by custom Matlab and ImageJ routines, respectively. For the cation-based maps the displacement vector of the iron to bismuth, $\mathbf{D_{FB}}$, is equal and opposite that of bismuth to iron, $\mathbf{D_{BF}}$, (see Fig. 3.3) so both sets of data points are used to give better spatial resolution. The ImageJ routine

recursively forms a lattice of A and B-site cations and uses the lattice addresses to find each cations displacement with respect to the center of mass of its four nearest neighbors. This methodology is not very robust as it cannot accommodate the addition of anions, non-perovskite type structures, or lattice defects without fundamental changes to the code. The Matlab routine instead calculates the dipole moment at each ion site based upon the neighboring atoms located within a cutoff radius. Both routines then output polarization maps colorized so that it rotates smoothly around a Red-Green-Blue color wheel according to the angle the polarization vector forms with the horizon (θ) (see Fig. 3.3).

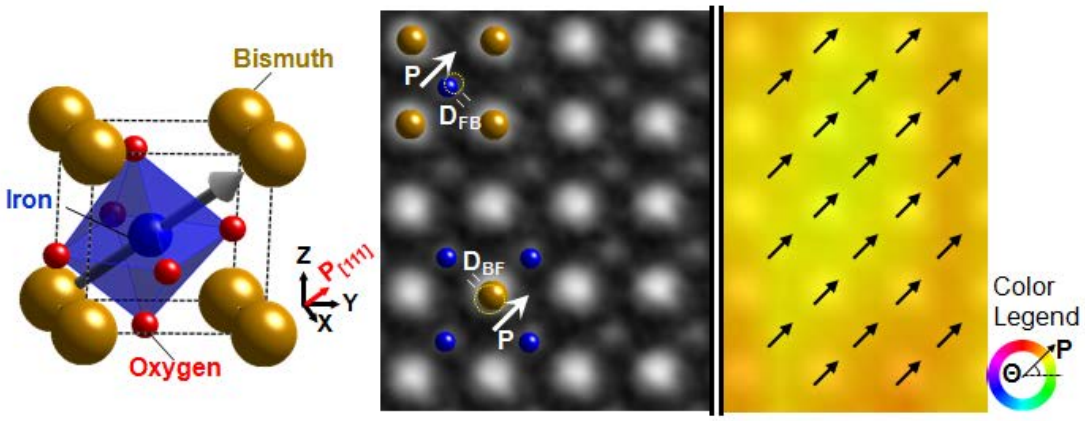

Fig. 3.3 Polarization Mapping by Cation Displacement
The 3-D $[111]_P$ polarized $BiFeO_3$ pseudocubic unit cell at left is projected onto the HAADF image at right for both the Bi centered and Fe centered cases. The polarization is interpolated between each of these unit cells to form a

The efficacy of the cation displacement based polarization mapping is especially good for $BiFeO_3$ since the ferroelectric phase is driven by the lone-pair electrons on the A-site Bi atoms. Fortuitously these are the very atoms which are easiest to see in Z-contrast HAADF images and their projected displacement distance is relatively large (33 pm). Thus, it is often clear even from a visual inspection of a domain wall boundary what type of polarization rotation is present. By measuring the relative translations of the Bi sub lattice at the domain walls it is therefore possible to identify the polarization rotation and infer the domain structure. For example both an in-plane and out-of-plane (normal to the film) offset in the Bi sublattice are apparent in the 180° domain wall in the left inset of Fig. 3.4a corresponding to both in and out-of-plane changes in the polarization vector. In

contrast, the 109° domain wall in the right inset has only an out-of-plane offset as the in-plane polarization is constant.

Because the Bi lattice accounts for most of the image intensity its periodicity is the primary contribution to the transform into frequency space (FFT). Using geometric phase analysis (GPA) deviations in periodicity produce strain-maps like that shown in Fig. 3.4c created from Fig. 3.4a. GPA works by taking orthogonal Bragg peaks in the FFT image and measures the frequency variation with respect to a reference region which it then maps it into real space[130,131]. The FFT peaks used to form the image in Fig. 3.4c are shown in Fig. 3.4b and the substrate was used as the reference lattice. The result is that the changes in the displacement of the Bi sublattice, i.e. the domain walls, become clearly visible as single unit-cell wide regions of "strain." The inclined 180° domain walls manifests in the ε_{xx} and ε_{yy} strain maps since they have both in-plane and out-of-plane discontinuities in the Bi periodicity as it crosses the wall. In contrast, the 109° domain wall has no in-plane change and is oriented parallel to the out of plane [001] direction so the spacing along [001] is also constant since it never traverses the domain wall. Instead the offset at the 109° domain wall manifests as an ε_{xy} shear strain. Using these fingerprints as a guide, the domain structure of Fig. 3.4 is identified as a large inclined 180° domain wall plus a vertical 109° domain wall with a small triangular region at its base which is reversed by 180°. As I will show in section 4.3, this agrees with the results of cation-displacement polarization maps. Such strain maps are an indirect approach and do not uniquely identify the polarization or provide any detailed information about the polarization distributions. However, in the case of $BiFeO_3$ it does provide a convenient check and confirms the consistency of the cation-displacement method.

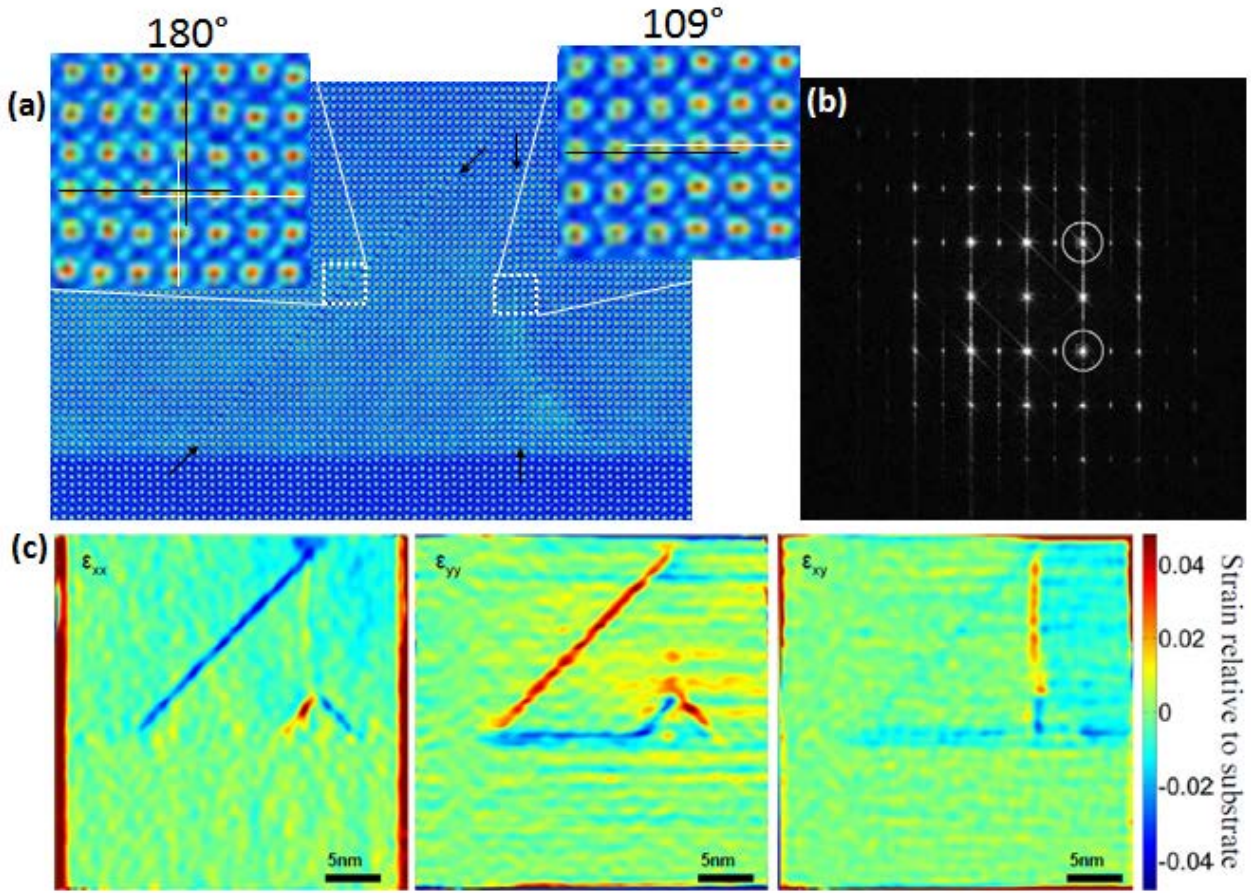

Fig. 3.4 GPA of Domain Walls in a $BiFeO_3$ Film
(a) A colorized HAADF image of a 20 nm $BiFeO_3$ thin film highlights the Bi sublattice offset across a 180° and 109° domain wall (inset). A GPA analysis using the peaks in the fft pattern shown in **(b)** produces the ε_{xx}, ε_{yy}, and ε_{xy} strain maps shown in **(c)**. 180° domain walls are apparent in the first two and 109° in the latter.

3.4 The Structure of 109° and 180° Domain Walls in $BiFeO_3$

The use of ferroelectric domain walls as functional elements is attractive since they are easily manipulated and, unlike their ferromagnetic cousins, they are exceedingly small. This is a product of the strong electrostriction in ferroelectrics (coupling between the polarization and the lattice) which creates a prohibitive energy cost for deviating from the preferred polar directions. Thus, ferroelectric domain walls are usually only singles of nanometers across and involve little if any contributions from phonon modes other than the spontaneous polar distortions. This is in contrast to ferromagnetic domains which have relatively weak magnetostriction and thus domain walls many microns wide with a gradually rotating magnetic moment.

Ferroelectric domain walls are categorized according to the angle of rotation of the polarization vector between the neighboring domains. For $BiFeO_3$ with eight possible <111> polarizations the rotation between any two polarizations is 71°, 109°, or 180°. The first two cases correspond to a change of the polarization axis, a ferroelastic rotation, while the 180° rotation is simply a reversal along the same axis. If $BiFeO_3$ is grown on an orthogonal substrate, as most substrates are, its rhombohedral footprint undergoes an in-plane shear strain in order to conform to the substrate. To relax this strain the film will intrinsically adopt a ferroelastic twin structure. The four possible ferroelastic variants (r_1-r_4 in the Streiffer notation[97]) corresponding to the four unique polar axis are shown in Fig. 3.5a. Alternating domains of any adjacent variants can relax the shear strain, for example $r_1||r_4$. However cross-variants have identical footprints, such as $r_1||r_3$, as do single variant domain walls $r_1||r_1$ and while such domain walls can sometimes be found they do not relax the shear strain. If the domains walls are restricted to only those planes which are both mechanically and electrically compatible (∇P=0 normal to the plane so it is charge neutral) then there are only two types of stable twin structures: parallel stripes with an alternating polarization rotating 71° along the in-plane direction separated by inclined {011} domain walls (Fig. 3.5b), or stripes with a 109° rotation of the polarization separated by vertical {010} domain walls (Fig. 3.5c)[97]. Both of these domain structures have been confirmed experimentally[132]. Similar constraints on 180° domain walls only

limit them to planes which contain the polarization vector[97]. In practice, however, we usually observe them in cross section along the {011} family of planes.

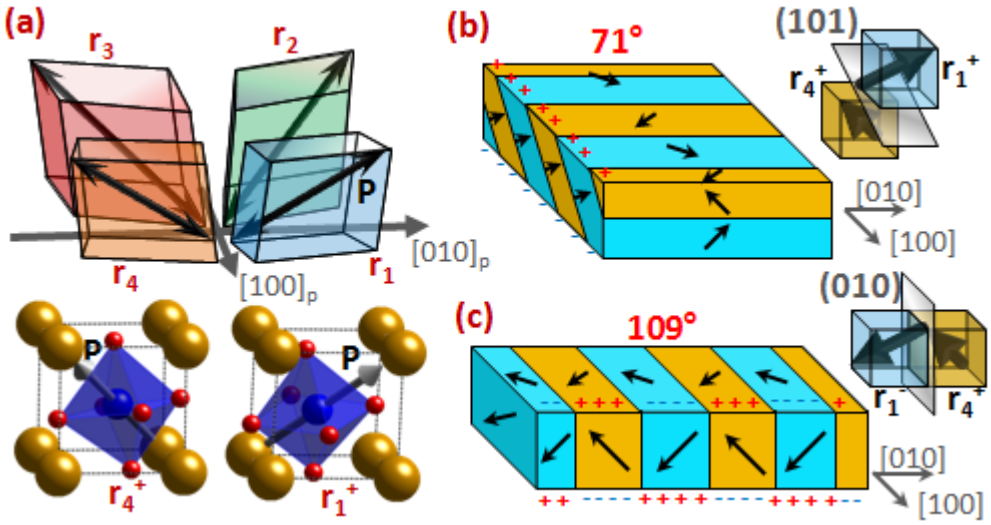

Fig. 3.5 Ferroelastic Twin Domain Structures in $BiFeO_3$
(a) The four ferroelastic variants of the $BiFeO_3$ pseudocubic unit cell, r_1-r_4, with exaggerated elongation of the polarization axis and the corresponding atomic model of upward polarized r_1 and r_4. Twins of these two variants will form domain patterns with 71° rotation of the polarization across $(101)_P$ walls **(b)** or 109° rotation of the polarization across $(010)_P$ domain walls **(c)**.

Despite the fact that domain walls have very little distortion of the host symmetry they never-the-less have been found to exhibit unique non-bulk properties such as conductivity[13]. However, the three domain walls do not behave identically; for instance conductivity was only detected in the 109° and 180° types. Seidel et. al. in ref 13 were only able to characterize the 109° case and attributed conduction to a small bound charge on the domain wall plane. However, subsequent first principles calculations determined that there is a reduction of the band gap depending on the distortion of the Fe-O-Fe bond angles – an effect that increases from 71° to 109° to 180° domain walls[44]. In this section we experimentally examine the domain wall structure of these three domain walls using Cs corrected high resolution STEM. 109° and 180° domain walls on their low energy (010) and $(01\bar{1})$ planes, respectively, can be viewed edge-on with the electron beam traveling along the [100] direction. Polarization-mapped images of 180° and 109° domain walls in the as-grown 20 nm $BiFeO_3$ film are shown in Fig. 3.6a-b and Fig. 3.6c-d respectively.

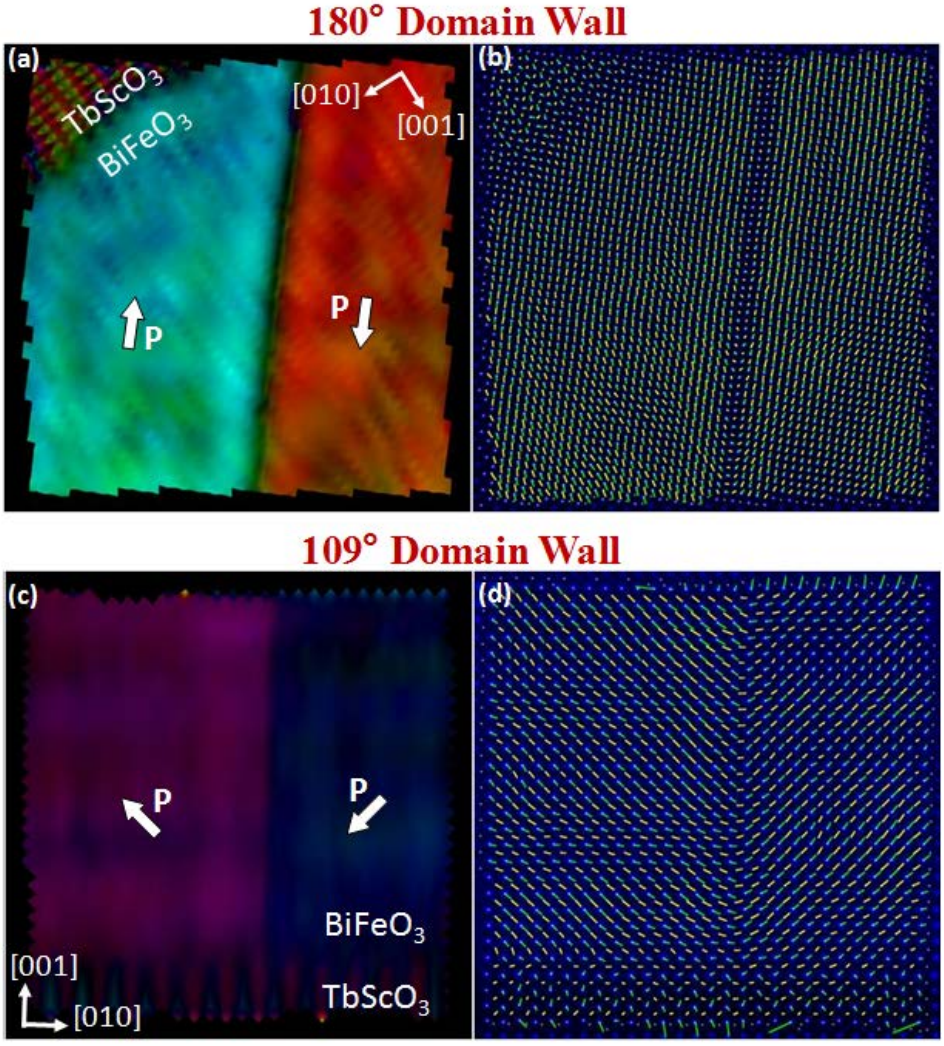

Fig. 3.6 Polarization Maps of 180° and 109° Domain Walls in a $BiFeO_3$ film
(a) Polarization map of a 180° domain wall and **(b)** the corresponding cation displacement vector map. The 180° domain wall is on the $(01\bar{1})$ plane. **(c)** Polarization map of a 109° domain wall and **(d)** the corresponding cation displacement vector map. The 109° domain wall is on the (010) plane.

The structure of the domain walls was evaluated by averaging the displacement at each atomic column versus distance from the domain wall. For the 109° domain wall this meant averaging along the alternating (010) BiO and FeO_2 planes and for the 180° domain wall along the $(01\bar{1})$ $BiFeO_3$ planes. The displacement vector was split into orthogonal components with respect to the domain wall plane – either normal or parallel to the domain wall. As a condition for charge neutrality the polarization normal to the domain wall is constant in both cases. The results for the 109° and 180° domain walls are shown in Fig. 3.7. The 109° domain wall consists of a single FeO_2 plane with non-

standard bonding. The polarization parallel to the domain wall on this column falls to near zero while the normal component remains constant. This domain wall width is considerably smaller than that reported in ref 13 and we do not observe a statistically significant discontinuity in the polarization normal to the domain wall. However, as I show in the next paragraph the agreement with first principles calculations is extremely close. The 180° domain wall is slightly wider than the 109° case with two atomic $BiFeO_3$ layers of damped polarization. The entire polarization is parallel to the domain wall so the normal component is kept constant near zero. There is some apparent smearing of the atomic columns at some regions of the domain wall so it may not be oriented exactly along the $(01\bar{1})$ plane. This is a by-product of the zero polarization normal to the domain wall – it is free to rotate without incurring any energy penalty from becoming charged. In projection this results in some domain overlap, smearing of the atomic columns, and a domain wall which is artificially wide. A look at the entire domain wall polarization vector map in Fig. 3.6b shows some regions which appear to have only a single damped atom layer.

Axel Lubk et al. provided us the structural data from their first principles calculations in ref 44. The models of the two domain walls are shown above and overlaid with the HAADF images. An identical calculation of the cation displacement was performed and is shown for each of the iron sites as a red vector in the model at top. These results are projected onto the yz image plane and graphed as dashed lines alongside the experimental data. The match for the 109° domain wall is remarkably good and strongly supports the validity of their findings. However, there is a fairly large departure in the 180° case. In order to preserve the symmetry the supercell had to be much wider than for the 109° case and due to computational limitations it was correspondingly much shorter. From these results it appears that it was too short and the $BiFeO_3$ was unable to relax to its stable structure away from the domain wall.

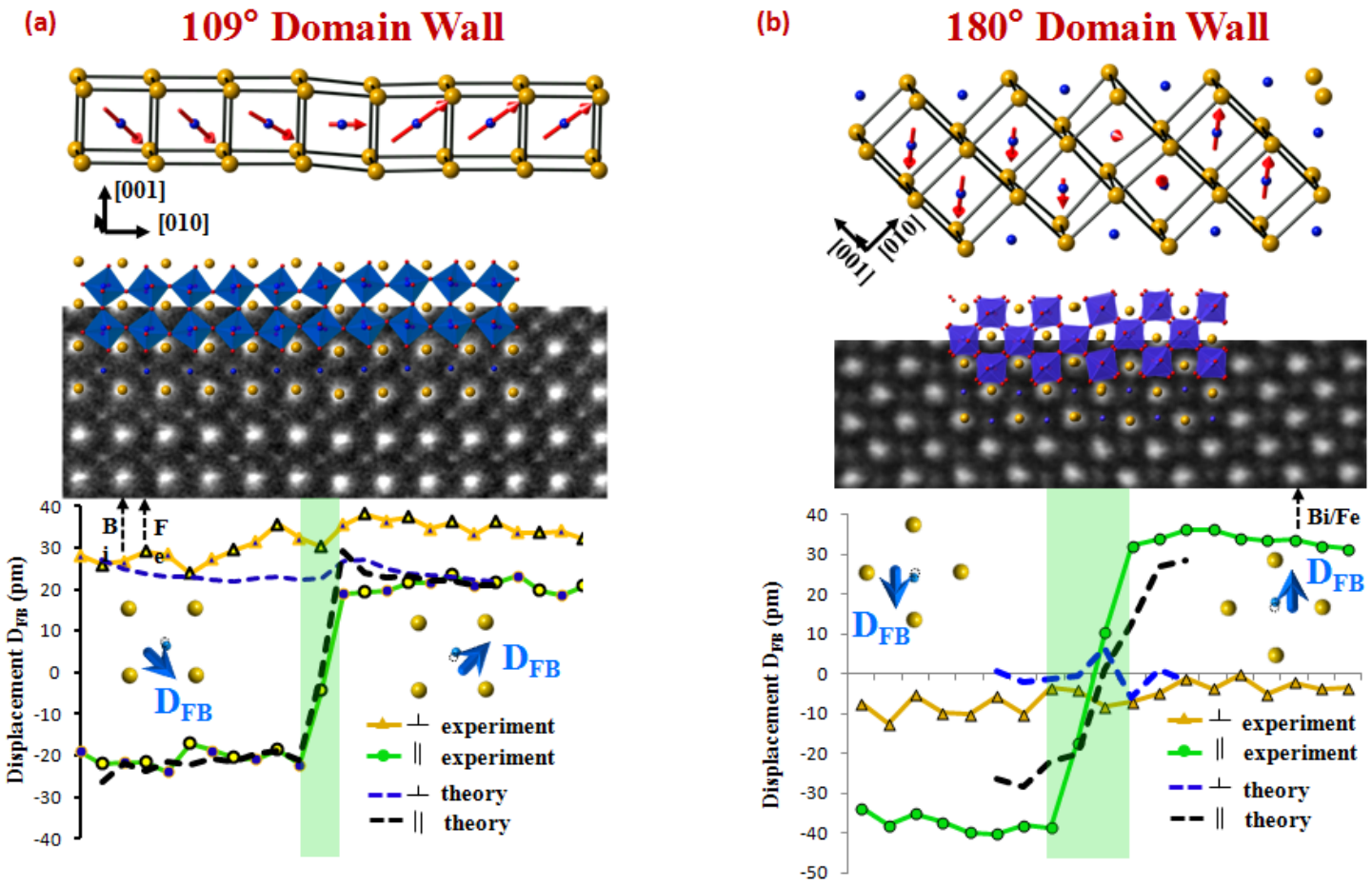

Fig. 3.7 Atomic Structure of 109° and 180° Domain Walls
(a) The domain structure of a 109° domain wall. The two orthogonal components of the average cation displacement (solid lines: parallel to and normal to the domain wall plane) of each column is plotted below the HAADF image. The fit to a first principles theoretical domain wall structure is very good (dashed lines). **(b)** The domain structure of a 180° domain wall and the average cation displacement (parallel to and normal to the domain wall plane) of each column. Fit to first principles is not as good suggesting too short of a supercell.

The 71° domain wall provides a difficult challenge to analyze microscopically. In order to view their {101} planes edge-on they must also be viewed along the [010] beam direction. Unfortunately, the change in polarization is also along [010] so it is invisible in the TEM image. The only possibilities are then to either view it edge-on from the top surface along $[10\bar{1}]$, use a non edge-on zone axis, or look at a different type of 71° domain wall. The first option is virtually impossible by conventional mechanical polishing. The latter option is best and as I will show, still far from ideal. It also requires a 71° domain wall which is not one of those formed by the substrate strain and thus has no driving force to exist in the film. However, we are able to create 71° domain walls through the application of an electric field, which is the subject of chapter 5. An example of such a 71° domain wall formed by in-situ switching of a 100 nm $BiFeO_3$ film is shown in Fig. 3.8a. In this case the polarization change is along the film normal (vertical direction in the figure). Unfortunately it does not strictly adhere to any well defined plane and the same is quite likely to be true along the electron beam direction as well. The equilibrium plane for this type of 71° domain wall is the vertical (110) plane. Given that this is viewed along the [100] axis the plane at equilibrium is tilted by 45° degrees. The irregular domain wall prevents averaging across multiple columns as was done for the 109° and 180° domain wall and has a great deal of local variation which is especially apparent in the magnitude. The polarization profile along a single atomic column, labeled by a white stripe in Fig. 3.8a is graphed in polar coordinates in Fig. 3.8b. Over the course of ~6 atomic layers there is a ~90° rotation of the projected polarization. The magnitude is in a trough for ~9 atomic layers at the domain wall. This result is considerably wider than either of the other two domain walls, however it is likely to be partly an artifact from not being viewed edge-on. However, it does provide an upper bound for the 71° domain wall width.

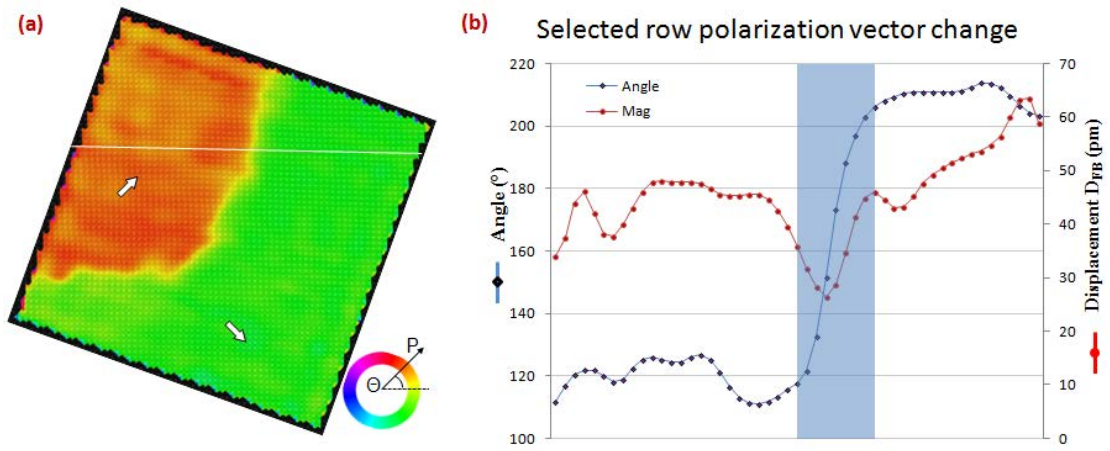

Fig. 3.8 Atomic Structure of a 71° Domain Wall
(a) Polarization mapping of a 71° domain wall formed by in-situ switching by an applied electric field. The polarization along the white line is shown in **(b)**. The angle and magnitude of the polarization change over ~6 and

3.5 The Structure of the Heterointerface of $BiFeO_3$ and $TbScO_3$

The orthoscandates, {RE}ScO_3, such as the $TbScO_3$ and $DyScO_3$ used in this work are popular single crystal substrates due to the tunability of the in-plane lattice parameter from 3.95 Å to 4.05 Å depending on the choice of rare-earth {RE} element[133]. This allows for many of the ferroelectric perovskites to be grown on closely lattice matched substrates such as $BiFeO_3/TbScO_3$ and $PbZr_{0.2}Ti_{0.8}O_3/DyScO_3$ to avoid strain effects and misfit dislocation formation. The orthoscandates have a low-symmetry orthorhombic Pnma structure based on a distorted cubic perovskite cell. This results in a slight anisotropy of the in-plane lattice parameter, a_1 = 3.957Å and a_2 = 3.953 Å for $TbScO_3$[123]. $BiFeO_3$ grown on the $(110)_O$ $TbScO_3$ surface preferentially forms the r_1 and r_4 ferroelastic variants[106] and strain anisotropy was originally posited as a possible cause. However the anisotropy is extremely small and the addition of thin epitaxial cubic buffer layers returns the degeneracy of the r_1 and r_2 variants despite the fact that the in-plane lattice constant is unchanged. This strongly points to some other cause, most likely in the crystal structure of the $BiFeO_3/TbScO_3$ interface, which is responsible.

A high resolution HAADF STEM image of the $BiFeO_3$ interface with $TbScO_3$ is shown in Fig. 3.9a. In the Z-contrast image the $BiFeO_3$ appears brighter since Bi (Z=83) and Fe (Z=26) are heavier than Tb (Z=65) and Sc (Z=21) respectively. The pixel intensity

averaged across the image is shown at right with a clear abrupt transition from the darker $TbScO_3$ to brighter $BiFeO_3$ layer. Polarization mapping was performed using the cation displacement and an overlaid vector image is shown in Fig. 3.9b. The result is a clear non-polar region, or at least a region of suppressed Bi-displacement, extending four units cells beyond the Z-contrast determined interface. A close look at the crystal structure in this region shows that it still possess some of the large A-site distortions of the $TbScO_3$ structure. For example, the A to A bond length deviation and A to A bond angles are shown in Fig. 3.9c and Fig. 3.9d respectively. They show that the oscillating A-site position of $TbScO_3$ propagates the same distance in to the $BiFeO_3$ layer as the non-polar region. This suggests that the structural distortion induced by the low-symmetry substrate results in a small "dead layer" at the ferroelectric interface, a feature which is often reported from macroscale electrical measurements.

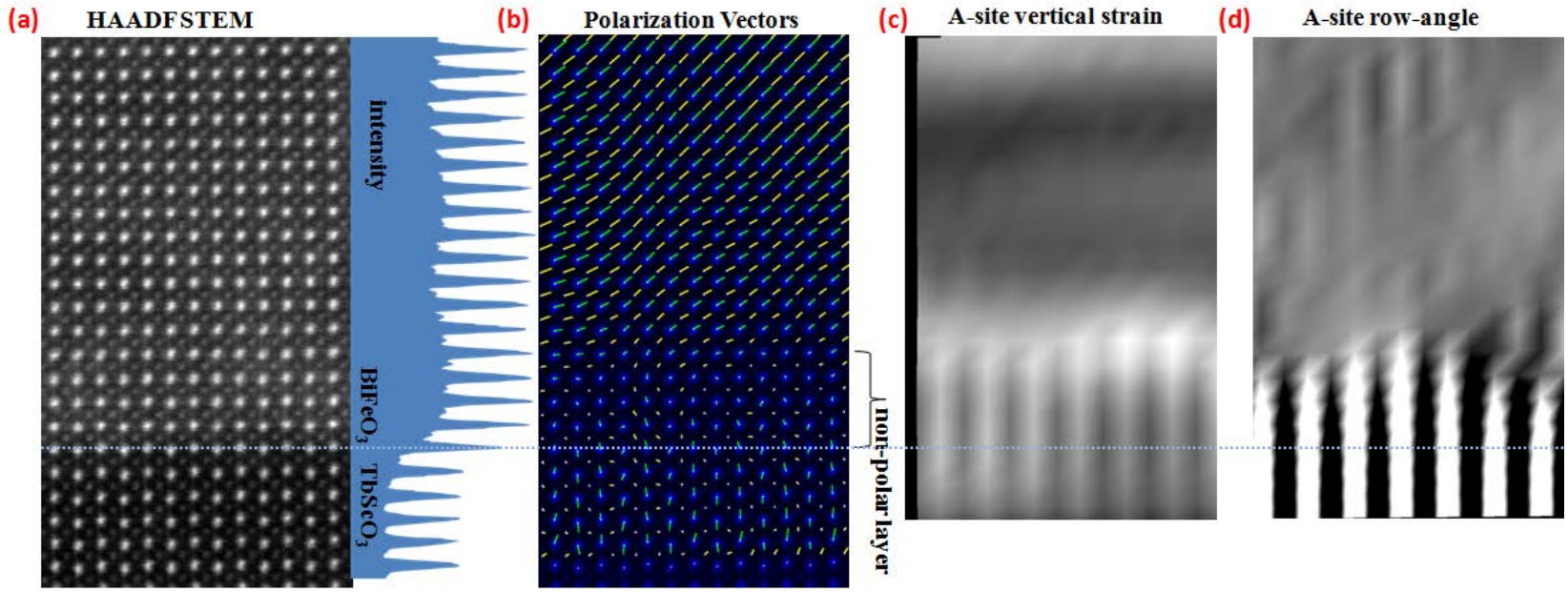

Fig. 3.9 $BiFeO_3$ / $TbScO_3$ Interface
(a) HAADF STEM image of the $BiFeO_3$ (top) / $TbScO_3$ (bottom) interface. The averaged pixel intensity shows the boundary between the heavier $BiFeO_3$ atoms and lighter $TbScO_3$ (marked by dashed line). **(b)** Polarization mapping shows a non-polar region of $BiFeO_3$ ~4 unit cells thick. **(c)** A to A bond length variation and **(d)** A to A horizontal bond angle show the propagation of the low symmetry $TbScO_3$ structure into this nonpolar layer.

An alternate possibility to structural distortion as the source of this layer is interdiffusion of elements which suppresses the ferroelectric phase near the interface. This was measured experimentally using EDS mapping by a FEI chemi-STEM system which uses an extremely large solid angle detector to minimize acquisition time. The quantitative elemental maps at the interface are shown in Fig. 3.10 for all 5 constituent components. Even the position of oxygen is visible, despite the low x-ray conversion efficiency for such light elements. The results show that the interface is quite sharp, the A-site atoms have only a single layer of intermixing. The smaller and lighter B-site atoms show more interdiffusion with approximately three layers of intermixing. This is dominated by Sc which extends 2-3 layers into $BiFeO_3$. Given that the ferroelectric distortion is primarily A-site rather than B-site driven in $BiFeO_3$, the chemical analysis suggests that the polar phase should appear within one unit cell of the interface. This further supports the structural distortion as the source of the non-polar region.

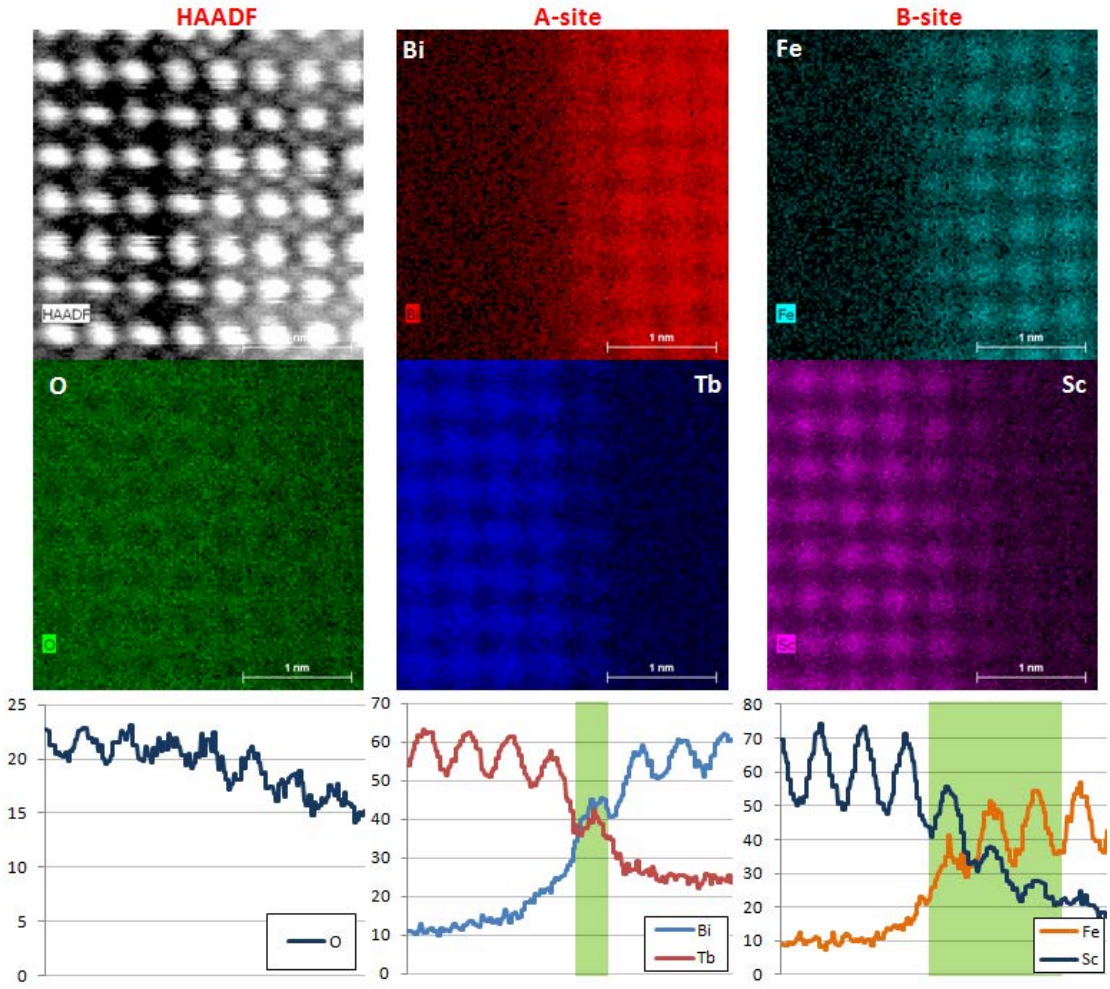

Fig. 3.10 EDS Chemical Composition Across the $BiFeO_3$ / $TbScO_3$ Interface
A HAADF STEM image (top left) and EDS elemental maps for the five constituent elements at the $BiFeO_3$/$TbScO_3$ interface. The A-site atoms (Bi,Tb) intermix only in a single layer. The B-site atoms (Fe,Sc) intermix over approximately 3 layers.

An additional factor to consider in the polarization distribution at the surface is the depolarizing fields generated by the bound charge, especially with an insulating material such as $TbScO_3$. To determine this contribution the structure of the $BiFeO_3$ interface with $TbScO_3$ was compared to a sample buffered with a conducting $La_{0.7}Sr_{0.3}MnO_3$ layer. A comparison of the two systems is shown in Fig. 3.11. The interface was determined from the Z-contrast intensity as the onset of the intensity increase of the higher Z $BiFeO_3$ film. The polarization across both interfaces are graphed at the bottom in polar magnitude/angle form. The oscillations in the $TbScO_3$ structure are very pronounced in

this graph and are slowly damped within the first few unit cells of the interface with $BiFeO_3$ after which the polarization takes on a nearly fixed direction and the magnitude increases to a plateau. The same general trend is also observed for $La_{0.7}Sr_{0.3}MnO_3$ except the oscillations in the angle are measuring noise since the displacements are ~0. Here the magnitude is distinctly bimodal with plateaus corresponding to the non-polar $La_{0.7}Sr_{0.3}MnO_3$ layer and the polar $BiFeO_3$ layer. The transition region is measured to be ~3.5 unit cells (highlighted in green). This transition region is harder to distinguish in the $TbScO_3$ due to the oscillating Tb cations. From the interface determined in the Z-contrast image the transition region within $BiFeO_3$ is ~6 unit cells (also highlighted in green). It is clear there is also damping of the distorted $TbScO_3$ structure within the $TbScO_3$ side of the interface so that the total transition region closer to 9 unit cells, however I will restrict the discussion to the effect on the $BiFeO_3$ film. This comparison suggests that the $La_{0.7}Sr_{0.3}MnO_3$ layer allows for a higher polarization gradient due to the free carriers to screen the surface charge. However, this contribution may be exaggerated since a comparison of the actual slope of the increasing polarization between the two systems does not show a very significant difference. Rather it appears that the difference is primarily an offset of the onset of polarization from the interface, and that this offset distance corresponds closely to the layers of $BiFeO_3$ distorted by the $TbScO_3$ symmetry.

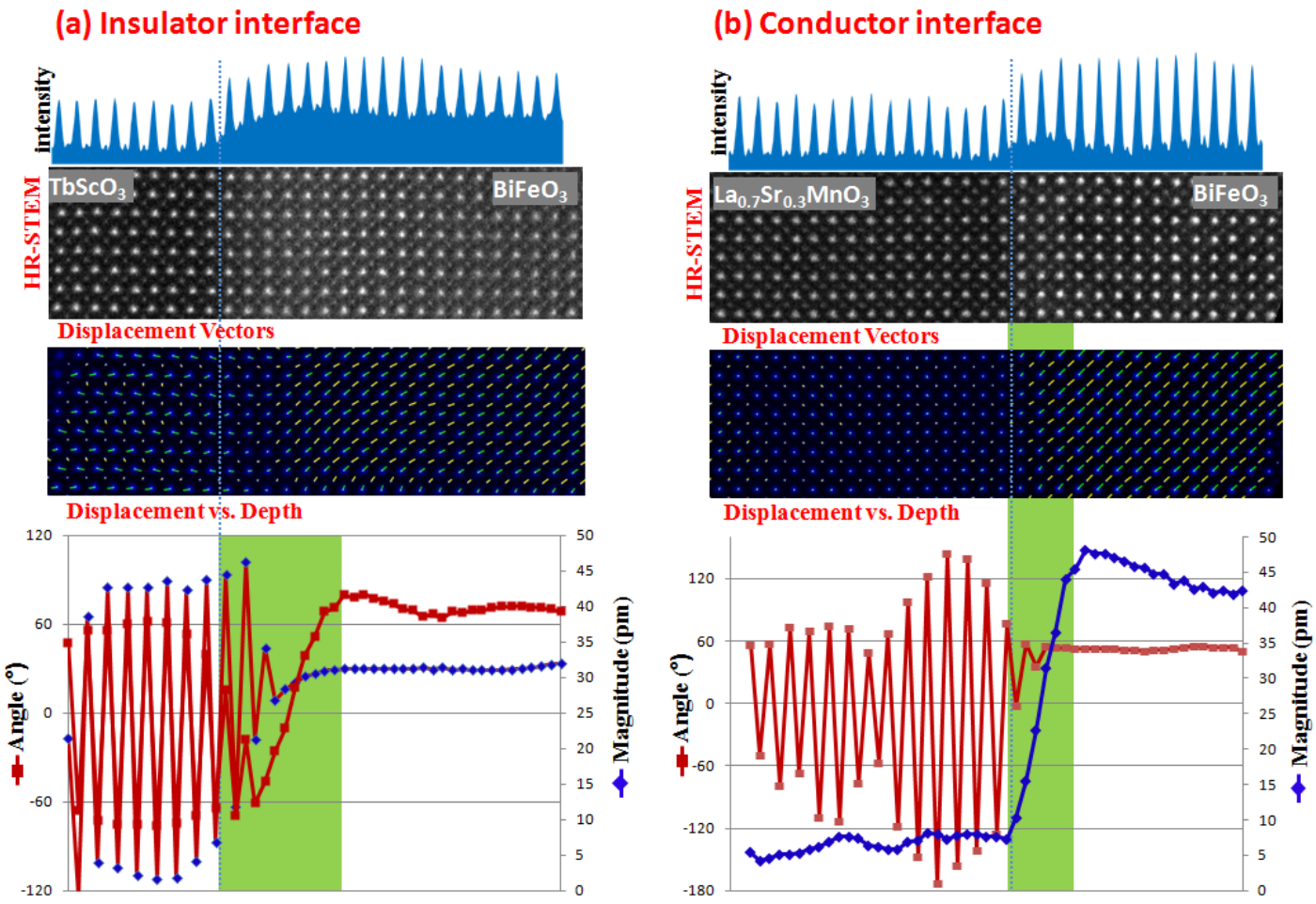

Fig. 3.11 $BiFeO_3$ Interface and Compensation
A comparison of the polarization and structure aross the **(a)** $BiFeO_3$ / $TbScO_3$ and **(b)** $BiFeO_3$ / $La_{0.7}Sr_{0.3}MnO_3$ interfaces. Each structure shows the HAADF STEM image and corresponding intensity, with the interface demarked by a dashed line. The polarization in magnitude/angle coordinates corresponding to the polarization maps are graphed at bottom. The distance for $BiFeO_3$ to reach its peak polarization from the interface line is ~6 unit cells for $TbScO_3$ and ~3.5 unit cells for $La_{0.7}Sr_{0.3}MnO_3$

The last point to address is the source of the broken degeneracy of the four ferroelastic variants. One explanation for the dominance of the r_1 and r_4 variants is from consideration of the out-of-plane symmetry of the two structures. Both $TbScO_3$ and $BiFeO_3$ exhibit a tilting of their (*h*00) planes, as illustrated by the electron diffraction image and corresponding diagram in Fig. 3.12. For $TbScO_3$ this direction is fixed and much larger than in $BiFeO_3$. In $BiFeO_3$ the direction of the tilt varies depending on the ferroelastic variant. The two low-energy variants are the ones that share the same (*h*00) tilt direction as the $TbScO_3$ substrate. This small difference may break the degeneracy by changing the out-of-plane O-Fe-O bond angles or from longer range interactions across the interface. This would explain why the addition of a cubic buffer layer, despite maintaining the in-plane strain, would return the 4-variant degeneracy. First-principles calculations are probably required to determine which of these two explanations, if either, is the primary cause of the preferential orientations.

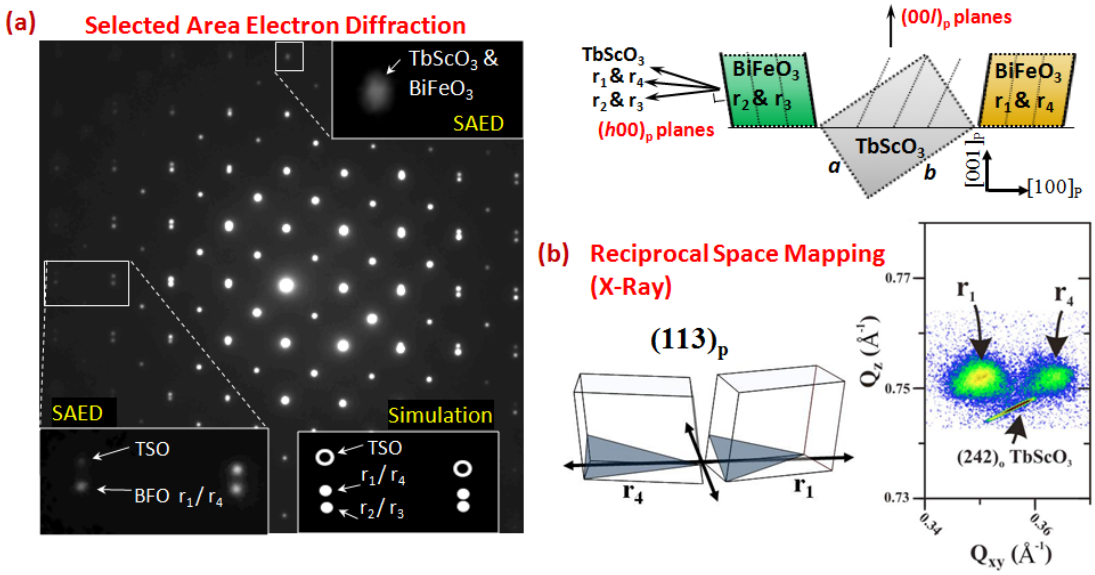

Fig. 3.12 Determination of Ferroelastic Variants
(a) Selected area electron diffraction pattern from the $BiFeO_3/TbScO_3$ interface with the beam along $[010]_P$. The single $(00l)_P$ peaks shows the alignment of the $(00l)_P$ planes and close match of the d-spacing. The split of the $(h00)_P$ spots shows the rotations of the $(h00)_P$ planes corresponding to $TbScO_3$ and $BiFeO_3$ r_1 and/or r_4 ferroelastic variants but no peaks for r_2 or r_3 variants. A simulated SAED pattern shows the expected pattern if r_2/r_3 variants were present. **(b)** X-Ray reciprocal space mapping of the $(113)_P$ peak shows only the r_1 and r_4 variants are present in the film.

3.6 Electrostatic Boundary Conditions

The electrical properties of the materials at the ferroelectric surface strongly influence the ferroelectric film based on their ability or inability to compensate the bound surface charge. The most typical approach to screen the surface charge is the addition of electrodes to the surface such as noble metals like platinum and gold or conducting oxides such as $SrRuO_3$ or $La_{0.7}Sr_{0.3}MnO_3$. Significant compensation can also be provided by the adsorption of mobile ions including those from exposure to atmosphere[134,135] and this molecular screening may in fact be more effective than the free carriers in electrodes[136]. Unfortunately both these extrinsic forms of compensation are unable to completely screen the bound charge. The finite separation between the bound surface charge and screening charges results in a dipole layer. The depolarizing field that results from this dipole layer in a thin ferroelectric film with symmetric charge screening electrodes can be expressed as[73]:

$$E_D = -\frac{P}{d \cdot \varepsilon_F} \cdot \left(\frac{2 \cdot \varepsilon_F}{2 \cdot \varepsilon_F / d + \varepsilon_0 / d_s} \right) \quad 3\text{-}5$$

Where P is the polarization normal to the surface, d is the thickness, ε_F is the dielectric constant of the ferroelectric film, ε_0 is the permittivity of free space, and d_s is the screening length of the electrode. The latter term can be replaced by an effective screening length λ_{eff} to give a more general expression[137]:

$$E_D = -\frac{\lambda_{eff} \cdot P}{d \cdot \varepsilon_F} \quad 3\text{-}6$$

The result is a depolarizing field which is monotonically increasing with the inverse of the film thickness. For compensated surfaces at large length scales the ratio of the screening length λ_{eff} to the film thickness d is miniscule and depolarizing effects are absent. However, in extremely thin films (d~<10nm) the depolarizing fields can become large enough to suppress the polar state. One byproduct is a longstanding question in ferroelectric films of the critical thickness (or thinness) before the ferroelectric state is lost. Recent first principles calculations[76,138] and experiments[78] suggest it can be as little

as 3 unit cells, however this is dependent on how efficiently the interface screens the surface charge ($\lambda_{eff} \rightarrow 0$).

The efficiency of charge screening is not easy to determine directly by experiment. This is especially true for free surfaces where the structure is likely to interact with whichever types and densities of mobile ions are available to adsorb to the surface. All of these parameters of a given real-life experiment are generally unknown. Even heterointerfaces between structurally matched materials can have unique properties including a radical difference in conductivity[11,12]. Thus, growing a film on an ostensibly insulating material does not guarantee an insulating interface. However, ferroelectric films also have intrinsic means of charge compensation via the formation of domain structures with alternating surface charge. In contrast to screening charges, these domain structures are relatively easy to detect, especially by TEM. The remainder of this chapter and the following chapter will use the domain structure to determine the local electrostatic boundary conditions.

The simplest means of determining the boundary conditions of a $BiFeO_3$ film is from the two possible twin structures: 71° and 109° stripes (Fig. 3.13a-b). From Landau theory (section 2.4) the domain wall energy scales with the gradient of the polarization making the 109° domain walls twice the energy density of the 71°s. However, from first principles calculations 71° and 109° domain walls have domain wall energy densities of 363 and 205 mJm^{-2} respectively where the lower energy of the 109°s is because they are better able to preserve the canting of the oxygen octahedra[44]. Regardless, there is not a large disparity in the self energy between the two domain wall types. The dominance of one type over the other primarily depends on the minimization of the electrostatic energy[132]. The 71° domain pattern has a single out-of-plane polarization vector resulting in a uniform sheet of bound charge (Fig. 3.13c). If the ferroelectric surfaces are uncompensated by free charges, then the bound charges would produce a large uniform depolarization field. Instead, when such uncompensated conditions are present, the system favors the alternating out-of-plane polarization of the 109° domain pattern which has a net surface charge of zero (Fig. 3.13d). Thus, a transition between these two twin structures is indicative of the boundary conditions. This was elegantly demonstrated by

Chu et. al. who showed a gradual transition to the 109° structure as films were grown on progressively thinner, and thus less conductive, oxide electrodes[132].

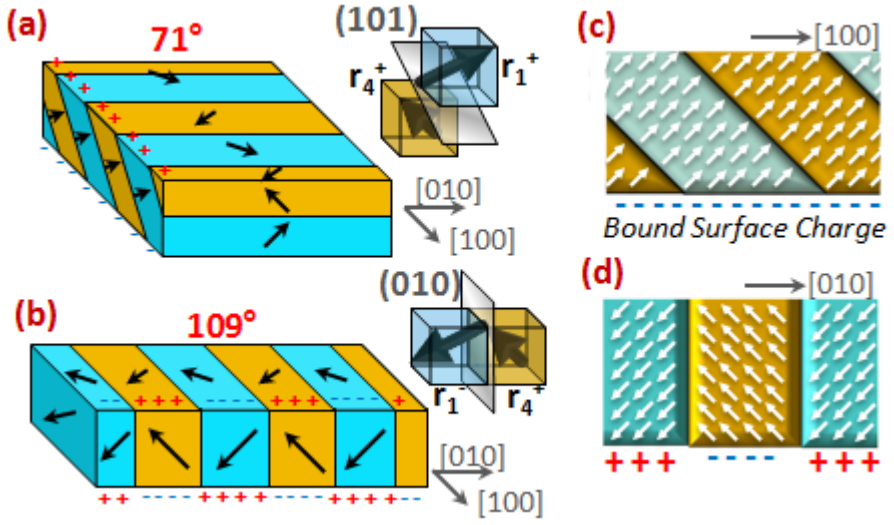

Fig. 3.13 Depolarizing Fields from 71° and 109° Twins
(a) Twins of these two variants will form domain patterns with 71° rotation of the polarization across $(101)_P$ walls **(b)** or 109° rotation of the polarization across $(010)_P$ domain walls **(c)**. If uncompensated, these patterns produce the bound surface charges shown in **(d)** and **(e)**. The surface charge distributions of the 109° pattern produce local electric fields at the surface.

The domain structure of the 20 nm thick $BiFeO_3$ film grown directly on $(110)_O$ $TbScO_3$ is shown in planar view (Fig. 3.14a) and in cross-section (Fig. 3.14b) TEM images. The corresponding domain configuration is shown below the cross section image, determined by polarization mapping. The self compensating 109° twin structure indicates a strong depolarizing field and that one or both interfaces are poorly screened. The addition of a 20 nm epitaxial $La_{0.7}Sr_{0.3}MnO_3$ bottom electrode (Fig. 3.14c) causes this structure to disappear. Instead the $BiFeO_3$ film forms large domains several hundred nanometers in width with little discernable long-range pattern at this length scale separated by domain boundaries typically of paired 109° and 180° domain walls such as the region shown in Fig. 3.14c. These results show that the $TbScO_3$ interface is highly insulating which is in good agreement with the strong insulating properties of bulk $TbScO_3$. Furthermore, the presence of such large monodomain regions also suggests that the top surface must be at least partially compensated as well (this is corroborated in section 4.3).

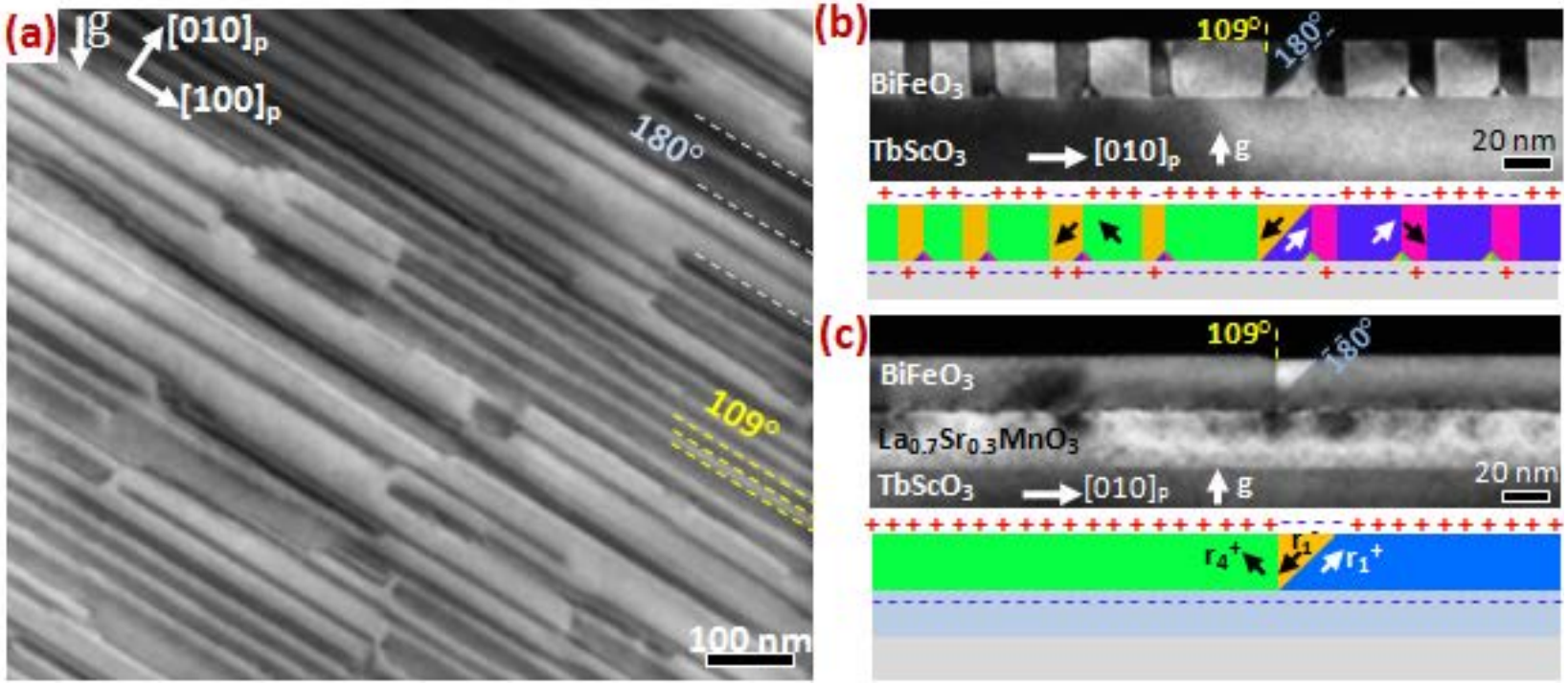

Fig. 3.14 Effect of Screening Charges on Domain Structure
$BiFeO_3$ on insulating $TbScO_3$ forms a $r_1 \| r_4$ striped domain pattern separated by vertical $(010)_P$ 109° domain walls as seen in planar view **(a)** and cross sectional **(b)** dark field TEM. **(c)** The addition of a conductive 20 nm buffer layer of $La_{0.7}Sr_{0.3}MnO_3$ results in very large domains separated by vertical 109° paired with inclined 180° domain walls.

If there is either full or partial screening of the charge at the top surface of the $BiFeO_3$ film then equation 3-6 predicts the film will exhibit a thickness dependent depolarization field which should manifest as a thickness dependent domain pattern. A thickness series of $BiFeO_3$ films on the bare $TbScO_3$ with thicknesses of 45 nm, 90 nm, 180 nm and 385 nm were grown in immediate succession to maintain constant growth conditions. As the film thickness increases the domain structure transitions from the self-compensating 109° twin structure in the thin 45 nm film (Fig. 3.15a,b), to a mixed 109° and 71° case in the 90 nm film (Fig. 3.15c,d), and finally results in a pure 71° domain structure for the 180 and 385 nm films (Fig. 3.15e,f). Fig. 3.15 shows the cross sectional and planar view images of the domain structure. The planar view images all have identical sample orientations where 109° domain walls appear vertical in the image and 71° domain walls are horizontal. The planar view data of the thicker films are taken from PFM scans. The PFM images of the thickest 385 nm case show a clear striped contrast of the in-plane (IP) polarization (Fig. 3.15f) but a single polarization normal to the film (OOP). The 90 nm film represents a mixed case where 109° and 71° domain walls create a cross hatched pattern. A planar view diffraction contrast TEM image is used to show the domain structure of the 45 nm film because it is too thin to measure the piezoresponse.

The observed change in domain structure is consistent with an increase in the depolarizing field expected from equation 3-6 which favors a 109° structure in very thin films. However, first principle calculations predict the energy density of the 71° domain walls to be 75% larger than 109° domain walls[44]. Furthermore the 71° domain walls are inclined 45% on the [101] planes so they have ~40% more surface area. One must then question why the 71° domain structure appears at all – it has a higher energy and produces a strong depolarizing field. Provided that the first principles calculations are correct, it indicates a preferential poling direction. This can arise from asymmetric screening efficiencies at the interfaces such as a polar surface layer of the $TbScO_3$ substrate or preferential adsorption of only positive or negative ions at the top surface. It can also arise from gradients in dopants and/or strain and from electronic band bending

such as from the formation of a Schottky junction. Regardless, this series shows that the preferred poling direction which favors the uniform z-axis polarization of the 71° domain structure is overcome by depolarizing effects at small thicknesses.

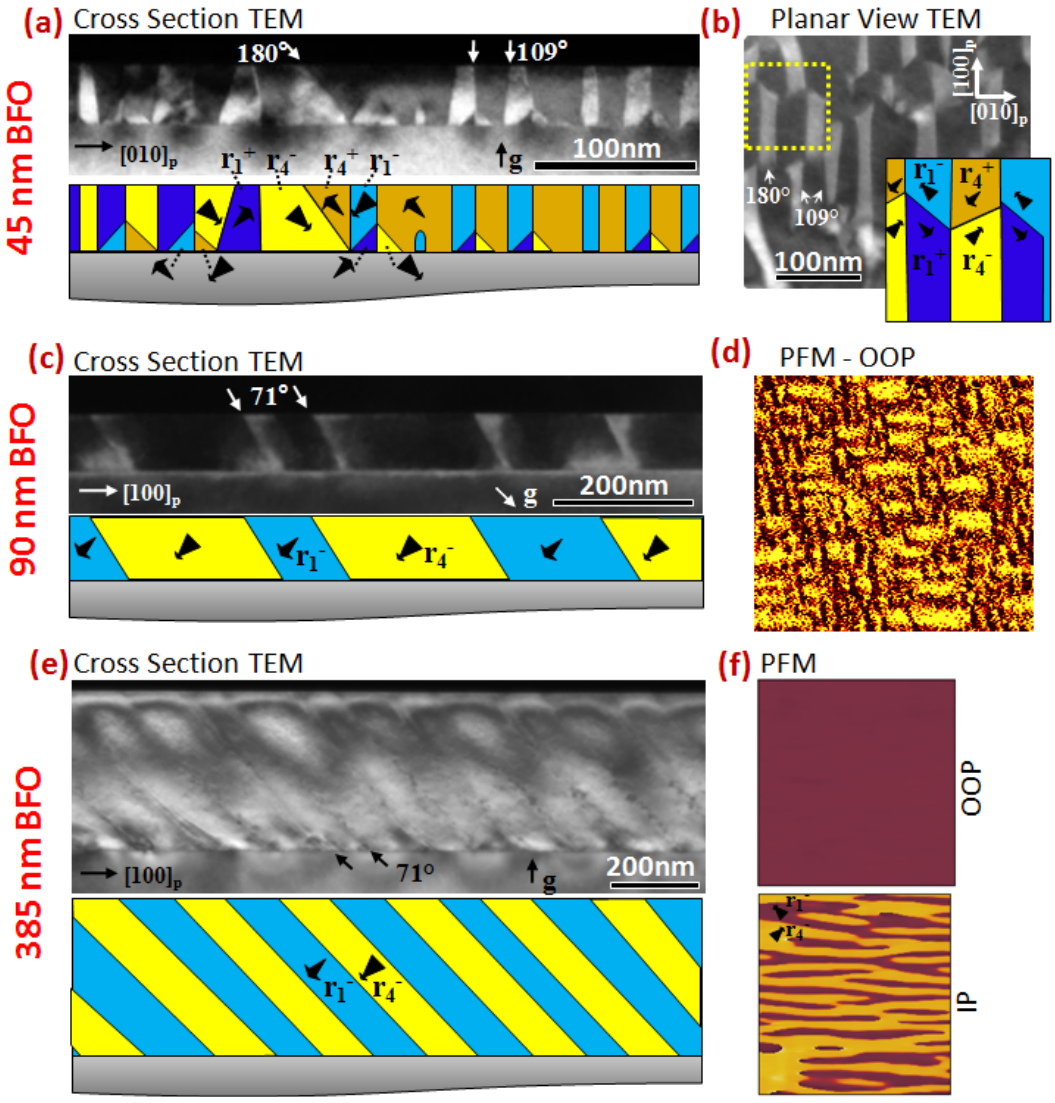

Fig. 3.15 Thickness Dependance on Domain Structure
The domain structure for three thickness of $BiFeO_3$ films on insulating $TbScO_3$ substrates. The 45 nm film forms a stripe pattern of vertical (010) 109° domain walls as seen in cross section **(a)** and planar view **(b)** dark field TEM images. The 90 nm film forms a mixed domain structure or 109° and 71° domain walls, the latter highlighted by cross sectional TEM **(c)**. The out-of-plane (OOP) PFM image of this film **(d)** shows the cross hatched mixed structure. The 71° domain pattern of the thickest film, 385 nm, is shown in cross sectional TEM **(e)** and planar view PFM **(f)**. The PFM image shows both the in-plane (IP) and out-of-plane domain structure.

Chapter 4

4 Polarization Vortices at Insulating Interfaces

4.1 Background

In ferroic materials, the magnetization or polarization may adopt rotational patterns to reduce the energy of magnetic or electric fields. Such flux closure or vortex domains are well known to ferromagnetic materials[139] but have only recently been observed in ferroelectric nanostructures[140,141] where they have garnered particular interest for storing memory bits in the vortex state with very little cross-talk between neighboring bits[142]. Polarization vortex structures have also been seen in ferroelectric thin films[143,144], however they are typically unstable and usually induced by reduced dimensionality. This rarity of observed flux closure states in ferroelectrics compared to ferromagnetic materials has several causes. First, unlike magnets there is an abundance of electrical monopoles which tend to extrinsically screen fringing fields which reduces or negates the energetic driving force. Second, as discussed in section 3.4, strong electrostriction restricts the polarization to fixed easy directions. Additionally such a rotation will likely pass through another polarization axis which is a ferroelastic transition in most systems and so would also add strain. Thus, the energy cost of gradual polarization rotations is large. Ultimately, the most important reason is that ferroelectric domain walls are several orders of magnitude smaller than in ferromagnets so the observation of flux closure required an atomic-scale view of the polarization distribution.

Using the polarization mapping developed in section 3.3, this chapter details the discovery of nanoscale polarization vortices at the interface of a ferroelectric and insulating material (published in ref 145). The lack of compensation at an insulating interface is analogous to unavailability of screening for ferromagnetic materials and is the driving force for the creation of flux closure domains. The strong insulating properties of the $BiFeO_3$ / $(110)_O$ $TbScO_3$ interface was already established in section 3.6, and

therefore this material system was also used for this study. Experimental data is combined with Phase-Field modeling to determine the energetic contributions driving the formation of the vortex domain structures. The results show that they compensate in-plane depolarizing fields produced from alternating surface charges in typical twinning structures of rhombohedral $BiFeO_3$. Although these vortices are observed in a thin film they are not connected with the reduced dimensionality of this system. Following this report of $BiFeO_3$ flux closure domains similar phenomenon was reported for $PbZr_{0.2}Ti_{0.8}O_3$ on insulating $SrTiO_3$ surfaces[127] which supports this as a universal phenomenon.

4.2 Experimental

A 20 nm $BiFeO_3$ film grown on single crystal $(110)_O$ $TbScO_3$ by MBE was used in this work[*] (growth details in section 2.3). Experimental determination of the spatial distribution of the polarization was determined by the polarization mapping method detailed in section 3.3. All TEM images are from HAADF STEM mode taken on the FEI titan TEAM 0.5 at the National Center for Electron Microscopy (NCEM) at the Lawrence Berkeley National Lab operating at 300 kV. The formulations for the energetic contributions and the phase field simulation methodology[‡] are detailed in section 2.4.

4.3 Domain Vortices

The 20 nm $BiFeO_3$ film formed a 109° striped mesoscale domain structure described previously in Fig. 3.1a,b. Using HRSTEM HAADF images we mapped the spatial distribution of the $\mathbf{D_{FB}}$ vector in the near surface region of the $BiFeO_3/TbScO_3$ interface to determine the polarization distribution. A *Z*-contrast image of two adjacent 109° domain walls is shown in Fig. 4.1a color mapped according to the B-site $\mathbf{D_{FB}}$ vector (yellow arrows). The pair represents the two types of 109° domain wall terminations at the $BiFeO_3/TbScO_3$ substrate: directly terminating (Fig. 4.1a−left and Fig. 4.1b) and those forming a triangular pattern of domain walls (Fig. 4.1a−right and Fig. 4.1c). The triangle domains consist of a mirrored pair of inclined 180° domain walls, which form a vortex domain structure with the polarization rotating about the intersection of two 109°

[*] Provided by collaboration with Dr. Darrell Schlom – *Cornell University*
[‡] Provided by collaboration with Dr. Long-Qing Chen – *Penn State*

and two 180° domain walls. The polarization closure is clear in the vector plot of $\mathbf{D_{FB}}$ in Fig. 4.1c. No such polarization closure is observed in the $\mathbf{D_{FB}}$ vectors at the direct domain wall termination in Fig. 4.1b. The map in Fig. 4.1 is an interpolation of only the B-site (Fe, Sc) cation displacements whereas the color maps in Fig. 4.1b,c are interpolated from both the A (Bi, Tb) and B (Fe, Sc) sites. The latter shows the oscillation of the Tb peaks within the $TbScO_3$ structure which is the source of the stripe pattern in the substrate region of the polarization maps.

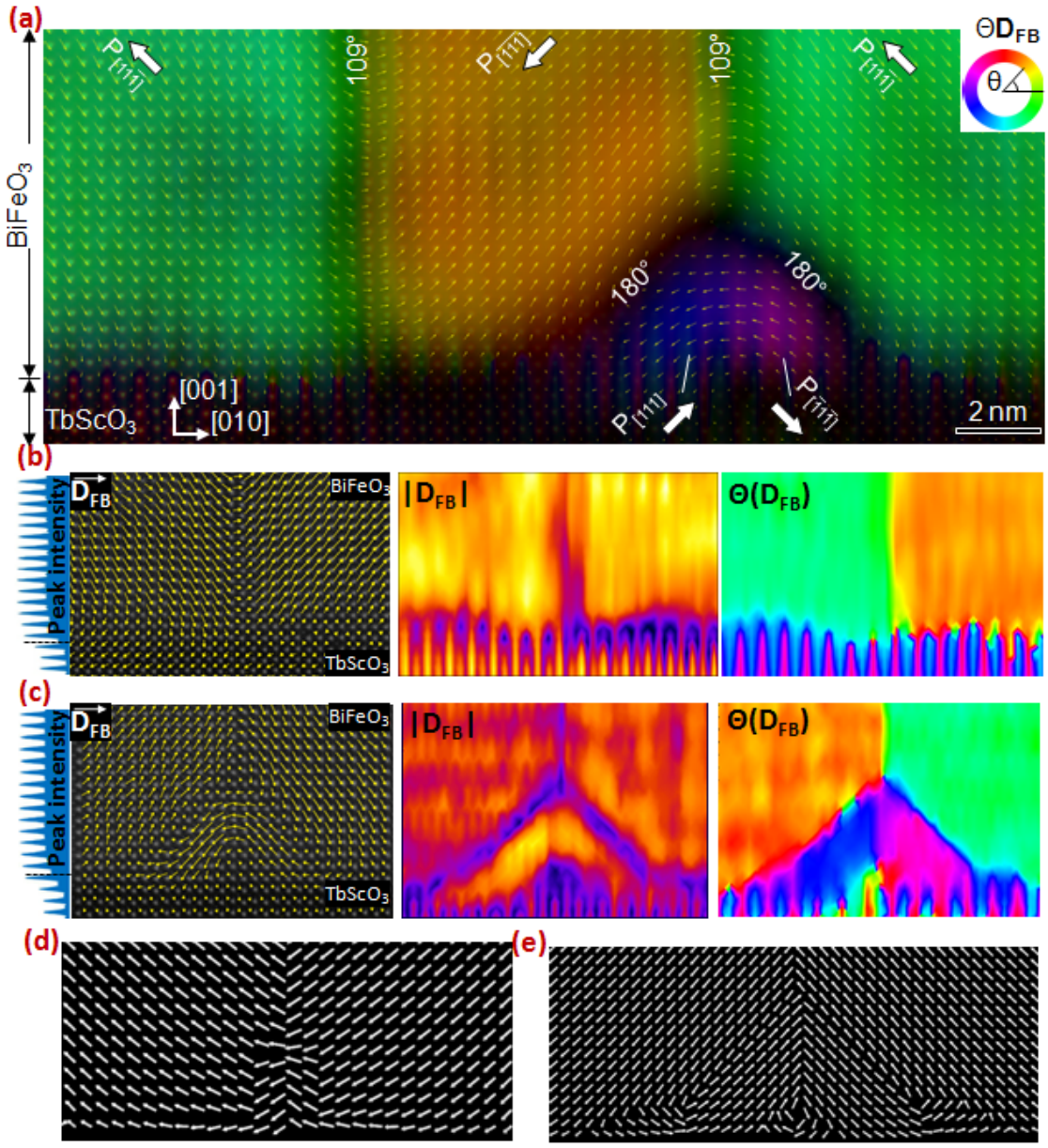

Fig. 4.1 Vortex Domains
(a) Polarization map from a HAADF STEM image containing the intersection of two 109° domain walls with the $TbScO_3$ surface. The $\mathbf{D_{FB}}$ vectors at the B-sites are shown as yellow arrows and determine the fill color according to the legend at right. **(b)** A $\mathbf{D_{FB}}$ vector plot of the vectors for the 109° domain wall which terminates directly with the interface plus the corresponding color maps of the magnitude and angle of $\mathbf{D_{FB}}$ shown at right. **(c)** A $\mathbf{D_{FB}}$ vector plot of the vectors for a 109° domain wall which forms a vortex domain with associated color maps of the magnitude and angle of $\mathbf{D_{FB}}$. Unlike (a), both **b**, and **c**, include displacements of the A-site which shows the oscillation of the Tb site in the $TbScO_3$ layer giving the striped appearance. The polarization distribution of a directly terminating 109° domain wall **(e)** and a triangle domain terminating 109° domain wall **(f)** from a phase field simulation.

The two triangle domains in the vortex structure exhibit several intriguing properties. Unlike the narrow domain walls at the film interior, the 180° and 109° domain walls at the vortices have gradual rotations of the polarization vector exhibiting a mixed Néel-

Ising character, especially where the 180° domain walls intersect the $TbScO_3$ surface. This leads to the formation of even smaller closure domains at the base of the triangles. The displacement vector extends into the first layer of the substrate suggesting that a polarization may be induced on the $TbScO_3$ surface. Lastly, the in-plane [010] component of $\mathbf{D_{FB}}$ within the triangle domains is much larger than its value in the interior of the neighboring domains, as can be seen from both the vector and corresponding magnitude plots (Fig. 4.1c). From a quantitative analysis of $\mathbf{D_{FB}}$ (Fig. 4.2), the [001] components inside and outside the triangle domains are roughly identical, but the [010] components within the triangle 109° domain wall are in some places more than double the value within the interior of the neighboring domains. Since the component along the viewing direction is unknown, a rotation of the polarization along the [001] axis cannot be ruled out, but it alone would be insufficient to account for the observed increase. The increased in-plane polarization may also modify or create functional properties in the domain wall since they deviate from the equilibrium structure analyzed in section 3.4.

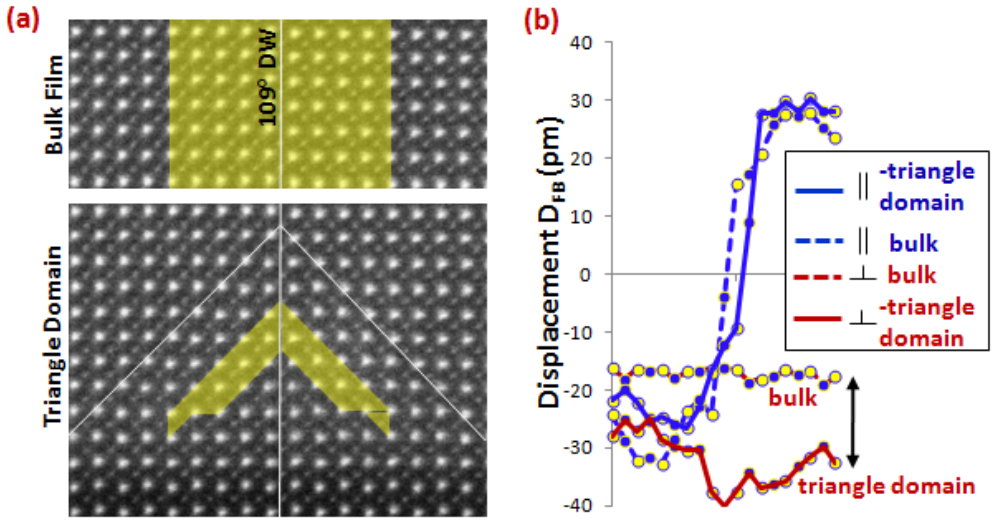

Fig. 4.2 Polarization Profiles Across Domain Walls
(a) HRSTEM HAADF images of the 109° domain wall in the bulk film and at the vortex site. **(b)**. The corresponding cation displacements $\mathbf{D_{FB}}$ normal and parallel to a 109° domain wall for the bulk film and inside the triangle domain averaged over the regions highlighted. The parallel components are similar in both cases but there is a significant increase in the normal component within the triangle domain indicating an enhancement of polarization.

The energetic driving force for the formation/stability of the vortex domains is analyzed with phase-field simulations[‡] by comparing the spatial variation of the electrostatic energy and the elastic energy densities for a periodic 109° domain wall array assuming unscreened charges (open-circuit boundary conditions) at the $BiFeO_3$ surfaces (Fig. 5a). There is no distinction in elastic energy, but a significant difference in electrostatic energy, between the terminations of adjacent 109° domain walls with the substrate. The bound charge distribution (ρ_b) corresponding to this structure (Fig. 4.3b) gives rise to the depolarizing electric field **E,** shown in Fig. 4.3c (black arrows) overlaid with the electrostatic energy. The high electrostatic energy termination (labeled Type II) results from the depolarizing field **E** opposing the polarization vector **P**. In contrast, **E** in the low energy domain wall (labeled type I) is more closely parallel to **P**, corresponding to a relatively small electrostatic energy.

[‡] Provided by collaboration with Dr. Long-Qing Chen – *Penn State*

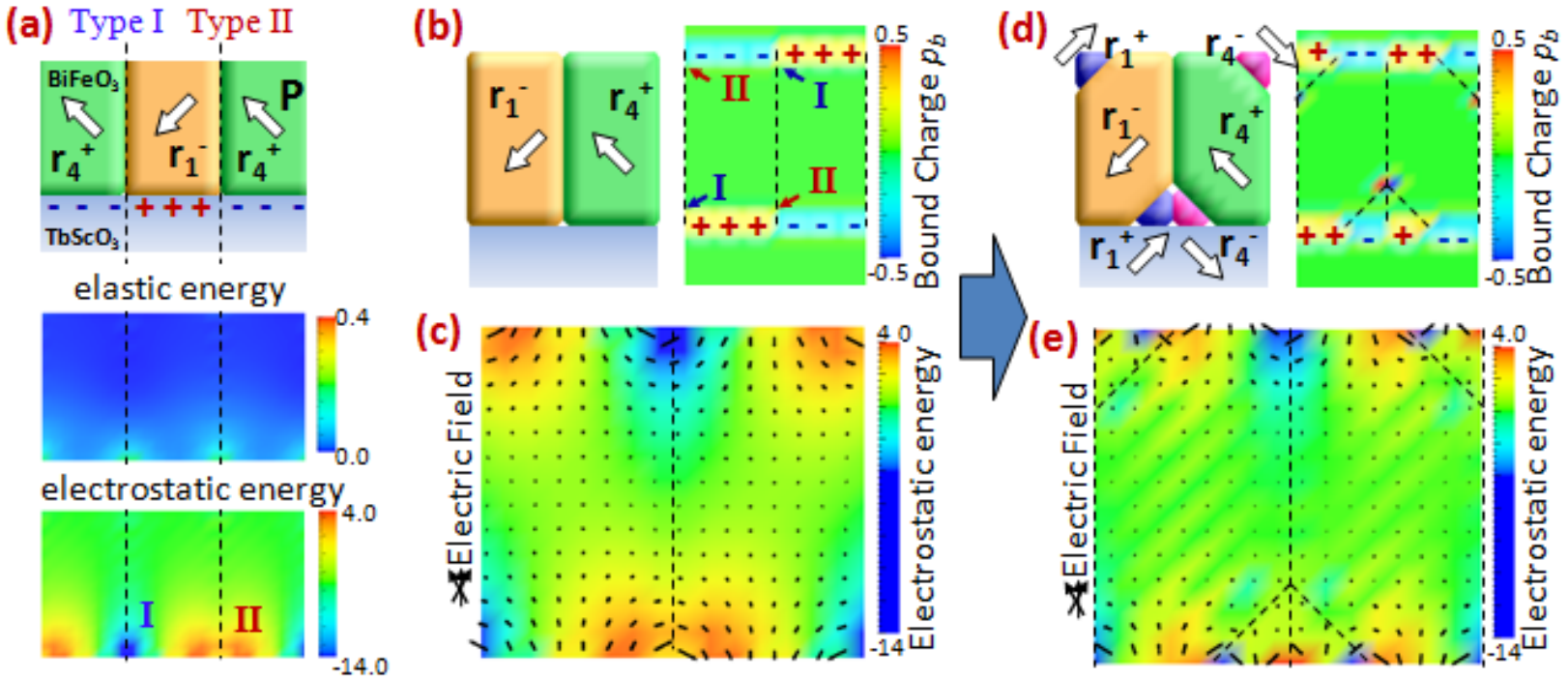

Fig. 4.3 Energy Contributions to the Formation of Vortex Domains
(a) The spatial distribution of the electrostatic and elastic energy density at an insulating surface of an unrelaxed 109° domain structure shows identical elastic energy between adjacent domain walls but distinct low (type I) and high (type II) electrostatic energies. **(b)**, Distribution of the bound charges at the 109° domain wall. **(c)**, A vector plot of the depolarization field overlaid with the electrostatic energy shows it is lowest (type I) when the surface fields are parallel to the in-plane polarization and highest (type II) when opposed. **(d)**, The electrostatic energy is intrinsically decreased by inserting 180° domains to compensate the depolarization field. This inserts a small region with favorably oriented surface charges. **(e)**, The depolarization field, and thus the electrostatic energy, is significantly reduced in the vicinity of the high energy boundary due to these compensating domains.

The high energy density of the type II domain wall termination is intrinsically reduced by the insertion of triangular 180° domains with the structure shown schematically in Fig. 4.3d. The bound charge of the vortex structure reduces the depolarizing field, and thus the electrostatic energy (Fig. 4.3e), versus the original structure (Fig. 4.3c) manifest by a reduction in the high energy region (colored red) at the domain wall termination. This polarization geometry is consistent with the domain patterns and locations observed experimentally (Fig. 3.13b). The local polarization distribution of the type I and vortex-relaxed Type II domain wall terminations were simulated by the time-dependent Ginzburg–Landau (TDGL) equation[110]. The resulting polarization distributions at the domain terminations (Fig. 4.1d,e) are in good agreement with the $\mathbf{D_{FB}}$ images (Fig. 4.1b,c).

The lowest energy equilibrium domain structure of the $BiFeO_3$ film was simulated by the phase-field method with no a-priori assumption of the final state[‡]. The simulation was initially seeded by a random distribution of r_1 and r_4 domains and allowed to relax under open-circuit boundary conditions at both the surface and the film/substrate interface, simulating vacuum growth conditions. The resulting film formed a 109° striped domain pattern with triangle vortex domains at both surfaces (Fig. 4.4a). The absence of the vortex domains at the free surface of the $BiFeO_3$ films (Fig. 3.14b) suggests that the depolarizing fields there are not large enough to promote their formation, most likely due to unavoidable screening charges from adsorbed species such as H^+ or OH^- at the top surface[135]. If this surface is compensated (short-circuit boundary conditions are applied) the triangle domains disappear, and the resulting domain pattern in Fig. 4.4b is a close match to the experimentally observed structure (Fig. 3.14b). That these vortex domains have not been previously observed may likely be due to either strain fields from misfit dislocations or the fact that most typical substrates provide too much charge screening, being either metallic (*e.g.*, having Pt or $SrRuO_3$ bottom electrodes) or semiconducting (e.g., $SrTiO_3$) under typical vacuum growth conditions. Our use of MBE grown films,

[‡] Provided by collaboration with Dr. Long-Qing Chen – *Penn State*

which uses a charge neutral molecular flux compared to charged plasmas from rf or laser sputtering, may also reduce screening during growth.

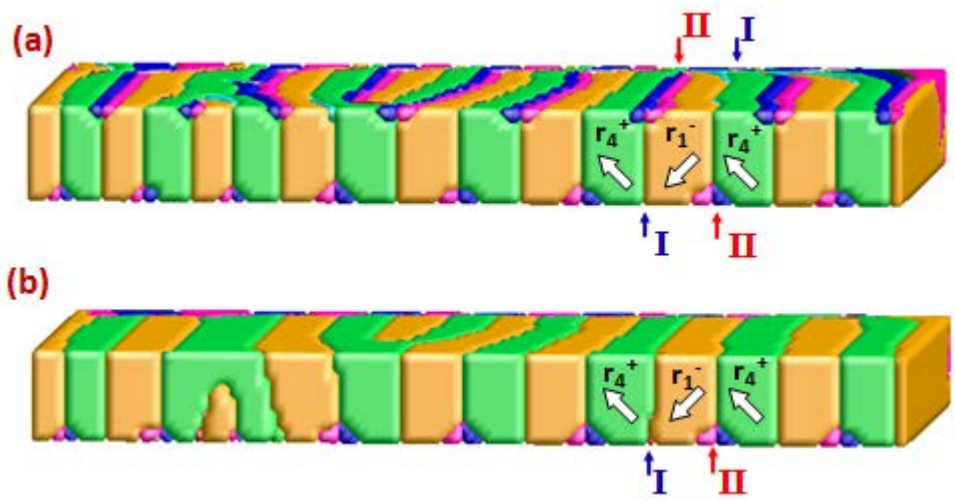

Fig. 4.4 Phase Field Simulations of the Equilibrium Domain Structure
Phase-field simulation of the $BiFeO_3$ domain structure coalesced from a random r1/r4 distribution. **(a)** The 109° domain pattern formed under open-circuit boundary conditions. **(b)** The triangle domains disappeared from the top surface after application of short-circuit conditions (compensation) to that surface.

Since the presence of the vortex domains is dependent only on the local field at the termination of the domain wall, there is no theoretical restriction to low-dimensional systems. We have observed vortex arrays in films up to 800 nm (the thickest we've examined), and they can well be expected to form spontaneously at bulk interfaces. Manipulating the film thickness provides tunability of the array of vortex domains since the 109° domain wall density scales with thickness[146]. Very thin films with two insulating surfaces, for example, would have a large volume fraction of vortex domains. By charge screening one surface, as we have in this experiment, one can produce a film with a single macro-scale toroidal moment. Even at large length scales, the vortex domains may significantly alter switching dynamics since reversed domains can grow from existing favorably oriented regions within the vortex domains instead of from a nucleation step.

In summary, a self-assembled array of ferroelectric vortex domains spontaneously forms at the interface between a $BiFeO_3$ thin film and an insulating $TbScO_3$ substrate. The

driving force for their formation is localized electrostatic energies where 109° domain walls terminate at the interface. The polarization closure is observed by mapping the electric polarization with atomic resolution via HRTEM images and exhibits non-bulk characteristics such as mixed Ising-Néel type domain walls and in-plane polarization up to twice that of the bulk film. Through comparison with phase-field simulations, we infer the presence and absence of free charge carriers at the film/air interface and the film/substrate interface, respectively.

Chapter 5

5 In-situ Ferroelectric Switching of Thin Films

5.1 Background

The majority of applications of ferroelectric materials require switching between polarization directions under an applied electric field. This process occurs through the nucleation and growth of domains with a favorable alignment of the polarization vector to the applied field vector. In a pure bulk crystal the theoretical energy required to form a stable nucleus is several orders of magnitude larger than experimental measurements. Thus, it was recognized early on that this process is inhomogeneous, dominated by defects which act as nucleation sites[46]. The high spatial resolution of TEM makes it ideal for studying defects and determining the local polarization distribution. The latter ability is especially important in ferroelectric film devices which require a specific polarization state at the interface[23,24,28]. In such cases bulk-switching is not sufficient, the presence of unswitchable, non polar, or inversion layers at the interface can poison the device functionality. There have been a number of TEM studies on the static structure near defects [120,126,128] and interfaces[103,147,148]. However, studies of the role these play in the dynamics of ferroelectric switching have heretofore been absent.

Since the actual physical defects underlying any given ferroelectric switching behavior are typically unknown, the defects are generally classified by their impact on ferroelectric switching itself. Those which locally break the degeneracy of the polarization states to favor one or more orientations are known as random-field defects (Fig. 5.1a) and those that change the barrier height affecting the transition between degenerate states are random bond defects (Fig. 5.1a), though a physical defect need not be purely a single type. In typical low-dimension ferroelectric structures such as thin films the most significant and the most voluminous defects in the crystal lattice are the interfaces. As shown in chapters 3 & 4, these interfaces also introduce internal depolarization fields

which will be superimposed onto the external field (a random field defect). However the increased energy due to the broken bonds at the surface reduces the nucleation barrier (a random bond defect). The combination of these effects and the omnipresence of the interface make it the dominant defect in ferroelectric switching. This has been observed repeatedly in macroscale switching studies[46]. However, the interface is itself inhomogeneous, displaying considerable variation in switching properties[99]. A multitude of optical, electrical, and surface probe studies have confirmed this defect-driven inhomogeneous switching but the defects responsible are below the spatial resolution limit of these methods.

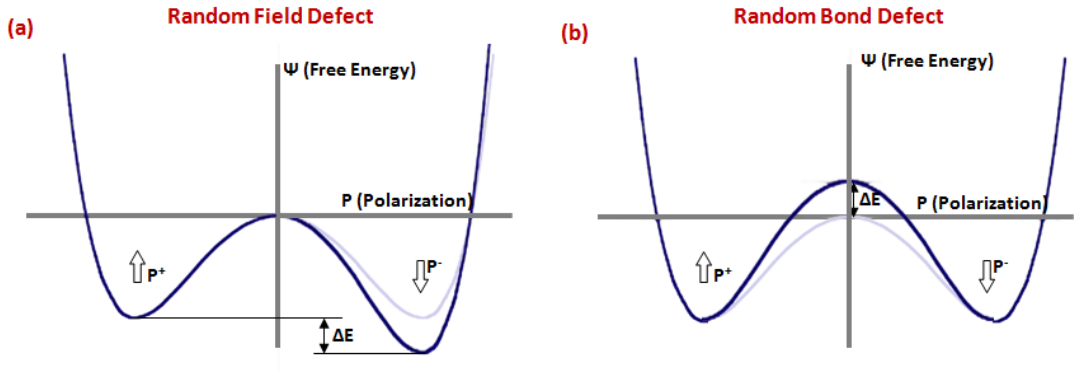

Fig. 5.1 Ferroelectric Switching Defect Types
Effect of defects on an example degenerate ferroelectric double-well energy diagram free energy vs. polarization **(a)** Random field defect breaks the degeneracy to favor a single state. **(b)** Random bond defect maintains degeneracy but changes the barrier height.

Until quite recently investigations of ferroelectric switching were done by either in-situ optical microscopy with polarized light[46,149,150] or ex-situ by selectively etching the surface using solvents with a removal rate which is polarization dependent[151]. These studies were responsible for early breakthroughs such as demonstrating the inhomogeneous needle-domain switching process. However, they have many limitations including difficulty in obtaining contrast between domains. In the former, experiments were restricted to materials which exhibited a change in refractive index under switching and not all domain wall types and orientations were usually visible. The diffraction limit of light also precludes any small scale measurements. The latter was destructive and showed only the relaxed near-surface structure.

Recent information on the properties of thin film switching has primarily come from surface probe microscopy techniques, particularly PFM (see section 2.2.3). This technique applies a highly localized electric field to the film surface using a conductive surface probe and measures the piezoelectric distortion. A subset of PFM which analyzes and images the variation in piezoelectric hysteresis at scan point, called switching spectroscopy PFM (SS-PFM), is especially useful for mapping local switching properties. PFM and SS-PFM studies have demonstrated preferential nucleation sites[99,152,153] and imaged lateral domain wall creep at high temporal resolutions[51,153,154] which fit well with theoretical models[47]. While it is highly effective at probing local switching properties, PFM is limited in characterizing the defects which give rise to those local properties. As a surface probe technique it is effectively blind to the dynamics along the normal-axis and only able to measure their aggregate response. The need to deconvolute the data by the probe shape and account for a variety of surface-probe interactions limits the effective resolution and can produce artifacts.

To date there are few reports of *in-situ* TEM studies of ferroelectric materials and these have primarily centered around paraelectric/ferroelectric phase transitions through the use of in-situ heating[155-160]. In-situ studies of ferroelectric switching by an electric field are even rarer. There have been reports on the electric field-induced domain formation and switching in $BaTiO_3$[161-164], PZT[165,166] and Sc-doped PMN[167] samples. Most active in the field have been Tan and Shang et. al. who observed electric field induced microcracking at grain boundaries in PZT[168] and PMN-PT[168-170]. However, all of these works were done on bulk, usually polycrystalline, samples and provide little insight into thin-film switching behavior or the role of defects. Additionally, such large complex geometries and structures make quantitative measurements impractical.

In this chapter we combine the local probing of switching behavior by SPM and the high resolution characterization of TEM in-situ to study electric-field induced switching in ferroelectric thin films. In addition to combining the advantages of these two methods the data obtained can be applied to the large body of SPM switching data available. Contemporary to the work detailed in this chapter have been two other SPM-TEM

publications studying phase transitions[171] and metastable switching[172] in $BiFeO_3$ thin films.

5.2 Experimental

Localized in-situ switching was performed on 100 nm (001) oriented $BiFeO_3$ and 100 nm (001) oriented $PbZr_{0.2}Ti_{0.8}O_3$ films using a freely positionable SPM probe incorporated into a TEM holder (schematic in Fig. 5.2a). A bias is applied between the tungsten surface probe and a grounded buffer electrode producing a localized electric field under the tip (Fig. 5.2b). For $BiFeO_3$ films this buffer electrode was a 20 nm epitaxial layer of $La_{0.7}Sr_{0.3}MnO_3$ and for $PbZr_{0.2}Ti_{0.8}O_3$ is was a 50 nm epitaxial layer of $SrRuO_3$. TEM switching was performed at voltages below any observation of electrical breakdown.

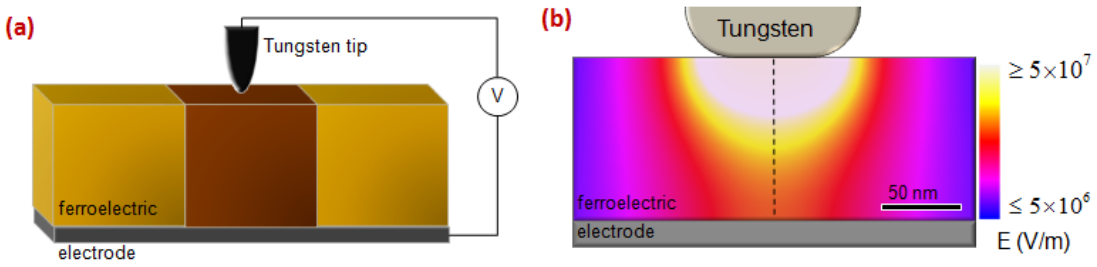

Fig. 5.2 In-situ Switching Geometry
(a) The geometry of the in-situ ferroelectric switching where a bias voltage is applied between a surface probe and a buffer electrode producing local inversion of the polarization. **(b)** The electric field distribution beneath the tip calculated from finite elemental analysis.

5.2.1 Film Growth

In situ switching was performed on 100 nm $BiFeO_3$ films grown by MBE on $(110)_O$ $TbScO_3$ substrates with a 20 nm $La_{0.7}Sr_{0.3}MnO_3$ buffer electrode* and on 100 nm $PbZr_{0.2}Ti_{0.8}O_3$ grown by rf sputtering on $(110)_O$ $DyScO_3$ substrates with a 50 nm $SrRuO_3$ buffer electrode†. An 800 nm thick $BiFeO_3$ film on $(110)_O$ $TbScO_3$ grown by rf sputtering† was used for characterization of the surface topography of a prepared TEM sample surface. The growth procedures are detailed in section 2.3.

* Provided by collaboration with Dr. Darrell Schlom – *Cornell University*
† Provided by collaboration with Dr. Chang-Beom Eom – *University of Wisconsin - Madison*

5.2.2 Characterization and Analysis

PFM experiments were carried out on an Asylum Research MFP-3D AFM using Umasch NSC18/Pt tips and on a Bruker Dimension Icon system using SCM-PIT Pt coated tips. Room temperature Hall measurements were performed with four-probe Van der Pauw configuration using a 0.22 T permanent magnet. A 1 nA driving current was applied by a Keithley 220 current source, and a Keithley 6517A high resistance meter recorded the voltage readings.

Specimen thickness in the region of switching (specifically from Fig. 5.13) was ~60 nm as determined by t/λ thickness maps using a JEOL 2100F where t is the thickness along the electron beam and λ is the mean free paths between plasmon scattering events. This method measures the relative number of electrons which have been inelastically scattered by plasmons which is proportional to the sample thickness. A (t/λ) map was generated by an unfiltered and an energy filtered TEM image using a 10eV selection window centered on the zero loss peak to isolate the signal from elastically scattered electrons. The sample was tilted several degrees off axis and away from low index planes to avoid diffraction effects. A proportionality constant of 0.7 λ / 100 nm was determined by thickness mapping a known thickness (100 nm) planar view $BiFeO_3$ sample lacking the $LaSr_{0.7}Mn_{0.3}O_3$ buffer layer in a region where orthorhombic $TbScO_3$ substrate diffraction spots first appear. The (t/ λ) map was scaled by this constant to give an absolute thickness map shown in Fig. 5.3. Although the mean free paths are probably similar for all three materials in the image, the calibration to absolute thickness is only strictly correct for the $BiFeO_3$ layer.

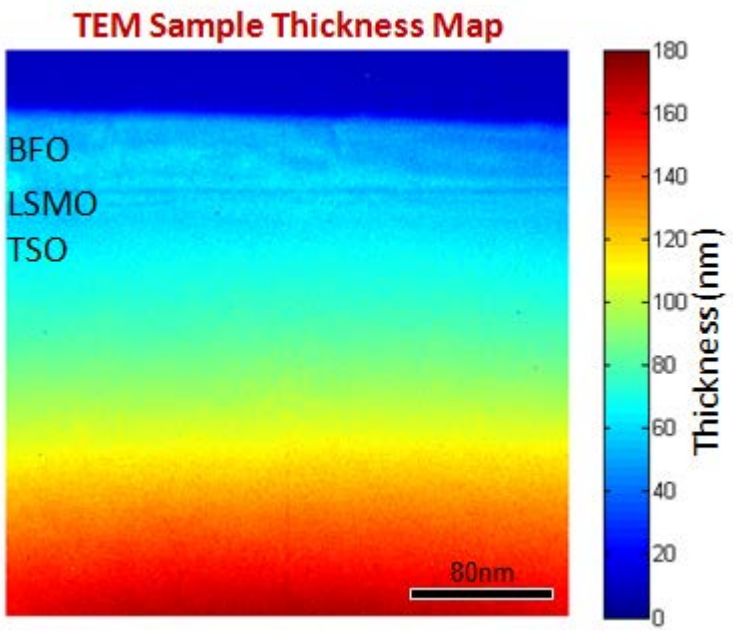

Fig. 5.3 Sample Thickness Map
Map of the sample thickness along the electron beam direction in a region used for ferroelectric switching, calibrated for the $BiFeO_3$ layer (top of image).

In-situ switching was performed in diffraction contrast TEM mode using a JEOL 2010F and JEOL 3011 microscopes in conjunction with a custom-designed Nanofactory TEM holder with a built-in scanning probe microscope (SPM). External voltages were applied using an HP 6614c for DC voltages, an HP 3324a function generator for waveforms, and a Nanofactory measurement system. The tungsten surface probe was placed in physical contact with the surface of the film for all switching experiments. The buffer $La_{0.7}Sr_{0.3}MnO_3$ electrode was grounded to the molybdenum TEM ring using silver paste. The probe was positioned so that its apex coincided with the apex of the film within ~4 nm along the electron beam axis (z) using an iterative process of 2 nm adjustments of the z-positioning piezo and making contact with the film. The 'center' position was assumed to be at the apex of the film height when the probe made contact while it was furthest retracted. Diffraction contrast images in Fig. 5.12 are tilted slightly off the (100) planes except Fig. 5.12a-5 which is tilted off the (001) planes, images in Fig. 5.13 are tilted slightly off the (-101) planes, and these are all respectively used as the image forming diffraction planes. Dark field images are aligned so the diffracted beam travels along the

optical axis to avoid aberrations. Videos were recorded by a (Gatan) TV-rate camera at 29 frames per second.

Post switching HAADF STEM imaging for polarization mapping was performed on a spherical aberration (Cs) corrected FEI Titan 80-300 operated at 300 kV (TEAM0.5 at LBNL). Polarization mapping was carried out according to the method described in section 3.3. HAADF STEM imaging of the dislocation segment in section was performed on a Cs corrected JEOL 2100F. The external electrical field was modeled by finite element calculations using Ansoft Maxwell software assuming tungsten as a perfect conductor and $BiFeO_3$ as an insulator with a resistivity of $2x10^3$ Ωm and a relative dielectric constant of 100. The tip contact was estimated as a 240 nm diameter sphere with a surface contact width of ~61 nm.

5.2.3 Ferroelectric Hysteresis Determination

TEM images of the film during switching provide a direct measurement of the size of the switched domain (see Fig. 5.4a). This corresponds to the change in the ferroelectric contribution to the polarization and can be used to plot spontaneous polarization v. electric field hysteresis loops (see Fig. 5.4b). This approach is advantageous since it isolates the spontaneous polarization contribution while ignoring dielectric or leakage effects and sources of electrical noise. It also provides much better spatial resolution than piezoresponse or electrical measurements since the piezoresponse and the switching current from such a small regions is also very small, below the shot noise in the case of electrical measurements. In oxide ferroelectrics the spontaneous polar contribution is usually the dominant contribution to the net polarization yielding equivalence of the TEM derived and electrical P-E loops.

Such P-E loops are very useful for quantitative analysis of the local switching properties. For example a P-E loop from cyclic switching of a $BiFeO_3$ film Fig. 5.4b shows a positive shift of the hysteresis loop indicating built-in fields or unequal nucleation/domain motion onset voltages. It also reveals a disparity in switching speeds between domain formation and reduction, and a pinning site on the rightmost edge in panel 3 producing a kink in the P-E loop.

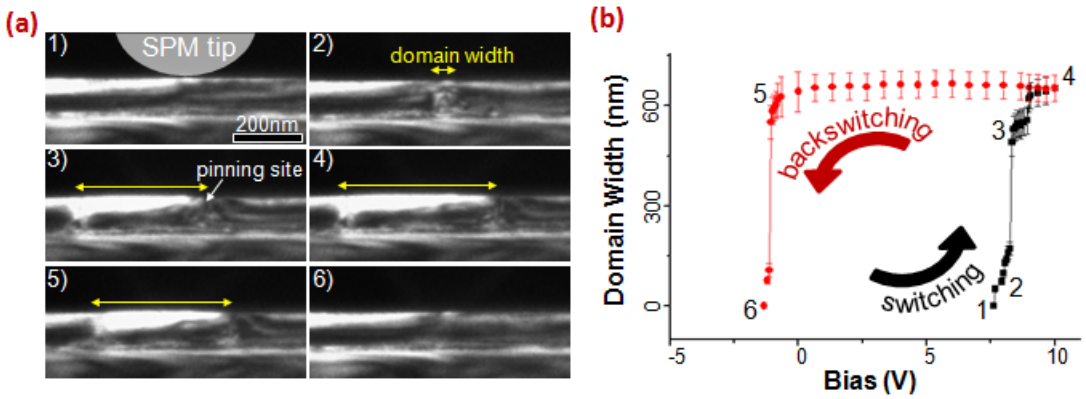

Fig. 5.4 Ferroelectric Hysteresis in TEM
(a) The area of polarization switching is determined directly from TEM images. The voltage is linearly increased from -10V to 10V (panels 1-4) then decreased back to -10V (panels 4-6) in a total of 20 s. The domain width is highlighted by the yellow arrow. **(b)** The P-E hysteresis loop determined from the projected domain size. Several selected data points in the loop are labeled with the corresponding images in (a). Point 3 depicts a region where the right domain wall is momentarily pinned before expanding to its final size in panel 4. Backswitching begins at a much smaller bias (5) and occurs more rapidly than the initial switching (1).

5.2.4 Conduction Properties & Electron Beam Interaction

Current vs. voltage curves were taken in situ to characterize the electrical properties of the tip/ferroelectric/electrode capacitor structure. Current conduction in electrode-buffered insulating ferroelectric materials is typically dominated by one of four mechanisms: Schottky injection, Poole-Frenkel hopping, Fowler-Nordheim tunneling, or space-charge limited currents[54,173]. Schottky injection is the thermal emission of carriers over a Schottky barrier. The lowering of this barrier by image charges under the application of a bias leads to a $I \propto e^{-aV^{1/2}}$ dependence (α is a constant at fixed temperature). Poole-Frenkel hopping is the thermally or field activated carrier hopping between traps and has the same voltage dependence as Schottky injection. However, the two can be distinguished either by the temperature dependence or the IV curve asymmetry (Schottky is generally asymmetric). Space charge limited conduction (SCLC) is the limitation of current by the build up of space charge and has a power law dependence $I \propto V^{\alpha}$ where α is a constant which generally lies between 3/2 and 2[174,175]. Fowler-Nordheim tunneling is the tunneling *through* a potential barrier such as a Schottky junction or the rapidly decaying potential at the apex of a sharp probe[23] and has an $I \propto V^2 e^{\alpha/V}$ dependence[176]. Over short ranges or at the limit of very small barriers (α→0) FN tunneling mimics the IV characteristics of SCLC and the two can be difficult

to distinguish. However, SCLC is the more commonly reported mechanism in ferroelectric films. These four conduction mechanisms are not mutually exclusive and can dominant at different voltage regimes within a single specimen[54,177,178].

IV curves taken in situ from bias between the tungsten probe/$BiFeO_3$/$La_{0.7}Sr_{0.3}MnO_3$ structure are shown in Fig. 5.5. Both the positive and negative branches are approximately symmetric and follow a power law $I \propto V^k$ where k≈2, as highlighted by the dashed fit lines on the linear and log-log plot (Fig. 5.5a inset). The power law behavior suggests conduction is bulk limited by SCLC[174]. A similar power law was observed on large 20 μm electrodes ruling out FN tunneling at the tip/surface and it is extremely unlikely that given the asymmetry of the electrodes that FN tunneling through Schottky junctions would be symmetric. Further, many curves exhibit a sharp jump at low voltages indicative of crossing the trap filling voltage which is characteristic of SCLC. Comparative IV curves using two different probe metals: Tungsten and Platinum/Iridium are shown in Fig. 5.5b. Both metals show identical trends offset by a small linear scaling which is attributable to dissimilar contact areas between the two tips. The insensitivity to surface contact further suggests a bulk-limited conduction method, i.e. SCLC or Poole-Frenkel hopping, of which only SCLC fits the observed voltage dependence. Unfortunately, bulk-limited conduction also prevents electrical characterization of the electrode interface by IV measurements.

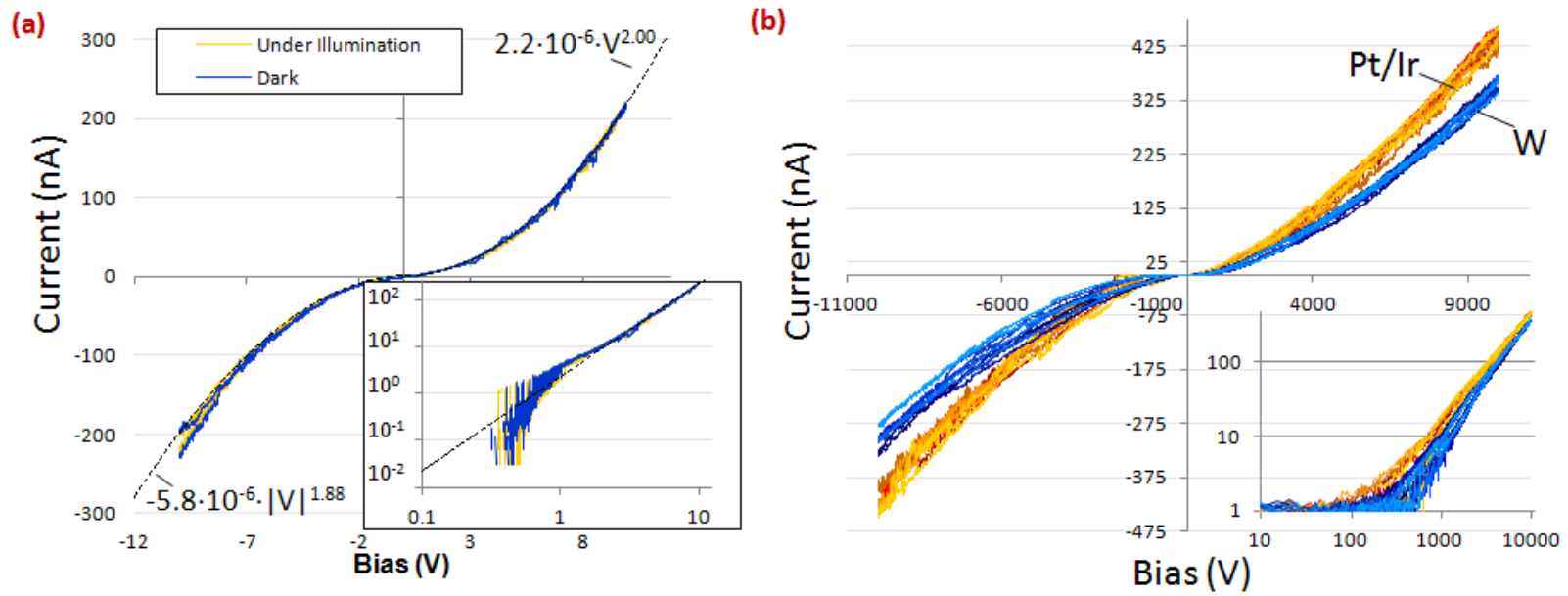

Fig. 5.5 Current Conduction of $BiFeO_3$ Films & Electron Beam Insensitivity
(a) Current vs. Voltage curves of the surface probe/$BiFeO_3$/$La_{0.7}Sr_{0.3}MnO_3$ heterostructure. Both the positive and negative branches fit a power law function (dashed lines). The conduction current is insensitive to the TEM imaging electron beam shown by IV curves under illumination (yellow) and in the dark (blue). **(b)** Multiple overlaid comparative IV curves using two surface probe metals: Tungsten (blues) and Platinum/Iridium(oranges). The symmetric power law trend which is insensitive to the surface metal suggests bulk-limited SCLC.

One frequent concern with TEM imaging is the influence of the high dose of electron radiation to the region under study. Although the oxide films in this work are highly resistant to damage from the electron beam, some discussion is necessary concerning how the incident electrons might affect the electric fields across the sample and thus the switching data. The majority of the incident electrons scatter elastically, however a small percentage scatter inelastically causing ionization of the atoms. This can lead to various forms of energy emission including secondary electrons, Auger electrons, and X-rays (see section 2.1). For typical sample thickness and beam energies of TEM, this electron emission far exceeds the absorption of the incident electrons into the sample and causes a net positive charge to form which is neutralized by a steady-state influx of electrons from the surrounding area[179]. The magnitude of this effect is extremely difficult to quantify since the ionization cross sections and the corresponding Auger electron conversion efficiencies have only been determined for the inner-shells which pertain to X-ray emission[180]. These values are not known for outer orbitals of high Z elements (such as Bi and Pb). To measure the effect of beam charging in the ferroelectric samples IV curves were taken under illumination and in the "dark" (see Fig. 5.5a). Sample charging should manifest as a positive current offset due to a flux of electrons being extracted from the large-area buffer electrode to recombine with the holes formed by the beam. There was no detectable difference in the IV curve between the two cases. This means that carrier distribution as a result of charging is negligible compared to the electrode-injected and depletion effects and should not make any discernable contribution to the electric fields. Furthermore, all switching was performed under parallel illumination so that all regions of the sample receive an identical electron flux and no charging gradients are present in the vicinity of the viewing region.

Ferroelectric films were grown by two different methods: molecular beam epitaxy and rf sputtering. The defect chemistry of thin films is known to vary with processing conditions and growth method as demonstrated by cathodoluminescence studies of $BiFeO_3$[181]. MBE in particular is sensitive to off-stoichiometry[182] which can drive up the leakage currents[183]. To compare the electrical quality of the sputtered and MBE films, IV

curves were taken of each type (Fig. 5.6a) using the same tungsten tip (Fig. 5.6b) to guarantee identical surface contact area. The leakage current of the MBE film is only 7.4 times that of sputtered films and follows the same ~V^2 trend suggesting an identical conduction mechanism: either space charge limited conduction or (unlikely symmetric) Fowler-Nordheim tunneling across the junctions. In the former case, a thickness (d) dependence of d^{-3} corresponds to conductivity in the MBE films 59 times that of the sputtered films. In the latter case, there is no thickness dependence so the conductivity is 7.4 times that of the sputtered films. Although sputtered films showed better electrical qualities, they typically have less regular domain structures and inhomogeneous strain contrast (Fig. 2.7). For switching studies in particular, the MBE grown films were found to have a much simpler monodomain structure and better suited to study nucleation from a single-domain region. The difference in conductivity of only one order of magnitude is small enough that film degradation and MBE-specific switching behavior are not a concern and so MBE films were used. $PbZr_{0.2}Ti_{0.8}O_3$ films were all grown by sputtering.

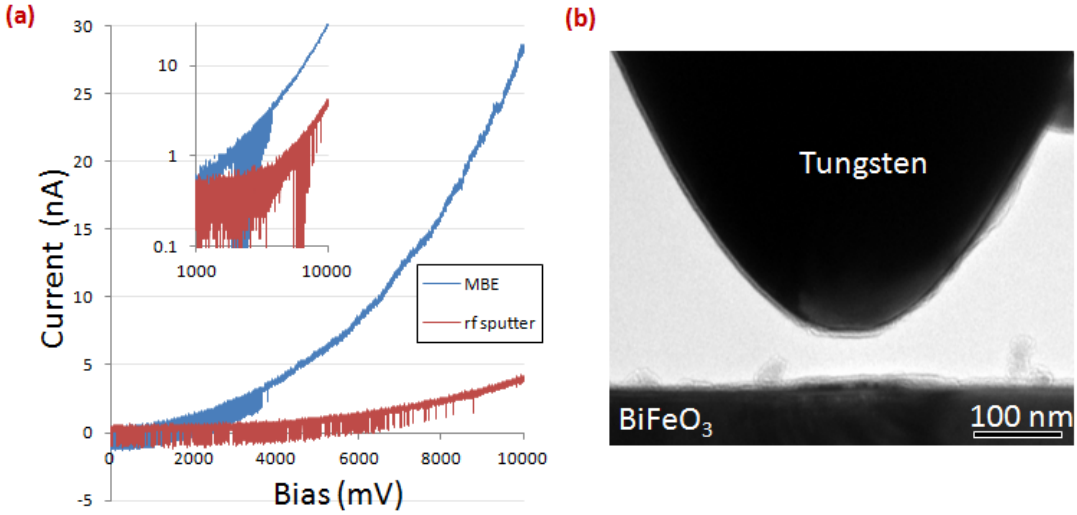

Fig. 5.6 Conduction vs. Growth Method
(a) Comparative current vs. voltage curves for the tungsten probe/$BiFeO_3$/electrode heterostructure of MBE and rf sputter-grown films. **(b)** The same tungsten probe was used for both samples to guarantee ~identical surface contact areas.

5.2.5 Contact Stress

All switching experiments were performed with the probe in physical contact with the top surface of the film. Since diffraction contrast images are very sensitive to strain the contact stresses are kept very small but they are non-zero. The tip was located at the sample surface within 2 nm (the step size used for the normal axis positioning piezo). Given a worst case scenario of a 2 nm indentation, and assuming the tip as a uniform circular plane (r = 30 nm) of constant applied pressure into an isotropic elastic half-space, the applied pressure can be determined from[184]:

$$u_z = -\frac{2\cdot\left(1-\upsilon^2\right)\cdot p\cdot r}{\pi\cdot E} \qquad 5\text{-}1$$

Where u_z=2 nm is the displacement, ν=.35 is Poisson's ratio, p is the applied pressure, and E=63 GPa is the modulus of elasticity. The 2-D normal strain distribution from a uniform line traction at this pressure takes the form[184]:

$$\sigma_z(y,z) = -\frac{p}{2\cdot\pi}\cdot\left(2(\theta_1-\theta_2)-(\sin 2\theta_1-\sin 2\theta_2)\right) \qquad 5\text{-}2$$

where θ_1 and θ_1 are the angles from the two edges of the indenter to the given coordinate. For the 2 nm indentation of PZT this distribution is shown in Fig. 5.7a. The normal stress in the 3-dimensional case using the same uniform pressure on a circle of r=30 nm has the depth profile at the tip center[184]:

$$\sigma_z(0,0,z) = -p\cdot\left(1-\frac{z^3}{\left(r^2+z^2\right)^{3/2}}\right) \qquad 5\text{-}3$$

Including the tangential stress:

$$\sigma_r(0,0,z) = -p\cdot\left(\frac{1+2\cdot\nu}{2}-\frac{z\cdot(1+\nu)}{\left(r^2+z^2\right)^{1/2}}+\frac{z^3}{2\cdot\left(r^2+z^2\right)^{3/2}}\right) \qquad 5\text{-}4$$

and using Hooke's law the depth profile of the strain is shown in Fig. 5.7b. The polarization which results from the flexoelectric contribution depends on the strain gradient which is shown in Fig. 5.7c. A flexoelectric constant for PZT of f = 0.5 μC/m and a dielectric constant ε_r = 20,000, both from ref 185, are used to determine the induced

polarization. This polarization is generally expressed as an "equivalent field" or the electric field to induce the same polarization from the linear dielectric response:

$$P = \varepsilon_r \cdot E \qquad 5\text{-}5$$

where E is the electric field, P is the polarization induced by flexoelectricity and ε_r is the relative permittivity. The equivalent field is shown in Fig. 5.7d and ranges from –3.4 to 1.4 MV/m. The largest absolute value occurs at the tip contact point where the rough approximation of a uniform pressure is least accurate but this conservative value is still over an order of magnitude smaller than the other built-in fields derived later in this chapter. Furthermore, a flexoelectric contribution should produce variation between experiments dependent on the contact pressure, which is not observed in our work. Most importantly, flexoelectric effects would produce similar phenomenon in both PZT and $BiFeO_3$ films which this chapter will also show is not the case. Thus contact stress is not considered as a significant contribution in the work which follows.

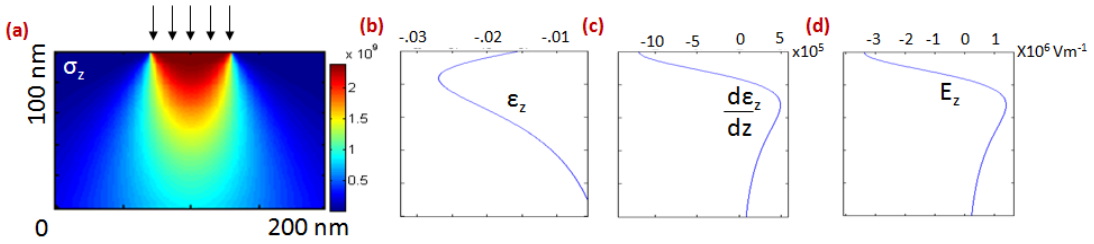

Fig. 5.7 Contact Stress, Strain, and Induced Polarization
(a) 2-D distribution of normal stress underneath a uniform line distribution of pressure corresponding to a 2 nm surface deflection. **(b)** Normal strain at the tip center axis of a 3-D compressed elastic half space. **(c)** the strain gradient along the film depth. **(d)** The equivalent electric field corresponding to the flexoelectric induced polarization.

5.3 Switching of Rhombohedral $BiFeO_3$

Ferroelectric switching was performed on a (001) oriented 100 nm $BiFeO_3$ film by applying a bias between the surface probe and grounded 20 nm $La_{0.7}Sr_{0.3}MnO_3$ buffer electrode. The bias results in an inhomogeneous out-of-plane electric field in the $BiFeO_3$ film promoting a transition amongst the eight possible $<111>_P$ polarization directions between the four "up" and four "down" orientation states. Three types of switching are possible, classified by the angular rotation of the polarization vector during switching: 71°, 109° or 180°. A 71° reversal along the electric field direction is generally reported

as the initial preferred switching direction[52,80,186], although the strain induced by such ferroelastic switching paths can lead to gradual backswitching[79] or further rotation to non-ferroelastic 180° switching[80]. The character of the switching is particularly import for $BiFeO_3$ since magnetoelectric coupling with an adjacent ferromagnet, such as the $La_{0.7}Sr_{0.3}MnO_3$ layer, requires a ferroelastic switching path[30].

The dynamics of this switching process in thin films are only experimentally known for the lateral domain wall creep phase of growth. Theoretical modeling of the switching in this geometry predicts a single nucleation event at the surface, the point of highest external field, after which the domain rapidly propagates across the film followed by slow lateral growth. A phase field simulation of surface probe induced switching in a $BiFeO_3$ film[‡] is shown in Fig. 5.8. The simulation is $128\Delta x \times 128\Delta x \times 32\Delta x$ cells in size, with a 14 Δx $BiFeO_3$ film height and 14 Δx $TbScO_3$. The external electric field is estimated as a Lorentzian function from a 4.7V bias with gamma equal to the film thickness, i.e. 100 nm, corresponding to a HWHM of 50 nm which is a close approximation to typical switching voltages and probe contact diameters in this work. Switching occurs by the 71° rotation of the normal axis from $P_{[11_1]}$ to $P_{[11\bar{1}]}$. The "needle domain" shape and rapid forward domain growth are due to the unstable charged domain wall at the leading edge of the propagating domain tip.

[‡] Provided by collaboration with Dr. Long-Qing Chen – *Penn State*

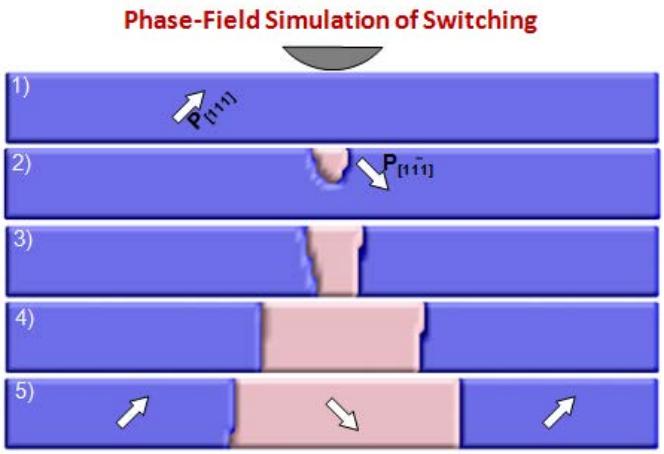

Fig. 5.8 Phase Field Simulation of Switching in $BiFeO_3$ by a Surface Probe
Time series from a phase field simulation of ferroelectric switching in a (001) $BiFeO_3$ film equivalent to a 4V bias between a probe and buffer electrode in a 100 nm film. Nucleation of a 71° rotated $P_{[11\bar{1}]}$ domain from the $P_{[111]}$ host occurs at the free surface directly below the probe (2). Growth proceeds rapidly along the film axis and expands slowly laterally.

5.3.1 Primary Domain Switching

Piezo-response force microscopy (PFM) of the MBE grown $BiFeO_3$ films indicate they are predominantly upward poled. Application of a dc positive bias leads to local switching shown by the out-of-plane PFM phase image in Fig. 5.9a for a probe bias of 20.6 V with a 2 s dwell time. The result is a circular downward poled domain (blue) ~400 nm in diameter which agrees with the final structure of the phase field simulation.

A cross-section of the same 100 nm $BiFeO_3$ film was thinned to electron transparency and switched in-situ. Cross sectional TEM micrographs of the domain structure pre- and post-switching by a 4 V dc bias are shown in Fig. 5.9b. A ~270 nm wide $P_{[11\bar{1}]}$ domain forms from the initial $P_{[111]}$ state, corresponding to the same 71° switching path observed in the full film and predicted by the phase field simulation. The projected polarization direction was determined from polarization mapping[125,145] (section 3.3). The polarization along the optic axis was inferred to be unchanged due to the wide vertical domain walls (Fig. 3.8) which would correspond with smearing due to the (110) equilibrium plane of 71° switching. A change of polarization along the optical axis would produce 109° switching with edge-on equilibrium domain wall planes along (010) which appear

atomically sharp (Fig. 3.7a). Furthermore, there is little in-plane driving force and no anisotropy to account for switching along only one in-plane direction.

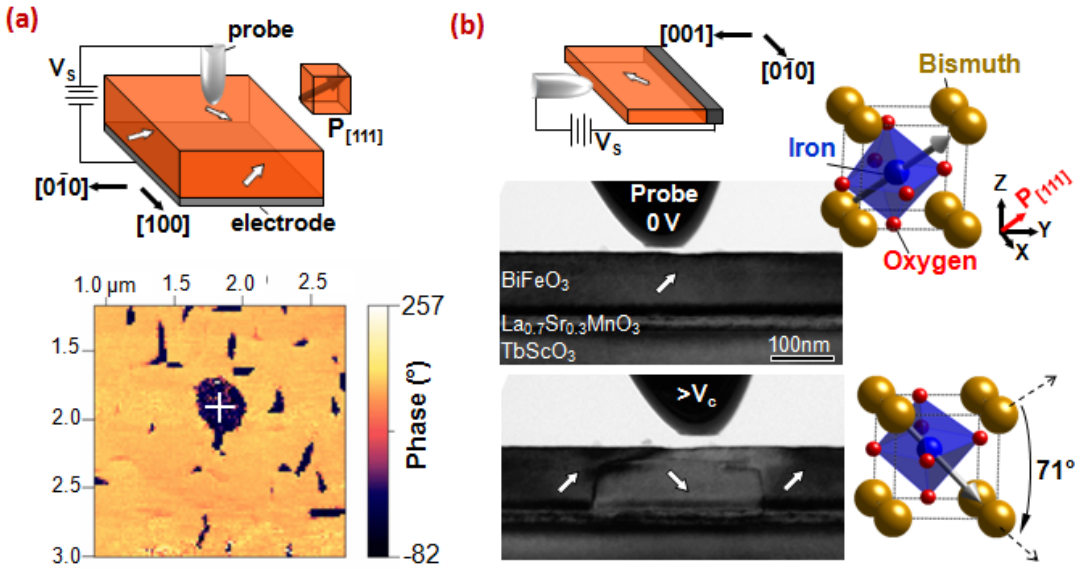

Fig. 5.9 $BiFeO_3$ switching by a Surface Probe
(a) An out-of-plane PFM phase image shows the reversed downward poled domain formed by application of a 20.6 V bias to a probe on the surface of the thick 100 nm $BiFeO_3$ film. **(b)** A thin cross sectional TEM image of the same film before and after switching by a 4 V bias. Switching occurs by 71° rotation of the polarization beneath the tungsten tip.

The nucleation of ferroelectric domains occurs when the applied field exceeds a critical nucleation threshold, i.e. the coercive field, which is subject to regional variation from defects[99]. The high field concentration formed at the tip of the surface probe is generally assumed to dominate over any built-in electric fields, such as from Schottky junctions, and initiate switching at the free surface where the applied field is highest. However, a chronological series of TEM micrographs in Fig. 5.10a of 71° $P_{[111]}$ to $P_{[11\bar{1}]}$ switching during a slow ramp of the DC probe bias from 0 to 4 V, clearly shows multiple nucleation events occurring exclusively at the bottom interface. Indeed finite element analysis of the out-of-plane electric field, E_Z, for this tip geometry at 2 V bias (Fig. 5.10b) shows a strong field concentration at the free surface. Hall measurements performed on non-buffered 100 nm $BiFeO_3$ films display an n-type conductivity. Inclusion of built-in electric fields from Schottky barriers of 0.85 V and 0.77 V from junctions of n-type $BiFeO_3$ with $La_{0.7}Sr_{0.3}MnO_3$ and Tungsten, respectively[187], produces the E_Z field

distributions shown in Fig. 5.10c. There is a broad band along the $La_{0.7}Sr_{0.3}Mn0_3$ interface where $P_{[11\bar{1}]}$ nucleation is likely to occur due to a strong negative field (pointed toward the substrate), in agreement with TEM observations. The electrical properties of the Schottky junctions could not be probed since conduction was bulk-limited by SCLC (section 5.2.4) however they are common feature of planar ferroelectric oxides[54,111] and known to determine nucleation sites between symmetric planar electrodes in $BiFeO_3$ films[186]. The relative strength and distribution of the built-in fields vary given assumptions about the Schottky barrier heights, the depletion width, and the electrode geometry. An accurate model requires knowledge of the surface states at the probe/$BiFeO_3$ junction. Regardless, the field approximation in Fig. 5.10 and obvious interface nucleation shows that the built-in fields can be at least of the same order of magnitude as the tip field and cannot be neglected.

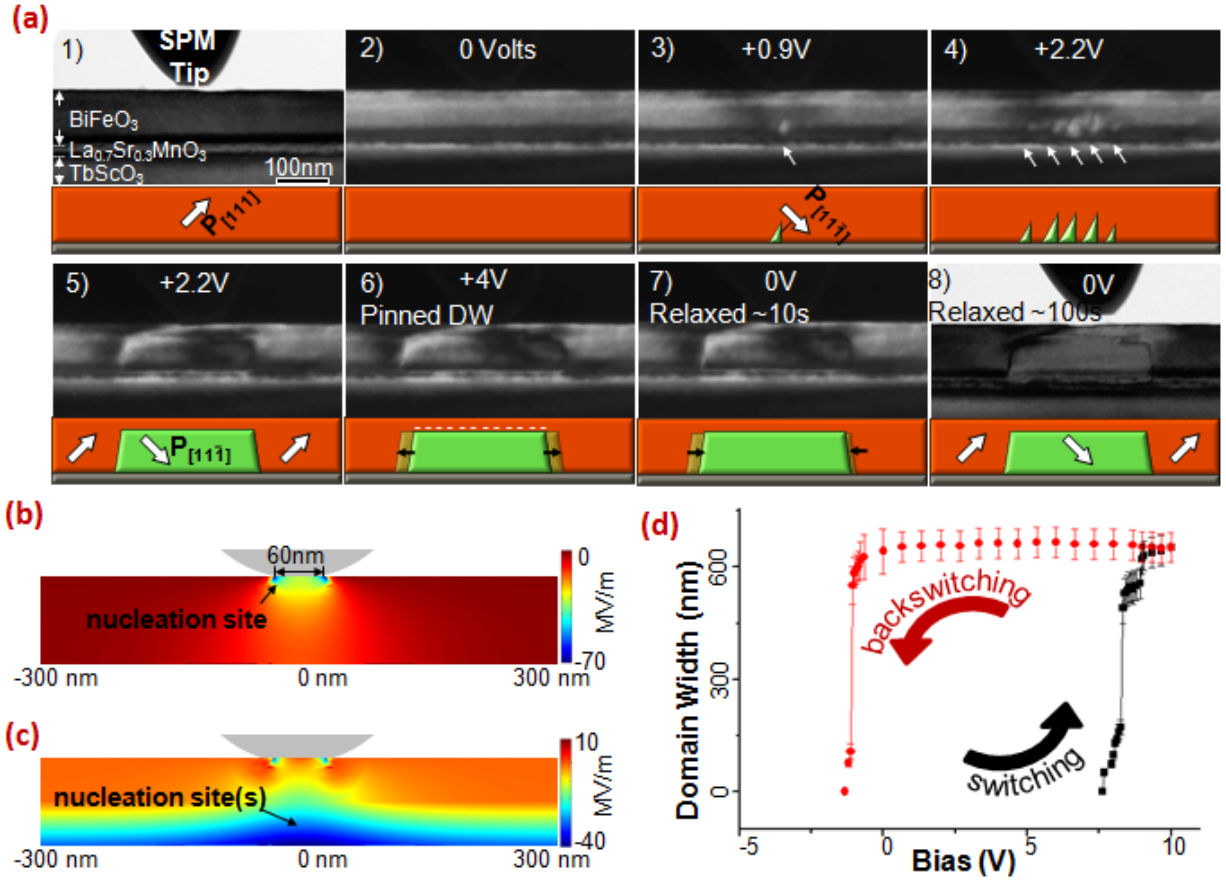

Fig. 5.10 71° Primary Switching of $BiFeO_3$

(a) A chronological TEM dark field image series, g=$(040)_P$ depicts the evolution of a $P_{[11\bar{1}]}$ domain in a single domain $P_{[111]}$ film. Nucleation occurs at the $La_{0.7}Sr_{0.3}MnO_3$ electrode interface at 0.9 V (1-3) producing a metastable stationary domain. Additional bias increases the size and number of these domains up to 2.2 V (4). At 2.2 V the domains merge and propagate forward just short of the surface (5) where they remain pinned along a (001) plane even after the voltage is nearly doubled (6). **(b)** Normal component of the electric field from the surface probe. **(c)** Normal component of the electric field including top and bottom Schottky junctions. **(d)** A ferroelectric hysteresis loop formed by the primary 71° switching as determined by the area of a switched domain.

The triangular domains that first nucleate at the $La_{0.7}Sr_{0.3}MnO_3$ interface are metastable, increasing (compare Fig. 5.10a-3 to a-4) or decreasing their fixed size with the applied bias. Multiple nucleation events occur before a critical voltage of 2.2 V whereupon they coalesce and expand into a single domain which reaches its full forward extent within a single 30 ms data sample. The triangular shape of these domains helps to minimize depolarizing fields as the domain walls orient closer to charge neutral (011) planes. During this low field region of thermodynamically limited switching, nuclei extend ~200 nm laterally across the interface, over three times the contact area of the tip. Such delocalization of switching under a localized field may be an important consideration for surface probe measurements. More fundamentally this process is a departure from the kinetically-limited models used to describe ferroelectric switching[54]. This is important for electrical characterization since the switching transient does not necessarily represent all of the switching current nor correspond to the actual nucleation bias.

The metastable behavior indicates an intrinsic thermodynamic instability of the nuclei such as from positive built-in fields or an accumulation of strain which destabilize the domain away from the interface. We do not see this behavior in similar nonferroelastic 180° switching of tetragonal $PbZr_{0.2}Ti_{0.8}O_3$ films suggesting that strain from ferroelastic 71° switching is a contributing factor. Hysteresis loops measuring the switched domain area during cyclic switching under the probe have a strong positive voltage offset indicating there is also a positive built-in field (Fig. 5.10d). The reduction of this offset during cycling (Fig. 5.11) suggests it may be the result of polar defects "imprinted" to the original $P_{[111]}$ polarization[188] which disassociate during cycling. An offset is also expected due to dissimilar electrode thermal histories and work functions (4.8 eV for $La_{0.7}Sr_{0.3}MnO_3$[189] versus ~4.5 eV for polycrystalline tungsten[190]) but both effects favor the negative field Schottky junction and a negative shift. It should also be noted that because the positive voltage branch switches by a nucleation event and the subsequent negative voltage branch backswitches by the shrinking of the switched domain an offset can result even in the absence of a built-in field since the critical field for nucleation and threshold field for the onset of domain wall creep need not be the same.

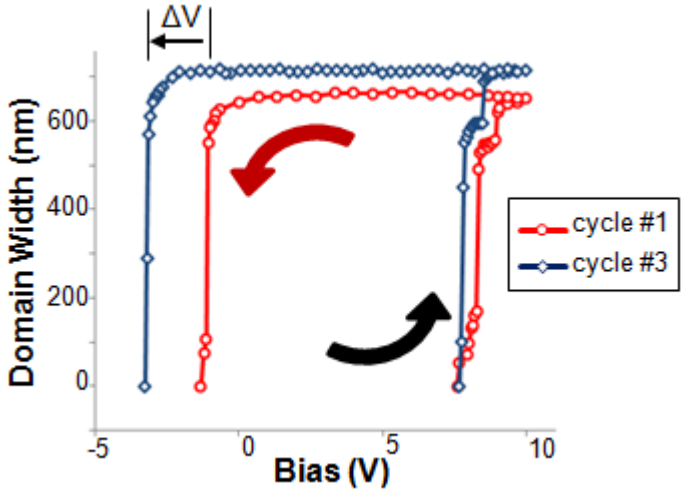

Fig. 5.11 Hysteresis Offset During Cycling
Aging effects evidenced in sequential hysteresis loops. The switched domain area of the $BiFeO_3$ film is shown for two triangle wave switching cycles. The third switching cycle, although it has the same features as the initial cycle, has a smaller positive voltage offset and a wider loop. One explanation for this behavior is the disassociation of polar defects which were initially aligned to the as grown $P_{[111]}$ polarization and promote backswitching to this state. The sample began at -10V and was given single triangle pulses, ramping up to 10V and back in 20 seconds with a ~15 second pause between cycles.

5.3.2 Interfacial Domain Switching

The 71° polarization reversal accounts for the majority of the area beneath the probe and corresponds well with previous reports from surface probe measurements[80]. The character of the switching at the ferromagnetic $La_{0.7}Sr_{0.3}MnO_3$ buffer electrode is critical for magnetoelectric applications, specifically 71° or 109° switching must occur at the interface. However, in-situ TEM switching shows there is a thin layer of film along the $La_{0.7}Sr_{0.3}MnO_3$ electrode layer which undergoes an independent switching process from the primary domain. A chronological TEM image series in Fig. 5.12a shows the domain structure evolution as the film is biased from -10 V to 20 V and back to zero. At small positive bias long horizontal domains confined to the interface appear (see Fig. 5.12a-2) and increase in height with increasing bias. Ultimately a primary 71° switched $P_{[11\bar{1}]}$ domain forms directly beneath the tip (Fig. 5.12a-3). Both the interfacial and primary domains persist after the bias is removed (Fig. 5.12a-4). Dark-field images formed from reflections of the (01l) planes (Fig. 5.12b) indicate that the interfacial domains (not seen) do not form the same ferroelastic twin with the unswitched region as the primary domain (bright). Polarization mapping from HAADF images confirm that the interfacial domains

undergo a different non-ferroelastic 180° polarization rotation (see Fig. 5.12c). The switching thresholds of the interfacial domains have a large negative voltage offset compared to the primary domain. They have a lower nucleation bias and form several hundred nanometers away from the tip. In contrast they require much larger negative voltages to erase due to the need to overcome the negative field in the Schottky junction where they are located.

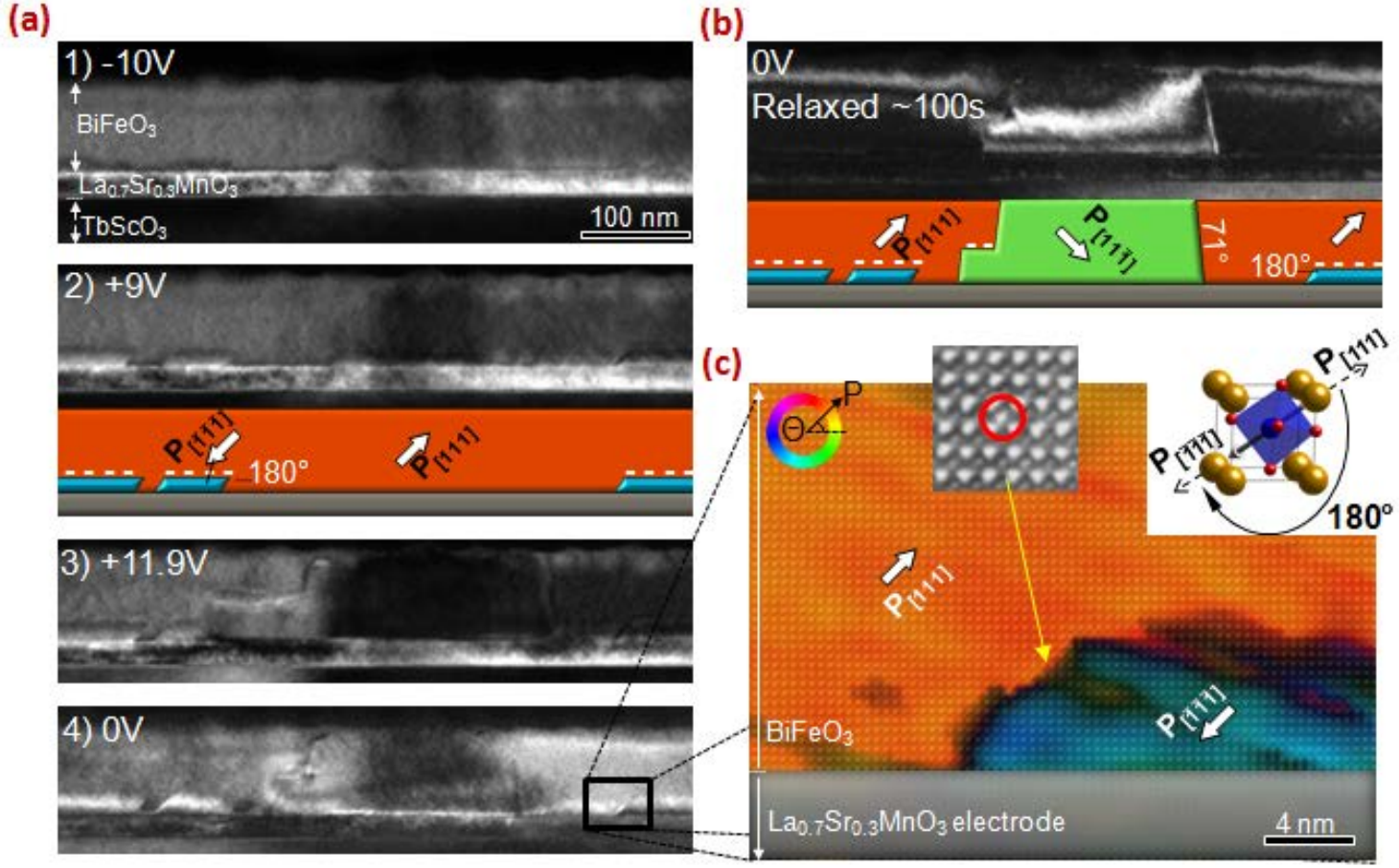

Fig. 5.12 180° Interface Switching of $BiFeO_3$

(a) A chronological TEM image series of the $P_{[111]}$ $BiFeO_3$ cross section as the voltage increases from -10 V to +11.9 V (1-3) and back to zero (4) formed from g=(040) diffraction of the vertical planes and **(b)** g=$(04\bar{4})$ diffraction of inclined planes. 180º rotated $P_{[\bar{1}11]}$ interfacial domains and a 71º rotated $P_{[11\bar{1}]}$ primary domain appear sequentially, shown by the accompanied schematics. **(c)** A high-resolution Z-contrast image shows the polarization distribution at the edge of an interfacial domain where the color and its intensity correspond to polarization angle and magnitude respectively. The inset figure is an example of a point defect located at the domain wall.

The lateral edges of the interfacial domains are charge neutral (011) 180° domain walls. However, the nominally (001) horizontal domain wall is unfavorable due to its negative charge from the tail to tail polarization vectors. Its graded appearance indicates that it is not a sharp (001) boundary but is inclined or corrugated to reduce the depolarizing field. Despite the energy cost of this domain wall, the interfacial domains exhibit long term stability (>6 months and ongoing). While the interfacial domains and primary switched domain do not overlap in Fig. 5.12a,b, Fig. 5.13 shows a region with an interfacial domain directly beneath the tip prior to switching (Fig. 5.13a). The subsequent formation of the primary 71° domain does not consume or otherwise alter the interfacial domain except to create a sharper (001) domain wall since the domain wall charging is absent (see Fig. 5.13b).

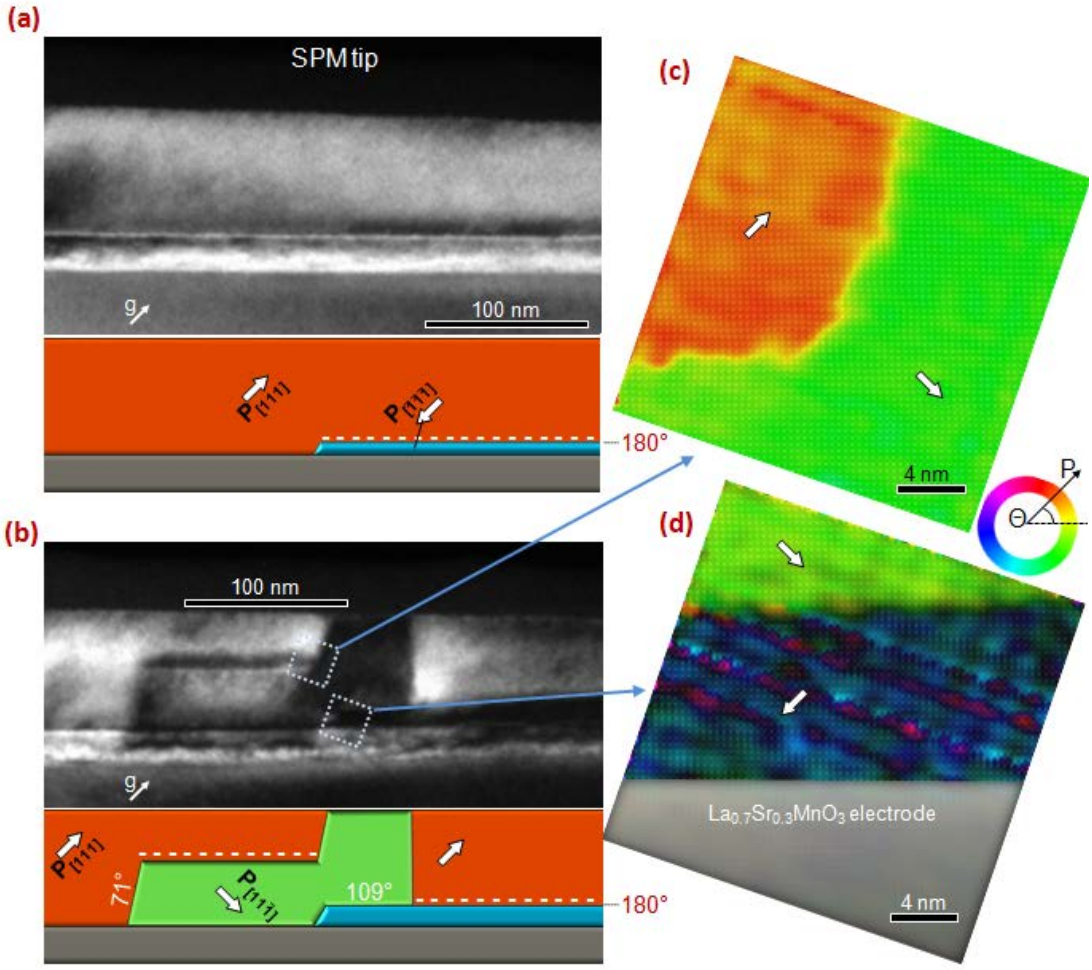

Fig. 5.13 Polarization Maps of Coincident 71° and 180° Switching
A region of $P_{[111]}$ $BiFeO_3$ film is switched in the vicinity of a 180° $P_{[\bar{1}\bar{1}\bar{1}]}$ interfacial domain. **(a)** The interfacial domain appears as a dark band on the right half of the dark field TEM image, g=(044), as shown in the corresponding diagram. **(b)** A $P_{[11\bar{1}]}$ domain formed by subsequent switching of this region with the left side pinned mid-film producing a negatively charged domain wall. Polarization maps from the highlighted regions show there is **(d)** a single $P_{[11\bar{1}]}$ polarization at the pinning boundary and that **(d)** the $P_{[\bar{1}\bar{1}\bar{1}]}$ domain remains at the interface.

The persistence of non-ferroelastic 180° switched regions at the interface is problematic for magnetoelectric applications since this does not correspond to a change in the polarization axis and therefore the antiferromagnetic ordering. Further, the presence of these small interface domains is unlikely to show up in PFM because of their small volume or in X-ray since they are essentially isostructural.

5.3.3 Domain Pinning

The vertical extent of the interfacial domains depends on the voltage history as shown by Fig. 5.12a, however the lateral edges of the interface domains are fixed and found to contain a high density of point defects. HAADF images of two inclined 180° domain walls show are shown in Fig. 5.14 and despite obvious smearing of the B-site Fe position in parts of the images the polarization maps (inset) indicate identical domain structures. In the two domain walls there are at least three defects highlighted in red. The left domain wall has a dark region at the oxygen site suggesting one or more oxygen vacancies. The boxed region highlights a large vertical displacement of adjacent Bi atoms possibly due to an interstitial. The right domain wall contains a heavy element substitution in the Fe site (also shown inset in Fig. 5.12). Both of these 180° domain walls lie on the equilibrium $(0\bar{1}1)$ planes and are neutrally charged, thus their interaction with the point defects is likely not electrostatic but due to local strain fields. It is unknown whether these defects act as nucleation or pinning sites or if they migrated to the domain wall post-switching.

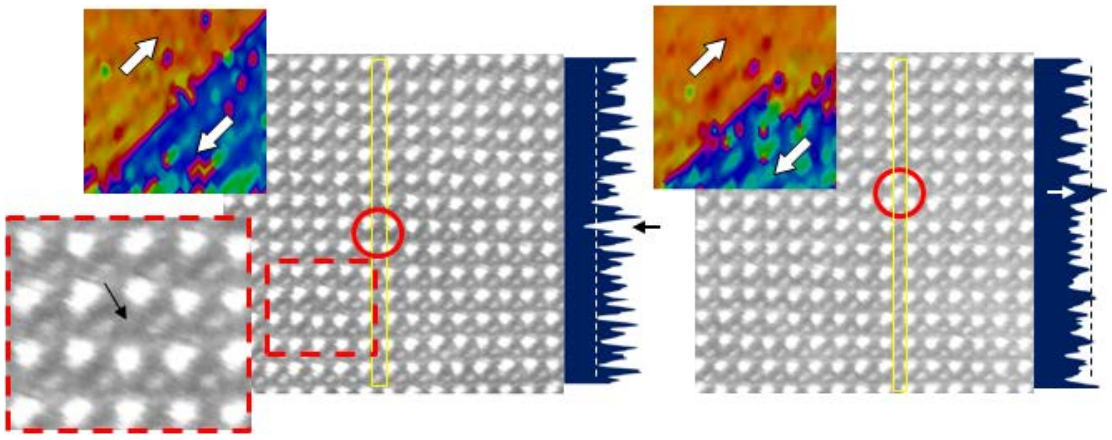

Fig. 5.14 Defects at Interfacial 180° Domain Walls
Two examples of the inclined edges of the interfacial domains which show apparent point defects in the respective HAADF STEM images. At left there is a dark region indicating vacancies or a lighter element substitution in the Fe or O positions. The rectangular region inset highlights a very large vertical displacements of two neighboring Bi atoms which may correspond to an impurities at either the oxygen or interstitial sites along this column (black arrow). At right there is a heavy element at the B-site, most likely a Bi substitution for Fe.

While it is speculative whether the observed defects act as pinning sites for the interface domains, in-situ switching of $BiFeO_3$ shows frequent examples of clear domain wall

pinning. Notably, switching of the primary domain often does not extend the full width between the two electrodes. Despite the high energy negatively charged domain wall that is created from the tail-to-tail alignment of the polarization, the forward propagating domain becomes pinned midway through the film leaving the top layer unswitched such as the switched region in Fig. 5.10a and the left-hand sides of Fig. 5.12b and Fig. 5.13b. This behavior points to pinning by fixed (at least on short time scales) planar defects such as ordered planes of point defects. This is supported by the repeatability of the pinning planes (see Fig. 5.15) but their inhomogeneous distribution throughout the sample.

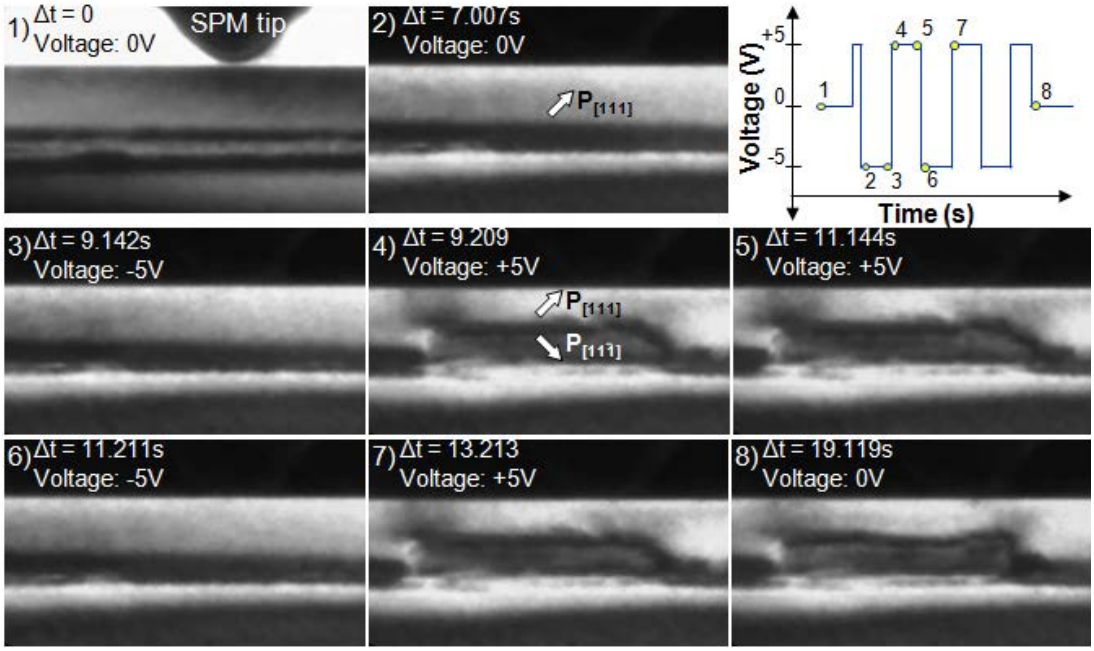

Fig. 5.15 Cyclic Pinning of a Primary Domain in $BiFeO_3$
The $BiFeO_3$ film is subjected to a series of cyclic square-wave switching pulses corresponding to the voltage-time curve shown at the top right. The parallel images from adjacent switching events (3,4 vs 6,7) show identical responses. The position of the switched domain is the same corresponding to a fixed pinning site. The dark field images were formed using g=(400) planes.

No structural defects are visible in the TEM images and thickness maps do not show any significant variation between pinned and fully switched regions which could otherwise account for the pinning (Fig. 5.16).

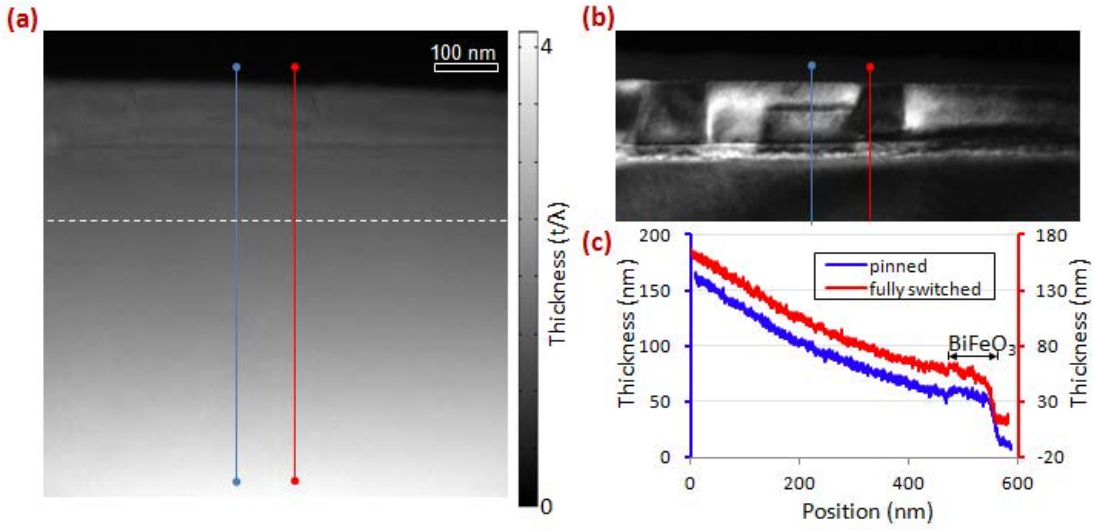

Fig. 5.16 Thickness Map of the Switching Region in $BiFeO_3$
(a) A (t/λ) thickness map of the switched region from Fig. 5.13b – shown again here in **(b)** where t is the thickness along the electron beam and λ is the mean free paths between plasmon scattering events. The thickness map was acquired and calibrated according to section 5.2.2. The result is real-value thickness map from which profiles across the pinned (blue) and unpinned (red) regions are shown in **(c)**. There is no discernable difference in thickness profiles between the two regions.

Surface defects have been reported to pin lateral domain creep[186] so AFM was performed on the prepared surface of a TEM sample. A much thicker 800 nm $BiFeO_3$ film[†] grown on bare $TbScO_3$ was used due to the lower resolution of PFM. An optical image of the cross section sample under study prepared according to section 2.2.1 is shown in Fig. 5.17a. AFM and PFM scans could not be performed at the fragile electron-transparent edge of the sample but were instead performed at the region highlighted. The AFM and PFM images of the $BiFeO_3$ film in this region are shown in Fig. 5.17b and Fig. 5.17c respectively. The presence of the $BiFeO_3$ layer is clear from the oscillating domain structure in the out-of-plane PFM image (Fig. 5.17c) formed in response to the depolarizing fields from the insulating $TbScO_3$ surface. The surface topography in this region does not have any systematic steps along the (001) planes which could account for the observed pinning on these planes (Fig. 5.17b).

[†] Provided by collaboration with Dr. Chang-Beom Eom – *University of Wisconsin - Madison*

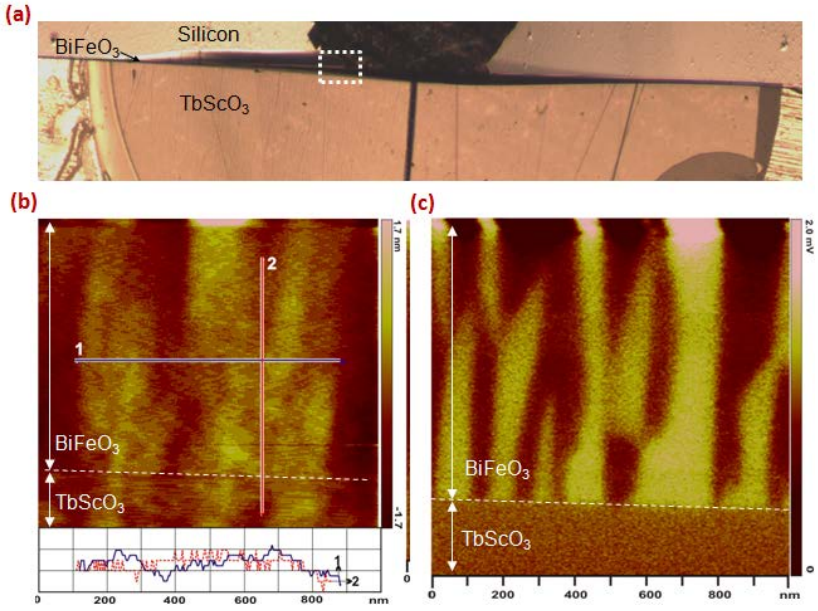

Fig. 5.17 Surface Topography of the $BiFeO_3$ TEM Sample
(a) An optical microscope image of the prepared cross-section TEM sample. The region used for SPM scanning is highlighted (white dashed rectangle-not to scale). **(b)** AFM image of the surface topography and horizontal in-plane (blue) and vertical normal axis (red) line traces show no topological defects to account for pinning. **(c)** out-of-plane PFM image of the same region as (b) clearly demarcates the $BiFeO_3$ film and $TbScO_3$ substrate regions.

Lastly we confirmed that the film is still ferroelectric and that the switched domain is thermodynamically stable beyond the pinning site by overcoming the pinning barrier with the application of larger bias and/or by repositioning the probe. After exclusion of these other possible causes, by process of elimination the likely source of this pinning is from ordered planes of vacancies and/or defect dipoles which are common in perovskite films[188,191], especially those grown by molecular beam epitaxy[181]. These types of defects are difficult to image directly, especially those involving oxygen vacancies or complexes since the scattering cross section is too small for detection in the HAADF images. Given the known influence of oxygen on ferroelectric fatigue[54,60] and the propensity for oxygen vacancies to form ordered planes[192] these results are almost certainly a direct visualization of an oxygen vacancy domain pinning process. Since fatigue remains one of the major shortcomings of long-term ferroelectric device functionality, this provides an excellent platform for future fatigue-failure studies. The fact that this pinning occurs along the normal axis is additionally problematic since, like the 180° interface switching, it prevents full ferroelectric switching to the interface.

Domain wall pinning was also observed by entanglement of domain walls. Such domain wall pile ups are often cited as contributing to switching fatigue[62]. In Fig. 5.18 switching occurs by 180° rotation, nucleating from a region of electrically degraded film directly below the tip (left side of image) and propagating outward (to the right). A preexisting 109◦ domain wall pins the inclined 180◦ domain wall. The two remain together until the opposite switching branch when a 180° domain wall of opposite sense propagates outward and annihilates with the pinned domain wall.

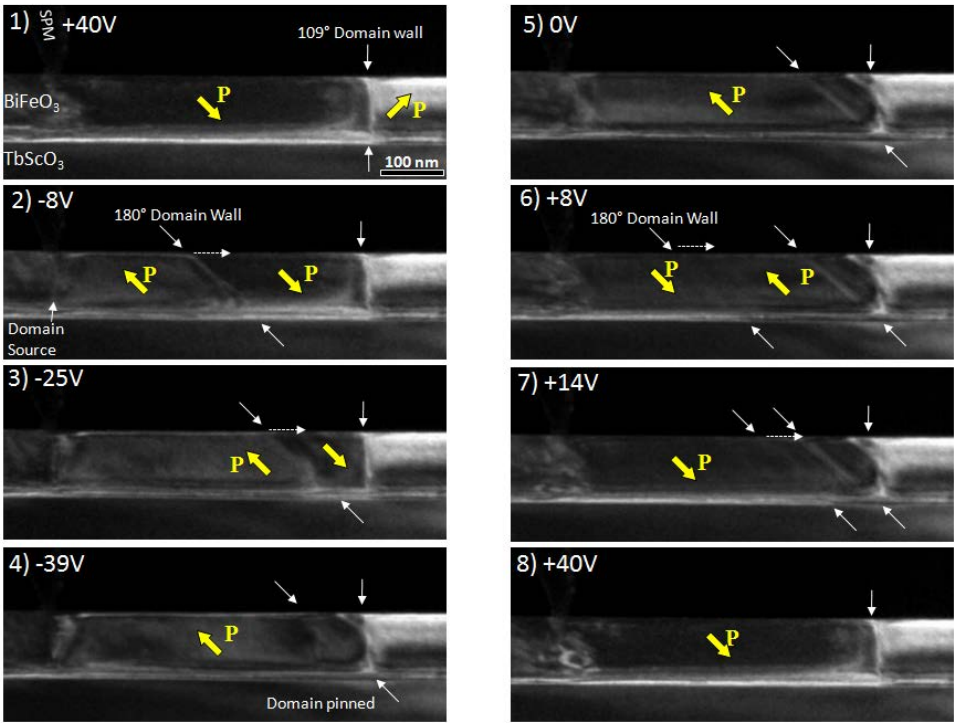

Fig. 5.18 Domain Wall Entanglement
A chronological image series of cyclic switching by a 80Vpp triangle wave depicts pinning of the switched domain on a preexisting 109° domain wall (right side of image). (2) At negative bias a 180° switched domain nucleates from a degraded region of the film and propagates outward. It becomes pinned by a preexisting 109° domain wall (4,5). At positive bias a reverse sense 180° nucleates and propagates outward (6,7) and annihilates with the pinned 180° domain wall (8)

5.3.4 Conclusions

The observed ferroelectric switching, while it may appear by other characterization methods as a conventionally understood 71° single domain switching process, is found to be more complex. In particular, reversible switching at the interfaces is impeded by both near-interface switching and domain pinning which is of particular consequence for

heterostructures dependent on the ferroelectric interface state such as the $BiFeO_3$/ $La_{0.7}Sr_{0.3}MnO_3$ film stack studied here. Film orientations which favor single strain-free switching paths such as (001) tetragonal or (111) rhombohedral ferroelectrics may avoid some of this complexity, but this is not possible for heterostructures such as this one which require ferroelastic switching[87]. We have also found that significant contributions by built-in electric fields lead to a large delocalization of switching from the tip, especially the formation of interfacial domains. The energetics favoring the nucleation and growth of 71° domains despite the presence of favorably oriented yet oddly immobile preexisting 180° domains is unknown. Future studies on the interface structure and its effect on switching or the inclusion of additional electrostatic contributions such as from inhomogeneous space charges, depolarizing fields from finite screening and flexoelectric effects may help elucidate this behavior.

5.4 Switching of Tetragonal $PbZr_{0.2}Ti_{0.8}O_3$

In-situ TEM switching was performed on (001) epitaxial 100 nm films of the commercially prominent ferroelectric $PbZr_{0.2}Ti_{0.8}O_3$. At this composition it adopts a tetragonal structure with six degenerate <100> polarization directions. A weak compressive strain from the $(110)_O$ $DyScO_3$ substrate results in a c-axis oriented film yielding two possible polarization directions, upward to the free surface ($P_{[001]}$) or downward to the substrate ($P_{[00\bar{1}]}$). The SRO electrode partially screens the depolarizing fields but introduces a space charge layer in the form of a Schottky junction with a field along the film normal (E || [001]) promoting an upward polarization ($P_{[001]}$) at this interface. In bulk films, application of a surface probe bias results in a local reversal of the polarization in the film normal axis, aka 180° switching, between upward $P_{[001]}$ and downward $P_{[00\bar{1}]}$ states. This is shown by out-of-plane phase and amplitude PFM images of the edge of a switched region (Fig. 5.19a,b). The 180° switching can be discerned from the large and equal amplitudes of the piezoresponse on either side of the domain wall but a large phase difference.

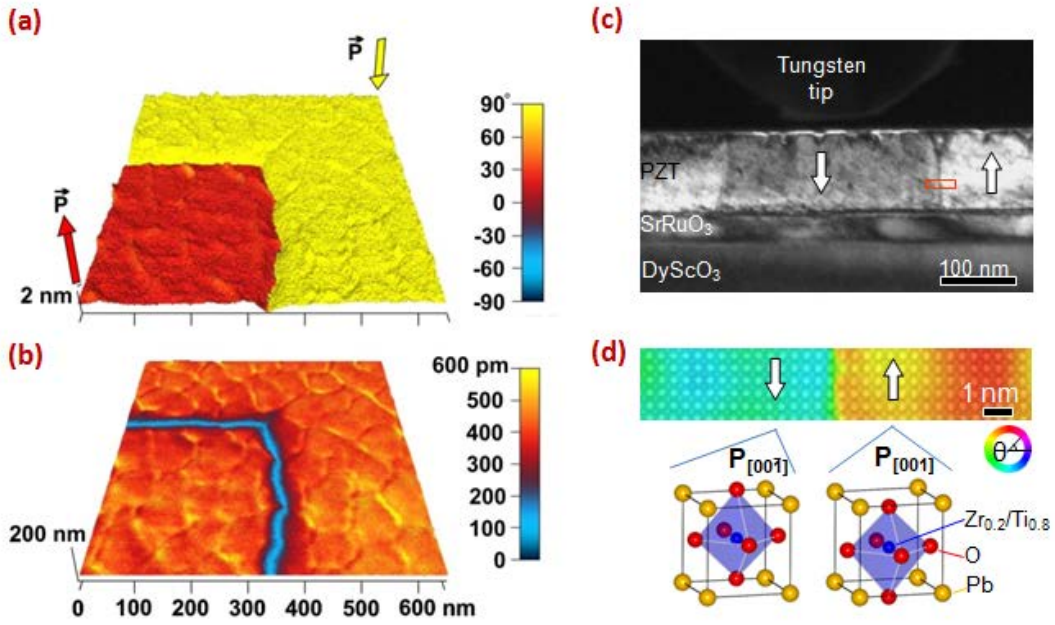

Fig. 5.19 180° Switching by Probe Bias in $PbZr_{0.2}Ti_{0.8}O_3$
PFM images showing 180° domain walls written in lithography mode with a voltage bias of +17.5 V (yellow) and –17.5 V (red). **(a)** The overlay of PFM phase on the amplitude, indicating a 180° rotation. **(b)** PFM amplitude image overlaid on surface topography shows the independence of the domain wall position (blue) from the surface contours. **(c)** Dark field in-situ TEM image showing the geometry of the tungsten tip-PZT-SRO heterostructure. A switched domain corresponding to a 180° rotation of the polarization appears with a darker contrast in this imaging condition with g = (202). The polarization direction is indicated by arrows. **(d)** A sub-Å resolution HAADF image overlaid with its polarization angle, revealing a 180° domain wall.

5.4.1 Domain Switching

Local nanoscale switching carried out in-situ in thin TEM cross sections of the $PbZr_{0.2}Ti_{0.8}O_3$ film is also determined to be 180°. An example dark field image of a switched region is shown in Fig. 5.19c. A polarization mapped section of the right-side domain wall of the switched region is shown in Fig. 5.19c. confirming a 180° domain wall.

The domain formation process along both switching directions was analyzed by real-time TEM imaging of the domain structure under a cyclic 0.1 Hz 18 $V_{peak\text{-}peak}$ triangle wave bias. This region of the PZT film was pre-poled into the $P_{[001]}$ state after which a voltage ramp from 0 to 9V was applied. The "negative" switching branch, i.e. formation of a $P_{[00\bar{1}]}$ domain by application of a negative electric field via a positive tip bias is shown in Fig. 5.20a. The outward progression of the domain area from a nucleation site at the top surface is shown by a time-series of domain outlines accompanied by corresponding

TEM images for the labeled 69 ms, 414 ms, and 1345 ms cases. Onset of the $P_{[00\bar{1}]}$ $P_{[00\bar{1}]}$ domain nucleation occurs at 0.4 V bias and initially proceeds by rapid growth along the applied field direction. Prior to reaching the opposite interface the domain maintains a characteristic “needle” geometry, tapering to a point in order to reduce the area of the charged head-to-head domain wall at the leading edge. After reaching the opposite interface the tapering of the domain walls, which produces small positive surface charge, relaxes to the vertical equilibrium (100) planes as they slowly propagate outward to a final domain width of ~250 nm.

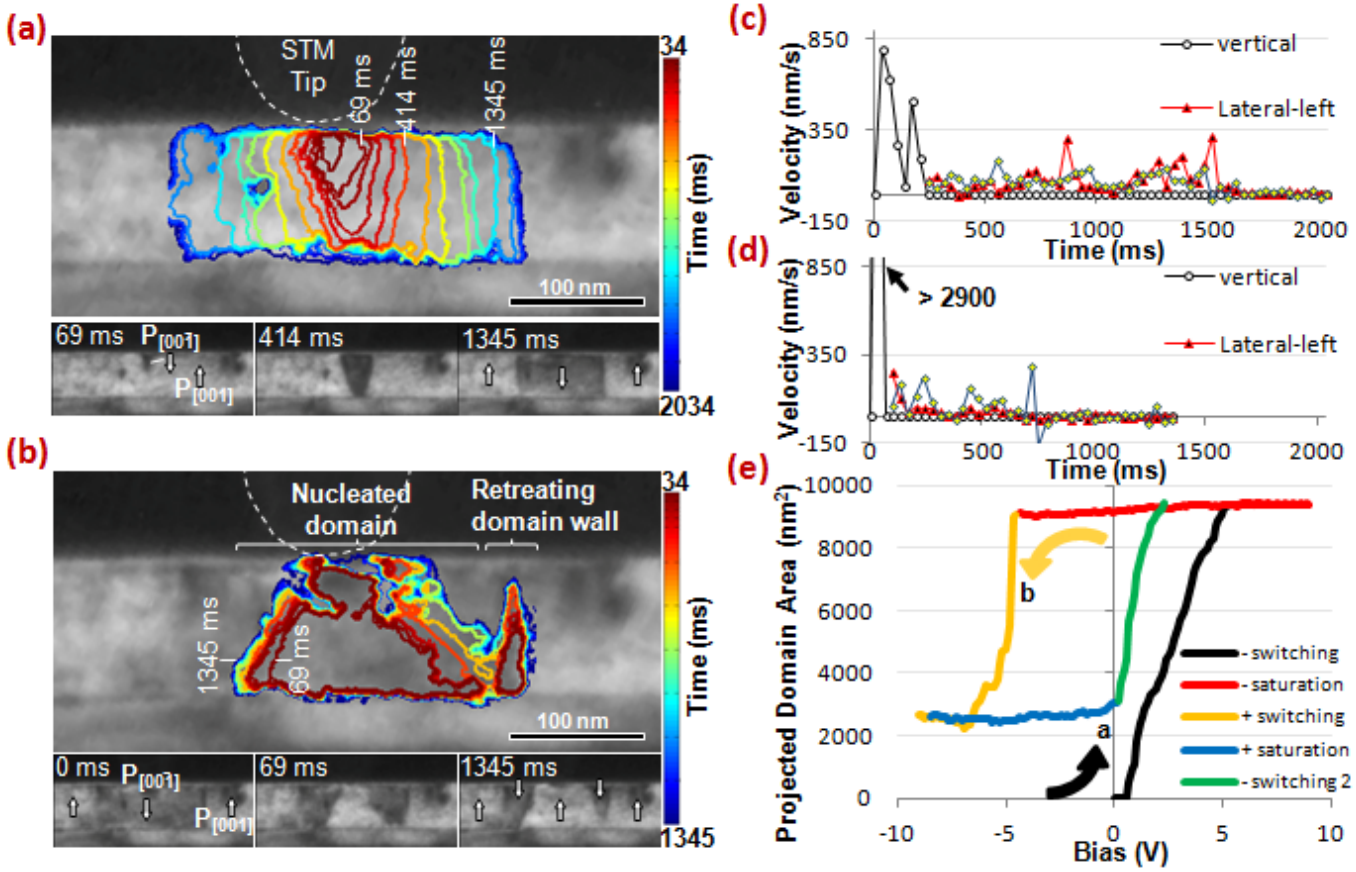

Fig. 5.20 Cyclic Ferroelectric Switching Dynamics in $PbZr_{0.2}Ti_{0.8}O_3$

This region of the PZT film, prepoled to $P_{[001]}$, undergoes cyclic switching using an 18 Vp-p triangle wave. **(a)** The negative and, **(b),** positive switching branches are shown by contour plots of the domain outline versus time with selected corresponding TEM images shown below. During the negative branch a $P_{[00\bar{1}]}$ domain nucleates at the top surface and expands to a final width of ~ 250 nm. On the subsequent positive branch $P_{[001]}$ domains nucleate at the bottom interface and expand across the film in a single timestep. **(c)** Domain wall velocities for the negative switching branch along the vertical and lateral directions. **(d)** Vertical and lateral domain wall velocities for the positive switching branch. **(e)** A ferroelectric hysteresis loop of domain area vs. bias for the switching cycle containing (a) and (b).

For the subsequent "positive" switching branch shown in Fig. 5.20b, where the voltage is ramped from 0 V to -9 V, a $P_{[001]}$ domain is formed within the previous $P_{[00\bar{1}]}$ domain but with very different kinetics than during negative switching. The nucleation of multiple $P_{[001]}$ domains occurs simultaneously at the bottom interface directly below the tip at -4.8 V after which the domains coalesce and expand to almost their full extent within a single 34 ms timestep. In addition to this nucleated domain, there is a retreat of the rightmost edge of the surrounding $P_{[00\bar{1}]}$ domain creating an additional region of $P_{[001]}$ formation labeled on the right side in Fig. 5.20b. Limited lateral domain growth is observed, primarily on the right side, but it does not fully consume the surrounding $P_{[00\bar{1}]}$ domain resulting in incomplete backswitching. The vertical and lateral domain wall velocities, determined by the forward edge and the mid-film domain wall position respectively, are shown for the two switching paths in Fig. 5.20c,d. Vertical switching during the positive branch is a minimum of 3.6 times faster than the negative branch, however this trend is reversed for the lateral creep rates which favor the negative switching branch. These two processes were repeatable during subsequent switching cycles.

The corresponding ferroelectric hysteresis loop for these switching events is shown in Fig. 5.20e determined from the switched domain area (section 5.2.3). There are three obvious asymmetries in the hysteresis loop: First, there is a horizontal shift of –2.2 V, corresponding primarily to a built-in electric field, and second, there is a vertical shift due to incomplete back switching. Third, as expected from the observed switching speeds, there is a large disparity in the slopes of the positive and negative switching branches. The translational offsets of the hysteresis loop are primarily the result of random-field defects which can depend on the sample history[193]. Specifically, a portion of the observed loop translation is attributable to charged surface adsorbates and polar defects[188] which have aligned to the as-grown $P_{[00\bar{1}]}$ state, known as aging. This effect favors the original $P_{[00\bar{1}]}$ orientation, leading to a negative horizontal shift, and is a likely source of the incomplete backswitching.

The primary contribution to the asymmetry in the nucleation site and nucleation bias is the built-in electric fields formed by Schottky junctions at the ferroelectric/electrode (semiconductor/metal) interfaces[186] owing to the differences between the larger work functions of $SrRuO_3$ and tungsten electrodes than the electron affinity of PZT[194,195]. The depletion of holes in p-type PZT near the electrodes (diagram in Fig. 5.21a) produces built-in electric fields (E_{bi}) which reach their maximum at the interfaces (black line in Fig. 5.21b). Given energy barriers for the W/PZT and SRO/PZT junctions of 1.3 V and 0.9 V respectively[190,196,197] and assuming homogenous doping and full carrier depletion this corresponds to a doping concentration in a 100 nm film in excess of ~$5\times10^{19}cm^{-3}$ according to[198]:

$$W_d = \sqrt{\frac{2 \cdot \varepsilon_r \cdot \varepsilon_0 \cdot V_{bi}}{q \cdot e \cdot N_d}} \qquad 5\text{-}6$$

where W_d is the depletion width of a Schottky junction, ε_r is the relative permittivity, ε_0 permittivity of free space, q is dopant charge, e is the elementary charge, and N_d is the dopant concentration. Here the dopant concentration is solved for the reach-through condition or $W_d1 + W_d2$ = 100 nm. While this choice is somewhat arbitrary, uncertainty in the actual built-in voltages, the dopant concentration, and the dopant distribution prevents any sort of exact solution – and full depletion of a 100 nm film is not an unreasonable assumption. In this case the built-in fields are −47.6 MV/m at the W/PZT interface and 39.6 MV/m at the SRO/PZT interface. Under an external field (E_{ext}), which for simplicity we momentarily assume to be homogenous, the total electrical field $E_{total} = E_{bi} + E_{ext}$ results in the largest positive field (favoring $P_{[001]}$) to occur at the PZT/SRO interface and the largest negative field (favoring $P_{[00\bar{1}]}$) at the PZT/W tip, which corresponds exactly with the observed nucleation sites. In reality E_{ext} from the W tip decreases rapidly with distance from the contact point so the curves in Fig. 5.21b will instead appear more as illustrated in Fig. 5.21c. In the case that the brief room temperature W/PZT contact does not reach chemical equilibrium and fully form the predicted Schottky junction, the tip enhanced electric field still explains the single site $P_{[00\bar{1}]}$ domain nucleation at the surface probe contact point.

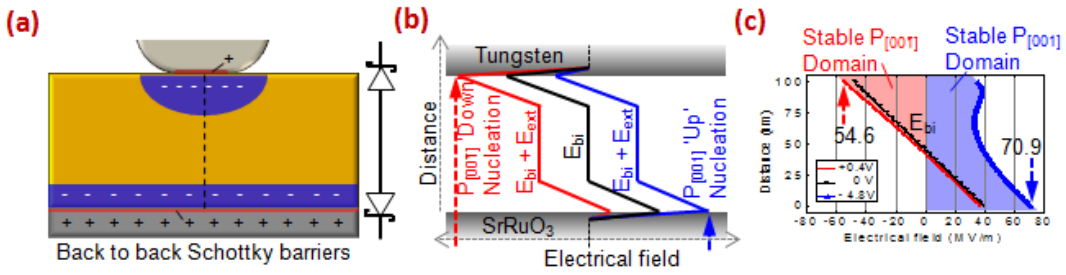

Fig. 5.21 Field Distributions in the W-PZT-$SrRuO_3$ Structure
(a) A schematic of the distribution of space charge corresponding to the formation of two depletion regions and **(b)** the corresponding built-in electric field (black line labeled E_{bi}) formed by the Shottky junctions. Additional external fields E_{ext} add to E_{bi}. The largest positive field and negative field occur on opposite interfaces preferentially nucleating up and down domains respectively. **(c)** The electric-field accounting for the tip-effect on the external electric field. The red curve: bias of +1.3 V and the blue curve: bias of -6.1 V.

The asymmetry in switching speed between the positive and negative branches can also be ascribed to the built-in fields at the interfaces. Maksymovych et. al. have correlated asymmetric piezoresponse hysteresis loops in ferroelectric $BiFeO_3$ films to random-field defects, including built-in junction potentials[199]. Notably, they show that random-field defect induced reduction in nucleation bias also corresponds to a decrease in the switching speed. This can be intuitively explained in the context of the slow switching observed here during the negative branch whose total electric field resembles the red curve in Fig. 5.21c. At the time of nucleation, the electric field exceeds the coercive field only at the interface but rapidly decreases with depth, crossing zero mid film below which the domain is not thermodynamically favored. The domain wall velocity is dependent on the applied electric field, so its velocity can be expected to decrease quickly after nucleation, which is born out in a vertical domain wall velocity graph in Fig. 5.20c. The forward propagation of the domain is momentarily halted between the 3rd and 4th timesteps possibly a result of collision with the zero field crossover. The positive branch, in contrast, has an electric field profile shown by the blue curve in Fig. 5.21c. At the time of nucleation the domain is thermodynamically stable through the entire film thickness so switching is rapid.

5.4.2 Domain pinning

The role of single defects can be explored in this cyclic switching data by making use of the presence of an interior segment of a threading dislocation off center to the tip contact

(see inset in Fig. 5.22a). The lateral expansion of both the $P_{[00\bar{1}]}$ $P_{[00\bar{1}]}$ and $P_{[001]}$ domains in the previously discussed switching branches interact with this dislocation during their respective switching cycles. A HAADF STEM image of the threading dislocation in Fig. 5.22b shows the distorted region which is bounded by two misfit dislocations with the Burgers vectors of <100>a. Fig. 5.22c shows the Fourier-filtered image restricted to information from the (*h*00) reflections with the dislocation cores labeled. They are shown magnified in Fig. 5.22d (top) and Fig. 5.22e (bottom). The influence of this defect on the domain wall can be observed by comparing the lateral domain wall velocities of the left and right domain walls during the negative switching branch (Fig. 5.20c and Fig. 5.22a). When the left domain wall nears the dislocation there is a sudden spike in the domain wall velocity to 300 nm/s as it jumps toward the defect position, manifested as a bright red band in the velocity map in Fig. 5.22a and as a sharp peak in the inset lateral velocity vs. time graph. There is no corresponding spike mirrored on the right edge of the expanding domain, ruling out a change in bias or surface contact. For 233 ms after the spike, the domain wall velocity lies in a trough, never exceeding 50 nm/s, which is manifested as a dark band left of the dislocation. This initial attraction towards and resistance past the dislocation loop indicates a weak pinning of the 180° domain wall to the defect. The regions of compressive and tensile stress are mirrored by the pair of dislocations and cancel when averaged along the domain wall plane ruling out significant net piezoelectric or flexoelectric effects. The vertical 180° domain wall itself is neither ferroelastic nor charged, precluding strong elastic or electrostatic interactions with the dislocation. This suggests that the pinning is the result of an energy reduction by having coincident regions of disorder.

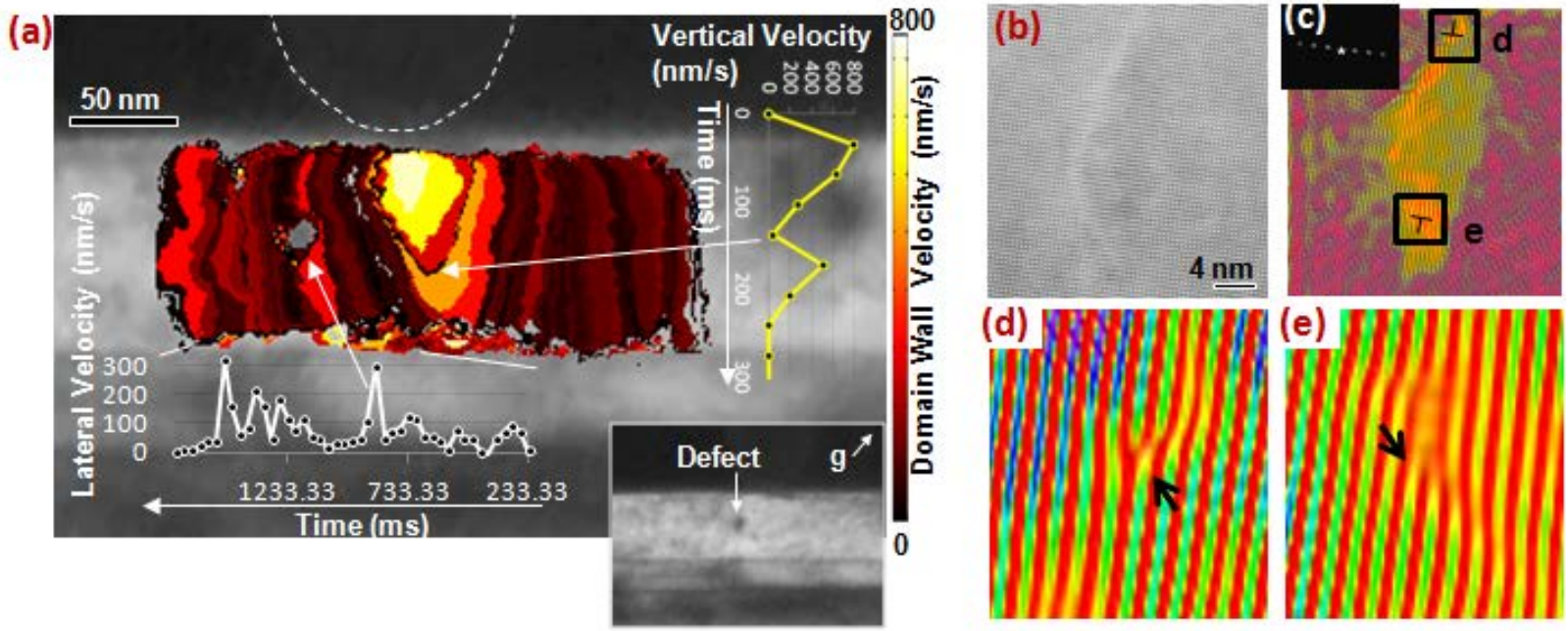

Fig. 5.22 Domain Wall Velocities and Defect Pinning
(a) A contour map of the domain outline at each time step with the color corresponding to the domain wall velocity. Line profiles for the initial vertical velocity and lateral velocity versus time of the left domain wall are overlaid. In both cases a pinning event is highlighted by a white arrow. **(b)** A HAADF image of a defect (labeled in the inset in a) corresponding to the pinned region of the lateral domain wall. **(c)** The same image filtered in Fourier space (see inset) by including only the (200) lattice planes. The labeled <100>*a* dislocation cores are magnified in **(d)** and **(e)**.

Defect pinning is further demonstrated by the positive branch of the switching cycle. The left edge of the backswitched $P_{[001]}$ domain is consistently coincident with the dislocation (see Fig. 5.20b). This pinning manifests in a clear disparity between the lateral velocities (see Fig. 5.20d) and the degree of switching reversal of the left (pinned) and right domain walls. The strength of the pinning is potentially larger during this positive branch since the domain walls are heavily inclined, causing them to be positively charged due to head-to-head polarization vectors normal to the domain wall. This allows for additional electrostatic interactions with ionized dopants or polar defects that may have diffused to the dislocation core. While 180° switching is typical of c-oriented tetragonal ferroelectric materials, stronger defect pinning through elastic interactions would be expected from ferroelastic switching paths such as 90° switching in a tensile strained film or from 71° or 109° switching in a rhombohedral ferroelectric. Despite the proximity of the dislocation to the tip, nucleation and growth kinetics appear to be dominated by the respective interfaces. Especially on the negative branch, the presence of a defect on one side of the domain does not appear to produce a significant lateral domain asymmetry. The large regional variations observed in switching kinetics are therefore likely due to interface effects, either from surface defects modifying the local nucleation energy or heterogeneous screening and/or doping modifying the local built-in fields.

5.4.3 Domain Size Effect & Retention Failure

During the positive switching cycle in section 5.4.1 the 180° $P_{[001]}\|P_{[00\bar{1}]}$ domain walls are significantly inclined from the equilibrium (010) planes forming trapezoidal domains (Fig. 5.20b). This orientation is metastable and relaxes back to the (010) planes after removal of the bias. This section will show that the instability of the switched domain wall can lead to backswitching when the domain width is too small. This is a new mode of retention failure which is generally ascribed to a thermodynamic instability of the switched domain itself. Such behavior is important for high density memory applications since it would impose a lateral size limitation on a stable memory bit. The results in this section suggest that even thermodynamically favored domain orientations are still subject to retention loss, which must be mitigated by overcoming this critical domain size.

A time series of a $P_{[001]}$ domain (light) formation and subsequent backswitching from an initial $P_{[00\bar{1}]}$ region (dark) under a positive-field is shown in Fig. 5.23a-d. The images correspond to the negative voltage cycle of a 0.1 Hz, 18 $V_{peak\text{-}to\text{-}peak}$ triangular wave. The corresponding hysteresis loop is shown in Fig. 5.23e determined by the domain volume (section 5.2.3). Formation of a $P_{[001]}$ domain occurred at –6.6 V during the initial 0 V to –9 V ramp and remained stable until ~–5.5 V of the returning –9V to 0V ramp (Fig. 5.23b). Further reduction in the voltage resulted in the rotation of the domain wall towards the equilibrium (010) plane as shown in Fig. 5.23c. This leads to the annihilation of the two opposing domain walls and the complete backswitching of the $P_{[001]}$ domain (Fig. 5.23d).

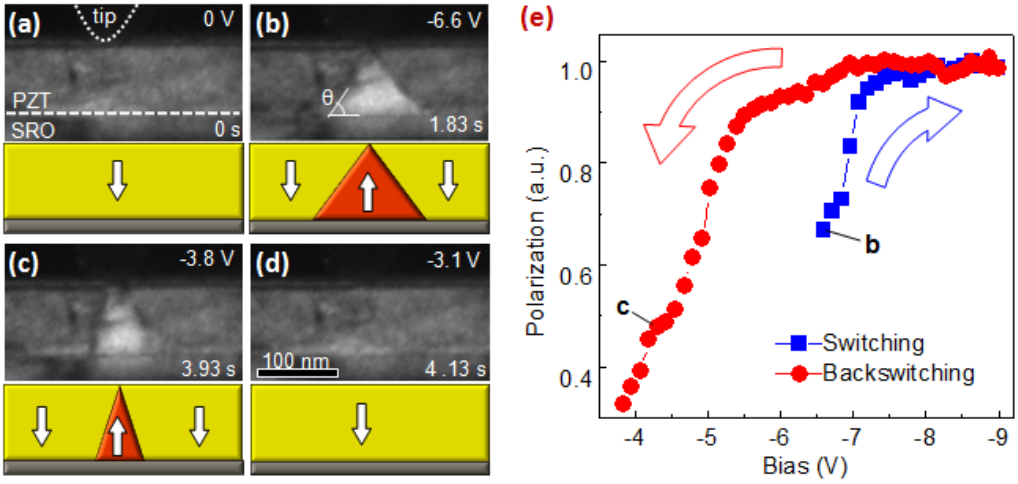

Fig. 5.23 Polarization Retention Loss in a Small Switched Domain
Continuous image sequence of domain evolution in PZT film under linear 0- (–9) -0 V voltage ramps. The time elapsed (in seconds) and bias (in volts) are marked in the figures. **(a)** The initial domain was polarized downward ($P_{[00\bar{1}]}$). **(b)** An upward polarized domain ($P_{[001]}$) has formed at a bias –6.6 V with a triangular shape. With the decrease in voltage, this domain **(c)** shrinks by the rotation of the inclined domain walls to their vertical equilibrium positions and **(d)** finally switches back completely. **(e)** The polarization hysteresis loop calculated by the projected domain area of the $P_{[001]}$ domain as a function of the applied bias.

The formation of a $P_{[001]}$ domain can be stabilized by an increase in the domain size using a larger magnitude and/or longer duration of applied voltages. A time series of the domain structure from the same region of film under longer duration switching is shown in Fig. 5.24. The initial domain structure is identical (Fig. 5.24b). However, the longer

switching time allows for slow lateral expansion of the $P_{[001]}$ domain (Fig. 5.24c-d). Upon removal of the applied voltage the relaxation of the domain walls no longer brings them into contact (Fig. 5.24e), but rather results in only a reduction in domain size as the domain walls acquire typical equilibrium vertical 180° domain orientations (Fig. 5.24f).

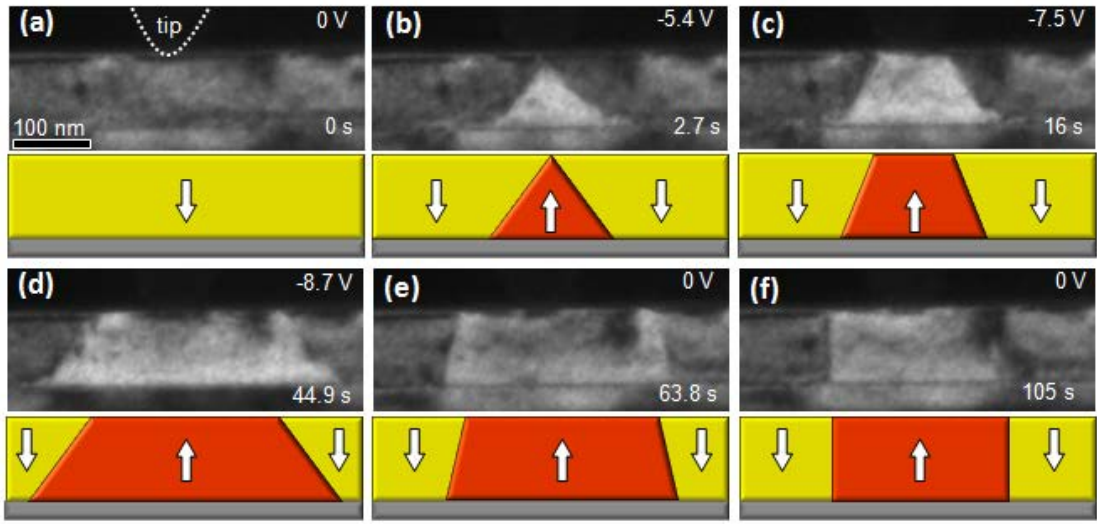

Fig. 5.24 Partial Retention Loss in a Large Switched Domain
(a) Original polar state is downward. **(b)** A triangular $P_{[001]}$ domain is created at –5.4 V bias with inclined domain walls. **(c-d)** With increase of the amplitude and duration of the voltage, the domain laterally expands into a trapezoidal shape. **(e)** The inclined domain walls relax after removal of the bias reducing the switched area and forming **(f)** a rectangular stable domain.

According to first-principles calculations the 180° domain walls in PZT along the low energy {100} planes have energy densities of about 130 mJ/m^2 [43]. However, the highly inclined orientations formed under applied electric field, observed in Fig. 5.23 and Fig. 5.24, results in positive bound charges from the head-to-head orientation of the polarization vectors normal to the domain wall plane (Fig. 4a). Given the incline θ=55° from Fig. 5.23b, the bound charge density from the termination of each of the polarization directions at the domain wall ($\cos\theta\ P_S$) is $0.57P_S$, where P_S is the spontaneous polarization. This gives a total charge density of $1.14P_S$ which exceeds even the surface charge density of the film (P_S). Given an approximate value of P_S=70μC/cm^2 [82,83], this corresponds to a charge density of 80μC/cm^2 or an equivalent density of $5.0 \cdot 10^{14}$cm^{-2} elementary charges. This charge makes the orientation of the domain walls metastable, leading to spontaneous relaxation to {100} planes after the bias is

removed and a shrinking of the switched domain area. For small domains where the apex of these two walls meet to form a triangle shaped domain, as in Fig. 5.25a, the backswitching leads to a complete reversal of polarization within a few seconds. Larger trapezoidal domains (Fig. 5.25b) suffer the same immediate loss in domain volume from the domain wall reorientation, but still retain a rectangular switched domain (Fig. 5.25c). These domains still remain stable after four months (10^7 seconds), indicating thermodynamic stability.

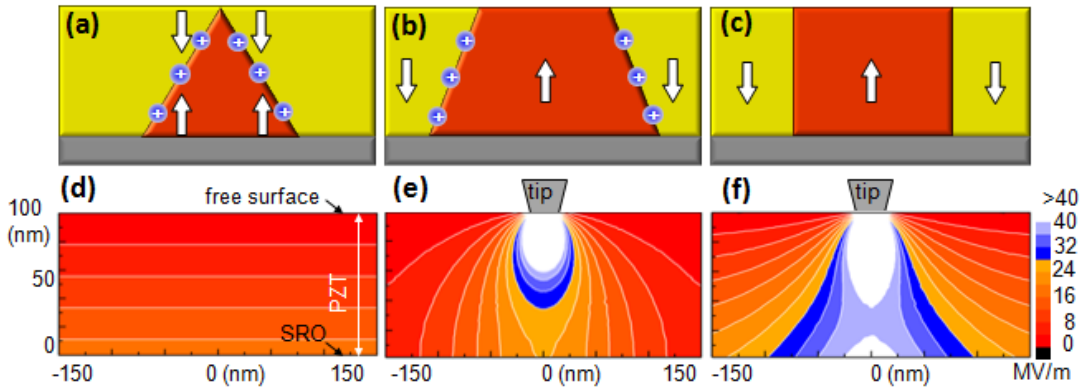

Fig. 5.25 Domain Shape and Electric Field Distribution
Inclined domain walls in **(a)** triangular and **(b)** trapezoidal domains are positively charged due to head-to-head polarization arrangements. **(c)** At zero bias stable domains are rectangular with uncharged vertical domain walls. **(d)** Equipotential contour plot showing the distribution of the built-in electric field (E_{bi}) in a fully depleted PZT film resulting from a Schottky barrier between PZT and $SrRuO_3$. E_{bi} decreases linearly from its maximum value (~18 MV/m) at the interface toward zero at the top surface. **(e)** Equipotential contour plot of the vertical component of the external electric field (E_{ext}) in PZT calculated with a tip contact width of 10 nm and voltage –6 V. **(f)** The combination of these electric fields results in the equipotential contour plot with tapered shapes, such as the highlighted blue contour.

The driving force for adopting metastable domain orientations can be understood from the electric field distribution within the PZT film. The two primary contributions are the Schottky junction at the PZT/SRO interface (Fig. 5.25d) and the external field applied between the surface probe and SRO electrode (Fig. 5.25e). The former arises from the larger work function of SRO (4.9 eV) in comparison with the electron affinity of PZT (3.5 eV)[196,197]. The resulting electric field is normal to the interface and increases linearly with depth, reaching its maximum value ~18 MV/m at the PZT/SRO interface[194] as shown in the contour plot Fig. 5.25d, derived assuming homogenous doping and a depletion width equal to the film height. In contrast, the external applied field is concentrated at the top near the film surface due to the high curvature of the tip. The

inhomogeneous vertical electric field distribution is shown in Fig. 5.25e for a –6V bias and 10nm tip contact area. The combination of these two fields produces the distribution of the total field shown in Fig. 5.25f. The equipotential lines in this contour map show a triangular shape for moderate field strengths (Fig. 5.25f). Since the domain nucleation and domain wall motion depend on the total electric field (see equations 1-2 and 1-3), new domains can be expected to nucleate from one of the two maximum field regions (white) and expand quickly through the high field regions (blue), creating a triangle domain with inclined domain walls which may become kinetically frozen as it expands to regions where the field becomes small. Lateral growth of the domain away from the tip would be particularly slow at the top surface where the applied field is almost entirely in-plane.

Although the applied electric field and the Schottky junction between PZT and SRO can account for a tapered domain shape, other possible built-in fields may be present and destabilize the $P_{[001]}$ domain near the free surface. These fields may result from a Schottky junction between the tungsten tip and PZT[190,196] or from the possible diffusion of charged defects and adsorption of charged species aligned to the original $P_{[00\bar{1}]}$ orientation. The presence of surface states and the short contact of the tungsten tip to the PZT film at room temperature which is unlikely to have reached electrochemical equilibrium make the W/PZT Schottky field difficult to estimate. The built-in field at this junction has the potential to be slightly larger than at the PZT/SRO interface but opposite in direction, reducing the applied field at the tip contact point. The contribution of the alignment of defect dipoles to the original$P_{[00\bar{1}]}$ polarization, an aging process common to ferroelectric oxides, if present must be weak enough or rapidly reversed so that the $P_{[001]}$ orientation is thermodynamically stable as evidenced by the long term retention of all but the smallest domains.

Given the positive field at the PZT/SRO Schottky junction and the lack of strain in 180° switching, the $P_{[001]}$ domain may not only be degenerate but thermodynamically favored in the film at zero bias. In such a case the backswitching of small domains can be solely attributed to the relaxation of their high energy domain walls. Practically this imposes a

critical size criterion on the formation of stable switched domains, similar to the critical size for the nucleation of domains. This also reveals that for a ferroelectric thin film in an inhomogeneous field lateral domain wall creep does not take place by the stepwise movement of equilibrium domain walls, as it is typically modeled[47]. The propagation of charged, rather than neutral domain walls may significantly alter the kinetics of the switching since the domain wall itself will electrostatically interact with charged defects and built-in fields. The dynamic variation of the domain wall along the film depth is an important consideration not only for ferroelectric storage, but for surface probe microscopy which utilizes this same geometry.

5.5 Conclusions

In this chapter, the real-time ferroelectric switching in thin films of two of the most prominent ferroelectric materials, $BiFeO_3$ and $PbZr_{0.2}Ti_{0.8}O_3$, was measured at the nanoscale using in-situ TEM. From the analysis of these two, the switching dynamics in both rhombohedral and tetragonal systems was studied. In both cases, nucleation sites were dominated by the built-in fields created by Schottky junctions at the electrode interfaces with alternate signs between the n-type $BiFeO_3$ and the p-type $PbZr_{0.2}Ti_{0.8}O_3$ cases. Switching in the tetragonal $PbZr_{0.2}Ti_{0.}8O_3$ films occurred by the 180° rotation following typical needle-domain growth processes. The rhombohedral $BiFeO_3$ system was the more complicated and exhibited multiple switching paths, specifically a primary 71° switching in the bulk of the film and a 180° switching near the interface. Domain wall pinning was systemic in the $BiFeO_3$ film, occurring primarily along (001) oxygen vacancy planar defects, but weak pinning was also observed from dislocations in the $PbZr_{0.2}Ti_{0.}8O_3$ film. Under bias the switched domain walls adopt metastable orientations and positions and some backswitching was observed in both materials when the bias was removed. This was most pronounced in $PbZr_{0.2}Ti_{0.}8O_3$ and actually led to complete retention loss in very small switched domains.

Chapter 6

6 Summary and Future Work

6.1 Summary

In this work I have presented a detailed microscopic analysis of the deterministic role of interfaces in both the static equilibrium and dynamic ferroelectric switching properties of two prototypical ferroelectric thin films: $BiFeO_3$ and $PbZr_{0.2}Ti_{0.8}O_3$. Both materials were grown in low-strain systems to isolate the influence of electrostatic boundary conditions. From the self-compensating domain structures observed by TEM, the free surface and electrode interface were found to be charge compensated while the $\{Re\}ScO_3$ substrate interface was insulating. Most notably, the high electrostatic energy at the insulating interface promoted the formation of nanoscale flux closure domains in $BiFeO_3$ analogous to those observed in larger scales in ferromagnetic materials. The crystal, chemical, and polar structure of the $BiFeO_3$ films, domain walls and interfaces was analyzed using Sub-Angstrom TEM in combination with custom image processing. This nanoscale analysis, especially used as an input for later first principles studies, allows us to understand the mechanisms behind practical phenomenon such as non-polar interface layers, ferroelectric degeneracy and functional domain wall properties.

Ferroelectric switching of rhombohedral $BiFeO_3$ and tetragonal $PbZr_{0.2}Ti_{0.8}O_3$ ferroelectric thin films was performed in situ. In both systems the nucleation site and the switching process were dictated by the built in electric fields formed by the carrier depletion of the ferroelectric/metallic junction(s). In addition to the interfaces, other defects were directly observed to play an active role as pinning sites including single point defects, ordered vacancy planes, dislocations, and pre-existing domain walls. This provides a first ever look at these switching and pinning processes within the confined thin film axis. There are several notable deviations from the theoretical models including thermodynamically limited switching, independent interface switching, and depletion

assisted interface nucleation. These behaviors have significant import on macroscale properties such as an incorrect switching transient in electrical measurements, partial failure of magnetoelectric coupling at the $BiFeO_3$ / $La_{0.7}Sr_{0.3}MnO_3$ interface, and delocalization of nucleation sites in surface probe measurements, respectively. These experiments demonstrate integrated SPM-TEM as an ideal platform to study the nanoscale properties which control the macroscale behavior of ferroelectric materials.

6.2 Future Directions

As a pioneering study into nanoscale ferroelectric switching there is a monumental amount of design space and analysis that is yet to be studied. Obvious low-hanging fruit is the analysis of other ferroelectric materials systems, growth orientations, and switching directions which will exhibit different behavior. Modifications to these two materials can provide additional insight into the switching and pinning: for example doping of the ferroelectric films to change the majority carrier type / concentration or growth under different oxygen partial pressures. Many of the behaviors reported here are qualitative or semi-quantitative due to uncertainty of the inhomogeneous electric field. The use of uniform fields or characterization of the field distribution using electron holography would allow for the domain nucleation and domain motion activation fields to be determined and lateral preferential nucleation sites to be identified.

There is a great deal of additional characterization which can be done in conjunction with the in situ TEM switching, such as the aforementioned electron holography. The near-edge EELS structure would help to characterize the electronic structure and the composition at the nucleation and domain wall pinning sites. Lorentz microscopy could be used to simultaneously image the ferromagnetic domains in materials such as $La_{0.7}Sr_{0.3}MnO_3$ allowing the coupling or lack thereof to an adjacent $BiFeO_3$ layer to be detected directly. Macroscale and mesoscale measurements such as electrical P-E loop measurements, cathodoluminescence, and SS-PFM would provide detail about the electrical properties, defect states, and switching behavior over a much larger sample size. Ultimately, direct comparisons between the in situ TEM and these other techniques would help to bridge our understanding of the nanoscale control of ferroelectric behavior.

Bibliography

1 Imada, M., Fujimori, A. & Tokura, Y. Metal-insulator transitions. *Rev. Mod. Phys.* **70**, 1039-1263 (1998).

2 Bardeen, J., Cooper, L. N. & Schrieffer, J. R. Theory of superconductivity. **108**, 1175-1204 (1957).

3 Hill, N. A. Why are there so few magnetic ferroelectrics? *J. Phys. Chem. B* **104**, 6694-6709 (2000).

4 Mathews, S., Ramesh, R., Venkatesan, T. & Benedetto, J. Ferroelectric field effect transistor based on epitaxial perovskite heterostructures. *Science* **276**, 238-240 (1997).

5 Haeni, J. H. *et al.* Room-temperature ferroelectricity in strained SrTiO3. *Nature* **430**, 758-761 (2004).

6 Choi, K. J. *et al.* Enhancement of ferroelectricity in strained BaTiO(3) thin films. *Science* **306**, 1005-1009 (2004).

7 Beach, R. S. *et al.* Enhanced Curie temperatures and magnetoelastic domains in Dy/Lu superlattices and films. *Phys. Rev. Lett.* **70**, 3502-3505 (1993).

8 Gan, Q., Rao, R. A., Eom, C. B., Garrett, J. L. & Lee, M. Direct measurement of strain effects on magnetic and electrical properties of epitaxial SrRuO3 thin films. *Appl. Phys. Lett.* **72**, 978-980 (1998).

9 Sato, H. & Naito, M. Increase in the superconducting transition temperature by anisotropic strain effect in (001)La1.85Sr0.15CuO4 thin films on LaSrAlO4 substrates. *Physica C* **274**, 221-226 (1997).

10 Bozovic, I., Logvenov, G., Belca, I., Narimbetov, B. & Sveklo, I. Epitaxial strain and superconductivity in La2-xSrxCuO4 thin films. *Phys. Rev. Lett.* **89**, 107001 (2002).

11 Ohtomo, A. & Hwang, H. Y. A high-mobility electron gas at the LaAlO3/SrTiO3 heterointerface. *Nature* **427**, 423-426 (2004).

12 Ohtomo, A., Muller, D. A., Grazul, J. L. & Hwang, H. Y. Artificial charge-modulation in atomic-scale perovskite titanate superlattices. *Nature* **419**, 378-380 (2002).

13 Seidel, J. *et al.* Conduction at domain walls in oxide multiferroics. *Nat. Mater.* **8**, 229-234 (2009).

14 Privratska, J. & Janovec, V. Pyromagnetic domain walls connecting antiferromagnetic non-ferroelastic magnetoelectric domains. *Ferroelectrics* **204**, 321-331 (1997).

15 Scott, J. F. & De Araujo, C. A. P. Ferroelectric memories. *Science* **246**, 1400-1405 (1989).

[16] Auciello, O., Scott, J. F. & Ramesh, R. The physics of ferroelectric memories. *Phys. Today* **51**, 22-27 (1998).
[17] Scott, J. F. Data storage - Multiferroic memories. *Nat. Mater.* **6**, 256-257 (2007).
[18] Ramesh, R. & Spaldin, N. A. Multiferroics: progress and prospects in thin films. *Nat. Mater.* **6**, 21-29 (2007).
[19] Scott, J. F. Applications of modern ferroelectrics. *Science* **315**, 954-959 (2007).
[20] Garcia, V. *et al.* Giant tunnel electroresistance for non-destructive readout of ferroelectric states. *Nature* **460**, 81-84 (2009).
[21] Garcia, V. *et al.* Ferroelectric control of spin polarization. *Science* **327**, 1106-1110 (2010).
[22] Tsymbal, E. Y. & Kohlstedt, H. Applied physics - Tunneling across a ferroelectric. *Science* **313**, 181-183 (2006).
[23] Maksymovych, P. *et al.* Polarization control of electron tunneling into ferroelectric surfaces. *Science* **324**, 1421-1425 (2009).
[24] Li, D. B. *et al.* Direct in situ determination of the polarization dependence of physisorption on ferroelectric surfaces. *Nat. Mater.* **7**, 473-477 (2008).
[25] Aizu, K. Possible species of ferroelastic crystals and of simultaneously ferroelectric and ferroelastic crystals. *J. Phys. Soc. Jpn.* **27**, 387-396 (1969).
[26] Kubel, F. & Schmid, H. Structure of a ferroelectric and ferroelastic monodomain crystal of the perovskite BiFeO3. *Acta Crystallogr. Sect. B-Struct. Commun.* **46**, 698-702 (1990).
[27] Zheng, H. *et al.* Multiferroic BaTiO3-CoFe2O4 nanostructures. *Science* **303**, 661-663 (2004).
[28] Chu, Y. H. *et al.* Electric-field control of local ferromagnetism using a magnetoelectric multiferroic. *Nat. Mater.* **7**, 478-482 (2008).
[29] Laukhin, V. *et al.* Electric-field control of exchange bias in multiferroic epitaxial heterostructures. *Phys. Rev. Lett.* **97**, 4 (2006).
[30] Wu, S. M. *et al.* Reversible electric control of exchange bias in a multiferroic field-effect device. *Nat. Mater.* **9**, 756-761 (2010).
[31] Dho, J. H., Qi, X. D., Kim, H., MacManus-Driscoll, J. L. & Blamire, M. G. Large electric polarization and exchange bias in multiferroic BiFeO3. *Adv. Mater.* **18**, 1445-1448 (2006).
[32] Kim, S. K. *et al.* Voltage control of a magnetization easy axis in piezoelectric/ferromagnetic hybrid films. *J. Magn. Magn. Mater.* **267**, 127-132 (2003).
[33] Schroder, K. Stress operated random-access, high-speed magnetic memory. *J. Appl. Phys.* **53**, 2759-2761 (1982).
[34] Valasek, J. Piezo-electric and allied phenomena in Rochelle salt. *Phys. Rev.* **17**, 475-481 (1921).
[35] Nenert, G. Phenomenological Landau analysis of predicted magnetoelectric fluorides: KMnFeF(6) and Ba(2)Ni(7)F(18). *J. Phys.-Condes. Matter* **20**, 335229 (2008).
[36] Nenert, G. & Palstra, T. T. M. Prediction for new magnetoelectric fluorides. *J. Phys.-Condes. Matter* **19**, 406213 (2007).
[37] Cohen, R. E. Origin of ferroelectricity in perovsite oxides. *Nature* **358**, 136-138 (1992).

[38] Neaton, J. B., Ederer, C., Waghmare, U. V., Spaldin, N. A. & Rabe, K. M. First-principles study of spontaneous polarization in multiferroic BiFeO3. *Phys. Rev. B* **71**, 014113 (2005).

[39] Seshadri, R. & Hill, N. A. Visualizing the role of Bi 6s "Lone pairs" in the off-center distortion in ferromagnetic BiMnO(3). *Chem. Mat.* **13**, 2892-2899 (2001).

[40] Spaldin, N. A. & Fiebig, M. The renaissance of magnetoelectric multiferroics. *Science* **309**, 391-392 (2005).

[41] Gajek, M. *et al.* Tunnel junctions with multiferroic barriers. *Nat. Mater.* **6**, 296-302 (2007).

[42] Nan, C. W., Bichurin, M. I., Dong, S. X., Viehland, D. & Srinivasan, G. Multiferroic magnetoelectric composites: Historical perspective, status, and future directions. *J. Appl. Phys.* **103**, 031101 (2008).

[43] Meyer, B. & Vanderbilt, D. Ab initio study of ferroelectric domain walls in $PbTiO_3$. **65**, 104111 (2002).

[44] Lubk, A., Gemming, S. & Spaldin, N. A. First-principles study of ferroelectric domain walls in multiferroic bismuth ferrite. *Phys. Rev. B* **80**, 104110 (2009).

[45] Landauer, R. Electrostatic considerations in BaTiO3 domain formation during polarization reversal. *J. Appl. Phys.* **28**, 227-234 (1957).

[46] Merz, W. J. Domain formation and domain wall motions in ferroelectric BaTiO3 single crystals. *Phys. Rev.* **95**, 690-698 (1954).

[47] Shin, Y. H., Grinberg, I., Chen, I. W. & Rappe, A. M. Nucleation and growth mechanism of ferroelectric domain-wall motion. *Nature* **449**, 881-887 (2007).

[48] Avrami, M. Kinetics of phase change I - General theory. *J. Chem. Phys.* **7**, 1103-1112 (1939).

[49] Du, X. F. & Chen, I. W. in *Ferroelectric Thin Films Vi* Vol. 493 *Materials Research Society Symposium Proceedings* eds R. E. Treece *et al.*) 311-316 (Materials Research Society, 1998).

[50] Ishibashi, Y. & Takagi, Y. Ferroelectric domain switching. *J. Phys. Soc. Jpn.* **31**, 506-510 (1971).

[51] Gruverman, A. *et al.* Direct studies of domain switching dynamics in thin film ferroelectric capacitors. *Appl. Phys. Lett.* **87**, 082902 (2005).

[52] Pantel, D. *et al.* Switching kinetics in epitaxial BiFeO3 thin films. *J. Appl. Phys.* **107**, 084111 (2010).

[53] Jung, D. J., Dawber, M., Scott, J. F., Sinnamon, L. J. & Gregg, J. M. Switching dynamics in ferroelectric thin films: An experimental survey. *Integr. Ferroelectr.* **48**, 59-68 (2002).

[54] Dawber, M., Rabe, K. M. & Scott, J. F. Physics of thin-film ferroelectric oxides. *Rev. Mod. Phys.* **77**, 1083-1130 (2005).

[55] Lou, X. J. Statistical switching kinetics of ferroelectrics. *J. Phys.-Condes. Matter* **21**, 012217 (2009).

[56] Tagantsev, A. K., Stolichnov, I., Setter, N., Cross, J. S. & Tsukada, M. Non-Kolmogorov-Avrami switching kinetics in ferroelectric thin films. *Phys. Rev. B* **66**, 214109 (2002).

[57] Kim, Y. *et al.* Non-Kolmogorov-Avrami-Ishibashi Switching Dynamics in Nanoscale Ferroelectric Capacitors. *Nano Lett.* **10**, 1266-1270 (2010).

[58] Maksymovych, P. *et al.* Intrinsic nucleation mechanism and disorder effects in polarization switching on ferroelectric surfaces. *Phys. Rev. Lett.* **102**, 017601 (2009).
[59] Scott, J. F. & Pouligny, B. Raman-spectroscopy of sub-micron KNO3 films .2. Fatigue and space-charge effects. *J. Appl. Phys.* **64**, 1547-1551 (1988).
[60] Brazier, M., Mansour, S. & McElfresh, M. Ferroelectric fatigue of Pb(Zr,Ti)O-3 thin films measured in atmospheres of varying oxygen concentration. *Appl. Phys. Lett.* **74**, 4032-4033 (1999).
[61] De Araujo, C. A. P., Cuchiaro, J. D., McMillan, L. D., Scott, M. C. & Scott, J. F. Fatigue-free ferroelectric capacitors with platinum-electrodes. *Nature* **374**, 627-629 (1995).
[62] Baek, S.-H. *et al.* The Nature of Polarization Fatigue in BiFeO3. *Adv. Mater.* ***In Press*** (2011).
[63] Pertsev, N. A. & Koukhar, V. G. Polarization instability in polydomain ferroelectric epitaxial thin films and the formation of heterophase structures. *Phys. Rev. Lett.* **84**, 3722-3725 (2000).
[64] Lohse, O., Grossmann, M., Boettger, U., Bolten, D. & Waser, R. Relaxation mechanism of ferroelectric switching in $Pb(Zr,Ti)O_3$ thin films. *J. Appl. Phys.* **89**, 2332-2336 (2001).
[65] Gruverman, A. & Tanaka, M. Polarization retention in $SrBi_2Ta_2O_9$ thin films investigated at nanoscale. **89**, 1836-1843 (2001).
[66] Ganpule, C. S. *et al.* Polarization relaxation kinetics and 180 degrees domain wall dynamics in ferroelectric thin films. **65**, 014101 (2002).
[67] Guo, H. Y. *et al.* Study of domain stability on $(Pb_{0.76}Ca_{0.24})TiO_3$ thin films using piezoresponse microscopy. **81**, 715-717 (2002).
[68] Kang, B. S. *et al.* Polarization retention in $Pb(Zr_{0.4}Ti_{0.6})O_3$ capacitors with IrO_2 top electrodes. **84**, 3127-3129 (2004).
[69] Kim, D. J. *et al.* Polarization relaxation induced by a depolarization field in ultrathin ferroelectric $BaTiO_3$ capacitors. **95**, 237602 (2005).
[70] Lou, X. J., Zhang, M., Redfern, S. A. T. & Scott, J. F. Local phase decomposition as a cause of polarization fatigue in ferroelectric thin films. *Phys. Rev. Lett.* **97**, 177601 (2006).
[71] Jo, J. Y. *et al.* Polarization switching dynamics governed by the thermodynamic nucleation process in ultrathin ferroelectric films. *Phys. Rev. Lett.* **97**, 247602 (2006).
[72] Batra, I. P. & Silverma.Bd. Thermodynamic stability of thin ferroelectric films. *Solid State Commun.* **11**, 291-& (1972).
[73] Mehta, R. R., Silverma.Bd & Jacobs, J. T. Depolarization fields in thin ferroelectric films. *J. Appl. Phys.* **44**, 3379-3385 (1973).
[74] Arlt, G. & Neumann, H. Internal bias in ferroelectric ceramics - origin and time-dependentce. **87**, 109-120 (1988).
[75] Benedetto, J. M., Moore, R. A. & McLean, F. B. Effects of operating-conditions on the fast-decay component of the retained polarization in lead-zirconate-titanate thin-films. *J. Appl. Phys.* **75**, 460-466 (1994).
[76] Junquera, J. & Ghosez, P. Critical thickness for ferroelectricity in perovskite ultrathin films. *Nature* **422**, 506-509 (2003).

[77] Kornev, I., Fu, H. X. & Bellaiche, L. Ultrathin films of ferroelectric solid solutions under a residual depolarizing field. *Phys. Rev. Lett.* **93**, 196104 (2004).
[78] Fong, D. D. *et al.* Ferroelectricity in ultrathin perovskite films. *Science* **304**, 1650-1653 (2004).
[79] Cruz, M. P. *et al.* Strain control of domain-wall stability in epitaxial BiFeO3 (110) films. *Phys. Rev. Lett.* **99**, 217601 (2007).
[80] Baek, S. H. *et al.* Ferroelastic switching for nanoscale non-volatile magnetoelectric devices. *Nat. Mater.* **9**, 309-314 (2010).
[81] Damjanovic, D. Ferroelectric, dielectric and piezoelectric properties of ferroelectric thin films and ceramics. *Rep. Prog. Phys.* **61**, 1267-1324 (1998).
[82] Nagarajan, V. *et al.* Dynamics of ferroelastic domains in ferroelectric thin films. *Nat. Mater.* **2**, 43-47 (2003).
[83] Nagarajan, V. *et al.* Size effects in ultrathin epitaxial ferroelectric heterostructures. *Appl. Phys. Lett.* **84**, 5225-5227 (2004).
[84] Wang, J. *et al.* Epitaxial BiFeO3 multiferroic thin film heterostructures. *Science* **299**, 1719-1722 (2003).
[85] Das, R. R. *et al.* Synthesis and ferroelectric properties of epitaxial BiFeO3 thin films grown by sputtering. *Appl. Phys. Lett.* **88**, 242904 (2006).
[86] Zeches, R. J. *et al.* A Strain-Driven Morphotropic Phase Boundary in BiFeO(3). *Science* **326**, 977-980 (2009).
[87] Zhao, T. *et al.* Electrical control of antiferromagnetic domains in multiferroic BiFeO3 films at room temperature. *Nat. Mater.* **5**, 823-829 (2006).
[88] Urban, K. W. Studying atomic structures by aberration-corrected transmission electron microscopy. *Science* **321**, 506-510 (2008).
[89] Carter, D. B. W. a. C. B. *Transmission electron microscopy: a textbook for materials science*. (Plenum Press, 1996).
[90] Fultz, B. & Howe, J. *Transmission Electron Microscopy and Diffractometry of Materials*. 3rd edn, (Springer, 2008).
[91] Tanaka, M. & Honjo, G. Electron optical studies of barium titanate single crystal films. *J. Phys. Soc. Jpn.* **19**, 954-& (1964).
[92] Rafferty, B., Pennycook, S. J. & Brown, L. M. Zero loss peak deconvolution for bandgap EEL spectra. *J. Electron Microsc.* **49**, 517-524 (2000).
[93] Kimoto, K., Kothleitner, G., Grogger, W., Matsui, Y. & Hofer, F. Advantages of a monochromator for bandgap measurements using electron energy-loss spectroscopy. *Micron* **36**, 185-189 (2005).
[94] Nakagawa, N., Hwang, H. Y. & Muller, D. A. Why some interfaces cannot be sharp. *Nat. Mater.* **5**, 204-209 (2006).
[95] Muller, D. A. *et al.* Atomic-scale chemical imaging of composition and bonding by aberration-corrected microscopy. *Science* **319**, 1073-1076 (2008).
[96] Nakamura, Y., Mera, Y. & Maeda, K. A reproducible method to fabricate atomically sharp tips for scanning tunneling microscopy. *Rev. Sci. Instrum.* **70**, 3373-3376 (1999).
[97] Streiffer, S. K. *et al.* Domain patterns in epitaxial rhombohedral ferroelectric films. I. Geometry and experiments. *J. Appl. Phys.* **83**, 2742-2753 (1998).

[98] Gruverman, A., Wu, D. & Scott, J. F. Piezoresponse force microscopy studies of switching behavior of ferroelectric capacitors on a 100-ns time scale. *Phys. Rev. Lett.* **100**, 097601 (2008).

[99] Jesse, S. *et al.* Direct imaging of the spatial and energy distribution of nucleation centres in ferroelectric materials. *Nat. Mater.* **7**, 209-215 (2008).

[100] Ishikawa, R. *et al.* Direct imaging of hydrogen-atom columns in a crystal by annular bright-field electron microscopy. *Nat. Mater.* **10**, 278-281 (2011).

[101] Jia, C. L., Lentzen, M. & Urban, K. Atomic-resolution imaging of oxygen in perovskite ceramics. *Science* **299**, 870-873 (2003).

[102] Kisielowski, C. *et al.* Imaging columns of the light elements carbon, nitrogen and oxygen with sub Angstrom resolution. *Ultramicroscopy* **89**, 243-263 (2001).

[103] Borisevich, A. Y. *et al.* Suppression of Octahedral Tilts and Associated Changes in Electronic Properties at Epitaxial Oxide Heterostructure Interfaces. *Phys. Rev. Lett.* **105**, 4.

[104] Wu, C. L. *et al.* Direct spectroscopic evidence of charge reversal at the Pb(Zr(0.2)Ti(0.8))O(3)/La(0.7)Sr(0.3)MnO(3) heterointerface. *Phys. Rev. B* **83**, 020103 (2011).

[105] Ihlefeld, J. F. *et al.* in *2008 17th Ieee International Symposium on the Applications of Ferroelectrics IEEE International Symposium on Applications of Ferroelectrics* 301-302 (Ieee, 2008).

[106] Folkman, C. M. *et al.* Stripe domain structure in epitaxial (001) BiFeO(3) thin films on orthorhombic TbScO(3) substrate. *Appl. Phys. Lett.* **94**, 251911 (2009).

[107] Eom, C. B. *et al.* Single-crystal epitaxial thin-films of the isotropic metallic oxides Sr1-xCaxRuO3 (0-less-than-or-equal-to-x-less-than-or-equal-to-1). *Science* **258**, 1766-1769 (1992).

[108] Eom, C. B. *et al.* Fabrication and properties of epitaxial ferroelectric heterostructures with (SrRuO3) isotropic metallic oxide electrodes. *Appl. Phys. Lett.* **63**, 2570-2572 (1993).

[109] Eom, C. B. *et al.* Insitu grown YBa2Cu3O7-d thin-films from single-target magnetron sputtering. *Appl. Phys. Lett.* **55**, 595-597 (1989).

[110] Chen, L. Q. Phase-field method of phase transitions/domain structures in ferroelectric thin films: A review. *J. Am. Ceram. Soc.* **91**, 1835-1844 (2008).

[111] Tagantsev, A. K. & Gerra, G. Interface-induced phenomena in polarization response of ferroelectric thin films. *J. Appl. Phys.* **100**, 28 (2006).

[112] Tagantsev, A. K. Landau expansion for ferroelectrics: which variable to use? *Ferroelectrics* **375**, 19-27 (2008).

[113] Zhang, J. X. *et al.* Effect of substrate-induced strains on the spontaneous polarization of epitaxial BiFeO3 thin films. *J. Appl. Phys.* **101**, 114105 (2007).

[114] Li, Y. L., Hu, S. Y., Liu, Z. K. & Chen, L. Q. Effect of substrate constraint on the stability and evolution of ferroelectric domain structures in thin films. *Acta. Mater.* **50**, 395-411 (2002).

[115] Yang, S. Y. *et al.* Above-bandgap voltages from ferroelectric photovoltaic devices. *Nat. Nanotechnol.* **5**, 143-147 (2010).

[116] Jang, H. W. *et al.* Strain-induced polarization rotation in epitaxial (001) BiFeO(3) thin films. *Phys. Rev. Lett.* **101**, 107602 (2008).

[117] Chu, Y. H. *et al.* Domain control in mulfiferroic BiFeO3 through substrate vicinality. *Adv. Mater.* **19**, 2662-2666 (2007).
[118] Sun, H. P., Tian, W., Pan, X. Q., Haeni, J. H. & Schlom, D. G. Evolution of dislocation arrays in epitaxial BaTiO3 thin films grown on (100) SrTiO3. *Appl. Phys. Lett.* **84**, 3298-3300 (2004).
[119] Matthews, J. W. & Blakeslee, A. E. Defects in epitaxial multilayers. 1. Misfit dislocations. *J. Cryst. Growth* **27**, 118-125 (1974).
[120] Chu, M. W. *et al.* Impact of misfit dislocations on the polarization instability of epitaxial nanostructured ferroelectric perovskites. *Nat. Mater.* **3**, 87-90 (2004).
[121] Lee, D. *et al.* Giant Flexoelectric Effect in Ferroelectric Epitaxial Thin Films. *Phys. Rev. Lett.* **107**, 057602 (2011).
[122] Borisevich, A. Y. *et al.* Suppression of Octahedral Tilts and Associated Changes in Electronic Properties at Epitaxial Oxide Heterostructure Interfaces. *Phys. Rev. Lett.* **105**, 087204 (2010).
[123] Velickov, B., Kahlenberg, V., Bertram, R. & Uecker, R. Redetermination of terbium scandate, revealing a defect-type perovskite derivative. *Acta Crystallogr. Sect. E.-Struct Rep. Online* **64**, I79-U64 (2008).
[124] Sun, H. P., Pan, X. Q., Haeni, J. H. & Schlom, D. G. Structural evolution of dislocation half-loops in epitaxial BaTiO3 thin films during high-temperature annealing. *Appl. Phys. Lett.* **85**, 1967-1969 (2004).
[125] Jia, C. L. *et al.* Unit-cell scale mapping of ferroelectricity and tetragonality in epitaxial ultrathin ferroelectric films. *Nat. Mater.* **6**, 64-69 (2007).
[126] Jia, C. L. *et al.* Effect of a single dislocation in a heterostructure layer on the local polarization of a ferroelectric layer. *Phys. Rev. Lett.* **102**, 117601 (2009).
[127] Jia, C. L., Urban, K. W., Alexe, M., Hesse, D. & Vrejoiu, I. Direct Observation of Continuous Electric Dipole Rotation in Flux-Closure Domains in Ferroelectric Pb(Zr,Ti)O(3). *Science* **331**, 1420-1423 (2011).
[128] Jia, C. L. *et al.* Atomic-scale study of electric dipoles near charged and uncharged domain walls in ferroelectric films. *Nat. Mater.* **7**, 57-61 (2008).
[129] Li, J. F. *et al.* Dramatically enhanced polarization in (001), (101), and (111) BiFeO3 thin films due to epitiaxial-induced transitions. *Appl. Phys. Lett.* **84**, 5261-5263 (2004).
[130] Hytch, M. J., Snoeck, E. & Kilaas, R. Quantitative measurement of displacement and strain fields from HREM micrographs. *Ultramicroscopy* **74**, 131-146 (1998).
[131] Hytch, M. J., Putaux, J. L. & Penisson, J. M. Measurement of the displacement field of dislocations to 0.03 angstrom by electron microscopy. *Nature* **423**, 270-273 (2003).
[132] Chu, Y. H. *et al.* Nanoscale Control of Domain Architectures in BiFeO(3) Thin Films. *Nano Lett.* **9**, 1726-1730 (2009).
[133] Liferovich, R. P. & Mitchell, R. H. A structural study of ternary lanthanide orthoscandate perovskites. *J. Solid State Chem.* **177**, 2188-2197 (2004).
[134] Kalinin, S. V. & Bonnell, D. A. Local potential and polarization screening on ferroelectric surfaces. *Phys. Rev. B* **63**, 125411 (2001).
[135] Fong, D. D. *et al.* Stabilization of monodomain polarization in ultrathin PbTiO3 films. *Phys. Rev. Lett.* **96**, 127601 (2006).

[136] Spanier, J. E. *et al.* Ferroelectric phase transition in individual single-crystalline BaTiO3 nanowires. *Nano Lett.* **6**, 735-739 (2006).
[137] Lichtensteiger, C., Dawber, M. & Triscone, J. M. Ferroelectric size effects. **105**, 305-337 (2007).
[138] Ghosez, P. & Rabe, K. M. Microscopic model of ferroelectricity in stress-free PbTiO3 ultrathin films. *Appl. Phys. Lett.* **76**, 2767-2769 (2000).
[139] Kittel, C. Physical theory of ferromagnetic domains. *Rev. Mod. Phys.* **21**, 541-583 (1949).
[140] Rodriguez, B. J. *et al.* Vortex polarization states in nanoscale ferroelectric arrays. *Nano Lett.* **9**, 1127-1131 (2009).
[141] Schilling, A. *et al.* Domains in ferroelectric nanodots. *Nano Lett.* **9**, 3359-3364 (2009).
[142] Naumov, II, Bellaiche, L. & Fu, H. X. Unusual phase transitions in ferroelectric nanodisks and nanorods. *Nature* **432**, 737-740 (2004).
[143] Ivry, Y., Chu, D. P., Scott, J. F. & Durkan, C. Flux closure vortexlike domains structures in ferroelectric thin films. *Phys. Rev. Lett.* **104**, 207602 (2010).
[144] Balke, N. *et al.* Deterministic control of ferroelastic switching in multiferroic materials. *Nat. Nanotechnol.* **4**, 868-875 (2009).
[145] Nelson, C. T. *et al.* Spontaneous vortex nanodomain arrays at ferroelectric heterointerfaces. *Nano Lett.* **11**, 828-834 (2011).
[146] Huang, C. W. *et al.* Phenomenological analysis of domain width in rhombohedral BiFeO3 films. *Phys. Rev. B* **80**, 140101 (2009).
[147] Chisholm, M. F., Luo, W. D., Oxley, M. P., Pantelides, S. T. & Lee, H. N. Atomic-Scale Compensation Phenomena at Polar Interfaces. *Phys. Rev. Lett.* **105**, 197601 (2010).
[148] Chang, H. J. *et al.* Atomically Resolved Mapping of Polarization and Electric Fields Across Ferroelectric/Oxide Interfaces by Z-contrast Imaging. *Adv. Mater.* **23**, 2474-2479 (2011).
[149] Gopalan, V. & Mitchell, T. E. In situ video observation of 180 degrees domain switching in LiTaO3 by electro-optic imaging microscopy. *J. Appl. Phys.* **85**, 2304-2311 (1999).
[150] Gopalan, V. & Mitchell, T. E. Wall velocities, switching times, and the stabilization mechanism of 180 degrees domains in congruent LiTaO3 crystals. *J. Appl. Phys.* **83**, 941-954 (1998).
[151] Kuroda, A., Kurimura, S. & Uesu, Y. Domain inversion in ferroelectric MgO:LiNbO3 by applying electric fields. *Appl. Phys. Lett.* **69**, 1565-1567 (1996).
[152] Kim, D. J. *et al.* Observation of inhomogeneous domain nucleation in epitaxial Pb(Zr,Ti)O-3 capacitors. *Appl. Phys. Lett.* **91**, 132903 (2007).
[153] Yang, S. M., Yoon, J. G. & Noh, T. W. Nanoscale studies of defect-mediated polarization switching dynamics in ferroelectric thin film capacitors. *Curr. Appl. Phys.* **11**, 1111-1125 (2011).
[154] Tybell, T., Paruch, P., Giamarchi, T. & Triscone, J. M. Domain wall creep in epitaxial ferroelectric Pb(Zr0.2Ti0.8)O-3 thin films. *Phys. Rev. Lett.* **89**, 097601 (2002).
[155] Pan, X. Q. & Feng, D. Direct observation of nucleation of discommensurations in barium sodium niobate. *Phys. Status Solidi A-Appl. Res.* **106**, K117-K121 (1988).

[156] Pan, X. Q., Gleiter, H. & Feng, D. Dynamic evolution of discommensurations during the commensurate incommensurate transition in barium sodium niobate. *J. Phys.-Condes. Matter* **2**, 2603-2623 (1990).

[157] Pan, X. Q. & Unruh, H. G. Electron-microscopy study of discommensurations in K2ZnCl4. *J. Phys.-Condes. Matter* **2**, 323-329 (1990).

[158] Popoola, O. O. & Kriven, W. M. In-situ transmission electron microscopy study of phase transformations in KNbO3 perovskite. *Philos. Mag. Lett.* **75**, 1-5 (1997).

[159] Tai, C. W., Choy, S. H. & Chan, H. L. W. Ferroelectric Domain Morphology Evolution and Octahedral Tilting in Lead-Free (Bi1/2Na1/2)TiO3-(Bi1/2K1/2)TiO3-(Bi1/2Li1/2)TiO3-BaTiO3 Ceramics at Different Temperatures. *J. Am. Ceram. Soc.* **91**, 3335-3341 (2008).

[160] Kiguchi, T., Wakiya, N., Shinozaki, K. & Mizutani, N. in *Asian Ceramic Science for Electronics Ii and Electroceramics in Japan V, Proceedings* Vol. 228-2 *Key Engineering Materials* eds T. Kimura *et al.*) 203-206 (Trans Tech Publications Ltd, 2002).

[161] Snoeck, E., Normand, L., Thorel, A. & Roucau, C. Electron-microscopy study of ferroelastic and ferroelectric domain-wall motions induced by the in-situ application of an electric-field in BaTiO3. *Phase Transit.* **46**, 77-88 (1994).

[162] Krishnan, A., Bisher, M. E. & Treacy, M. M. J. in *Ferroelectric Thin Films Vii* Vol. 541 *Materials Research Society Symposium Proceedings* eds R. E. Jones, R. W. Schwartz, S. R. Summerfelt, & I. K. Yoo) 475-480 (Materials Research Society, 1999).

[163] Qi, X. Y., Liu, H. H. & Duan, X. F. In situ transmission electron microscopy study of electric-field-induced 90 degrees domain switching in BaTiO3 single crystals. *Appl. Phys. Lett.* **89**, 092908 (2006).

[164] Zhang, Z. H., Qi, X. Y. & Duan, X. F. Two-step evolution mechanism of multi-domains in BaTiO(3) single crystal investigated by in situ transmission electron microscopy. *Scr. Mater.* **58**, 441-444 (2008).

[165] Lin, X., Murray, C. & V. P. Dravid. Statics and dynamics of charged interfaces in electroceramics. 552-553 (1998).

[166] Tan, X. L., Xu, Z. K. & Shang, J. K. In situ transmission electron microscopy observations of electric-field-induced domain switching and microcracking in ferroelectric ceramics. *Mater. Sci. Eng. A-Struct. Mater. Prop. Microstruct. Process.* **314**, 157-161 (2001).

[167] Qu, W., Zhao, X. & Tan, X. In situ transmission electron microscopy study of the nanodomain growth in a Sc-doped lead magnesium niobate ceramic. *Appl. Phys. Lett.* **89**, 022904 (2006).

[168] Tan, X. L., He, H. & Shang, J. K. In situ transmission electron microscopy studies of electric-field-induced phenomena in ferroelectrics. *J. Mater. Res.* **20**, 1641-1653 (2005).

[169] Tan, X., Xu, Z., Shang, J. K. & Han, P. Direct observations of electric field-induced domain boundary cracking in < 001 > oriented piezoelectric Pb(Mg1/3Nb2/3)O-3-PbTiO3 single crystal. *Appl. Phys. Lett.* **77**, 1529-1531 (2000).

[170] Tan, X. L. & Shang, J. K. In-situ transmission electron microscopy study of electric-field-induced grain-boundary cracking in lead zirconate titanate. *Philos. Mag. A-Phys. Condens. Matter Struct. Defect Mech. Prop.* **82**, 1463-1478 (2002).
[171] Zhang, J. X. *et al.* Large field-induced strains in a lead-free piezoelectric material. *Nat. Nanotechnol.* **6**, 97-101 (2011).
[172] Chang, H. J. *et al.* Watching domains grow: In-situ studies of polarization switching by combined scanning probe and scanning transmission electron microscopy. *J. Appl. Phys.* **110**, 052014 (2011).
[173] Pabst, G. W., Martin, L. W., Chu, Y. H. & Ramesh, R. Leakage mechanisms in BiFeO3 thin films. *Appl. Phys. Lett.* **90**, 072902 (2007).
[174] Rose, A. space-charge limited currents in solids. **97**, 1538-1544 (1955).
[175] Lampert, M. A., Many, A. & Mark, P. space-charge-limited currents injected from a point contact. **135**, 1444-1453 (1964).
[176] Forbes, R. G. & Deane, J. H. B. Reformulation of the standard theory of Fowler-Nordheim tunnelling and cold field electron emission. *Proc. R. Soc. A-Math. Phys. Eng. Sci.* **463**, 2907-2927 (2007).
[177] Blom, P. W. M., Wolf, R. M., Cillessen, J. F. M. & Krijn, M. feroelectric schottky diode. *Phys. Rev. Lett.* **73**, 2107-2110 (1994).
[178] Pantel, D. & Alexe, M. Electroresistance effects in ferroelectric tunnel barriers. *Phys. Rev. B* **82**, 134105 (2010).
[179] Egerton, R. F., Li, P. & Malac, M. Radiation damage in the TEM and SEM. *Micron* **35**, 399-409 (2004).
[180] Scofield, J. H. K-shell and L-shell ionization of atoms by relatavistic electrons. *Phys. Rev. A* **18**, 963-970 (1978).
[181] Zhang, J. *et al.* Surface, bulk, and interface electronic states of epitaxial BiFeO3 films. *J. Vac. Sci. Technol. B* **27**, 2012-2014 (2009).
[182] Ihlefeld, J. F. *et al.* Optical band gap of BiFeO(3) grown by molecular-beam epitaxy. *Appl. Phys. Lett.* **92**, 142908 (2008).
[183] Yang, H., Wang, Y. Q., Wang, H. & Jia, Q. X. Oxygen concentration and its effect on the leakage current in BiFeO(3) thin films. *Appl. Phys. Lett.* **96**, 012909 (2010).
[184] Johnson, K. L. *Contact Mechanics*. (Cambridge University Press, 1985).
[185] Ma, W. H. & Cross, L. E. Strain-gradient-induced electric polarization in lead zirconate titanate ceramics. *Appl. Phys. Lett.* **82**, 3293-3295 (2003).
[186] Balke, N. *et al.* Direct observation of capacitor switching using planar electrodes. *Adv. Funct. Mater.* **20**, 3466-3475 (2010).
[187] Clark, S. J. & Robertson, J. Band gap and Schottky barrier heights of multiferroic BiFeO3. *Appl. Phys. Lett.* **90**, 132903 (2007).
[188] Folkman, C. M. *et al.* Study of defect-dipoles in an epitaxial ferroelectric thin film. *Appl. Phys. Lett.* **96**, 052903 (2010).
[189] de Jong, M. P., Dediu, V. A., Taliani, C. & Salaneck, W. R. Electronic structure of La0.7Sr0.3MnO3 thin films for hybrid organic/inorganic spintronics applications. *J. Appl. Phys.* **94**, 7292-7296 (2003).
[190] Muller, E. W. Work function of tungsten single crystal planes measured by the field emission microscope. *J. Appl. Phys.* **26**, 732-737 (1955).

[191] Yuan, G. L. & Uedono, A. Behavior of oxygen vacancies in BiFeO3/SrRuO3/SrTiO3(100) and DyScO3(100) heterostructures. *Appl. Phys. Lett.* **94**, 132905 (2009).
[192] Scott, J. F. & Dawber, M. Oxygen-vacancy ordering as a fatigue mechanism in perovskite ferroelectrics. *Appl. Phys. Lett.* **76**, 3801-3803 (2000).
[193] Yoshida, C., Yoshida, A. & Tamura, H. Nanoscale conduction modulation in Au/Pb(Zr, Ti)O-3/SrRuO3 heterostructure. *Appl. Phys. Lett.* **75**, 1449-1451 (1999).
[194] Sze, S. M., Coleman, D. J. & Loya, A. Current transport in metal-semiconductor-metal (MSM) structures. *Solid-State Electron.* **14**, 1209-1218 (1971).
[195] Pintilie, L. *et al.* Orientation-dependent potential barriers in case of epitaxial Pt-BiFeO3-SrRuO3 capacitors. *Appl. Phys. Lett.* **94**, 232902 (2009).
[196] Scott, J. F. Device physics of ferroelectric thin-film memories. *Jpn. J. Appl. Phys. Part 1 - Regul. Pap. Short Notes Rev. Pap.* **38**, 2272-2274 (1999).
[197] Hartmann, A. J., Neilson, M., Lamb, R. N., Watanabe, K. & Scott, J. F. Ruthenium oxide and strontium ruthenate electrodes for ferroelectric thin-films capacitors. *Appl. Phys. A-Mater. Sci. Process.* **70**, 239-242 (2000).
[198] Neamen, D. A. *Semiconductor Physics and Devices*. (Irwin/McGraw-Hill, 1997).
[199] Maksymovych, P. *et al.* Defect-induced asymmetry of local hysteresis loops on BiFeO3 surfaces. *J. Mater. Sci.* **44**, 5095-5101 (2009).